SANDIA REPORT

SAND2017-10287
Unlimited Release
Printed September, 2017

Developing a novel hierarchical approach for multiscale structural reliability predictions for ultra-high consequence applications

John M. Emery, Peter Coffin, Brian A. Robbins, Jay Carroll,
Rich V. Field, Yung Suk Jeremy Yoo, Josh Kacher

Prepared by
Sandia National Laboratories
Albuquerque, New Mexico 87185 and Livermore, California 94550

Sandia National Laboratories is a multimission laboratory managed and operated by National Technology and Engineering Solutions of Sandia, LLC., a wholly owned subsidiary of Honeywell International, Inc., for the U.S. Department of Energy's National Nuclear Security Administration under contract DE-NA0003525.

Sandia National Laboratories

Issued by Sandia National Laboratories, operated for the United States Department of Energy by National Technology and Engineering Solutions of Sandia, LLC.

Available to DOE and DOE contractors from
U.S. Department of Energy
Office of Scientific and Technical Information
P.O. Box 62
Oak Ridge, TN 37831

Telephone:	(865) 576-8401
Facsimile:	(865) 576-5728
E-Mail:	reports@adonis.osti.gov
Online ordering:	http://www.osti.gov/bridge

Available to the public from
U.S. Department of Commerce
National Technical Information Service
5285 Port Royal Rd
Springfield, VA 22161

Telephone:	(800) 553-6847
Facsimile:	(703) 605-6900
E-Mail:	orders@ntis.fedworld.gov
Online ordering:	http://www.ntis.gov/help/ordermethods.asp?loc=7-4-0#online

SAND2017-10287
Unlimited Release
Printed September, 2017

Developing a novel hierarchical approach for multiscale structural reliability predictions for ultra-high consequence applications

John M. Emery, Peter Coffin, Brian A. Robbins, Jay Carroll,
Rich V. Field, Yung Suk Jeremy Yoo, Josh Kacher

Abstract

Microstructural variabilities are among the predominant sources of uncertainty in structural performance and reliability. We seek to develop efficient algorithms for multiscale calculations for polycrystalline alloys such as aluminum alloy 6061-T6 in environments where ductile fracture is the dominant failure mode. Our approach employs concurrent multiscale methods, but does not focus on their development. They are a necessary but not sufficient ingredient to multiscale reliability predictions. We have focused on how to efficiently use concurrent models for forward propagation because practical applications cannot include fine-scale details throughout the problem domain due to exorbitant computational demand.

Our approach begins with a low-fidelity prediction at the engineering scale that is subsequently refined with multiscale simulation. The results presented in this report focus on plasticity and damage at the meso-scale, efforts to expedite Monte Carlo simulation with microstructural considerations, modeling aspects regarding geometric representation of grains and second-phase particles, and contrasting algorithms for scale coupling.

Acknowledgment

The team gratefully acknowledges fruitful discussions with James W. Foulk III, Kyle Karlson, Alejandro Mota, Jake Ostien, Mike Veilleux, Kyle Johnson, Judy Brown, Hojun Lim, Jake Hochhalter (NASA-LaRC) and Ben Reedlun – who also shared Python code for plotting inverse pole figures.

A special note of gratitude is extended to Joseph Bishop who was originally part of the team during the proposal stage. When we had some budget contraction, Joe graciously stepped back, but remained engaged as a mentor, interested collaborator, sounding board, and finally reviewer of this report. Thanks Joe!

Contents

Summary **14**

1 Introduction **17**

1.1 Hierarchical multiscale simulation 19

2 Material form and behavior of the AA 6061-T6 **23**

2.1 Metallurgical details of AA 6061-T6 23

2.2 Specimens 28

3 Microstructure modeling **33**

3.1 Translation model for generating polycrystalline texture models 33

3.1.1 Analysis of the available EBSD data 34

3.1.2 Analysis of Euler angle experimental observations for the purpose of informing the translation random vector model 34

3.1.3 Vector-valued translation random field model definition 36

3.1.4 Model calibration and implementation of translation model 38

3.1.5 Reduced-order model for vector-valued random field 39

3.2 Microstructure mesh model development 43

3.2.1 Grain independent meshing 44

3.2.2 Grain boundary conforming meshing 45

3.2.3 Consistent discretization of the second phase particle 46

3.2.4 Comparing particle breaking load for GB-conforming and non-conforming microstructures 48

3.3 Chapter summary 51

4 Multiscale simulation 52
4.1 Submodeling 53
4.2 MPC coupling 53
4.3 Comparing the approaches 55
4.4 Chapter summary 57

5 Multiscale digital image correlation 59

6 Numerical examples 67
6.1 Example 1 – cubic elasticity and micron-size plate in plane strain 67
6.1.1 Formulation 67
6.1.2 Results 69
6.1.3 Comments 71
6.2 Example 2 – microstructure texture models 72
6.2.1 Formulation 72
6.2.2 Results 74
6.3 Example 3 – microstructure and second-phase particle 74
6.3.1 Formulation 74
6.3.2 Results 77
6.4 Example 4 – multiscale now! 78
6.4.1 Formulation 78
6.4.2 Results 81

7 Quantifying dislocation accumulation via a combined EBSD - in situ SEM deformation approach 85
7.1 Experimental 85
7.2 Results and analysis 86
7.2.1 Dislocation distribution as a function of depth from the surface 86

7.2.2 Dislocation distribution as a function of strain 88

7.2.3 Quantification of microstructure/dislocation accumulation relationship 88

7.3 Summary 92

8 Conclusions **94**

References **96**

Appendix

A Multiscale uncertainty modeling code and Git repository **100**

B Engineering drawings **101**

List of Figures

1.2 Hierarchical multiscale simulation approach. 20

1.3 Arbitrary solid subjected to applied load. 21

1.4 Spatial partition of solid into n regions. 22

2.1 Micrographs showing inclusions and precipitates in AA 6061-T6. Originally, it was thought that these might provide a basis for a DIC speckle pattern, but they are too sparse and they lose contrast upon loading. 24

2.2 X-ray diffraction peaks showing some of the detected elements in this alloy. . 25

2.3 Spatial distribution of chemical constitituents measured by X-ray diffraction for AA 6061-T6 rolled plate. 26

2.4 Orientation convention for crystallographic plots. 26

2.5 EBSD maps from three primary directions of the plate colored according to the legend in Figure 2.4 with respect to the direction of view (normal, rolling, and transverse respectively). 27

2.6 Pole figures showing the texture of the AA 6061-T6. There is some preference for [100] texture in the rolling direction and a slight [110] bias in the other two directions. This is similar to a Goss texture. 28

2.7 Inverse pole figures of the AA 6061-T6 microstructure showing a 100 texture in the rolling direction with a slight secondary 111 rolling texture and preferential 100 and 110 orientations in the normal direction. 28

2.8 Normalized histograms of the Euler angles from the plan EBSD measurement. 29

2.9 Normalized histograms of the lattice misorientations from the plan, longitudinal, and transverse EBSD measurements. 30

2.10 In situ image of a broken sharp-notch specimen. 31

2.11 Engineering stress-strain curves for a the smooth, gradual-notched (GN), and sharp-notched (SN) tensile specimens in both rolling (R) and transverse (T) directions used for characterization. 31

2.12 Series of medium magnification images at the root of the six notches. Fracture sets up in the middle set of notches. 32

2.13 Normalized load versus strain curves for a the 6-notched tensile specimen serving as our "idealized component" for model validation. 32

3.1 Histogram and measurement locations of $\{\psi_j(\mathbf{x}_k), j = 1, 2, 3, k = 1, \ldots, n_j\}$ for the longitudinal direction of the aluminum alloy. The presented histograms illustrate the difference in the PDFs of the euler angles (a) $\{\psi_1(\mathbf{x}_k,\ k = 1, \ldots, n_1\}$, (c) $\{\psi_2(\mathbf{x}_k,\ k = 1, \ldots, n_2\}$, and (e) $\{\psi_3(\mathbf{x}_k,\ k = 1, \ldots, n_3\}$. The measurement locations are also illustrated for (b) $\{\mathbf{x}_k, k = 1, \ldots, n_1\}$, (d) $\{\mathbf{x}_k, k = 1, \ldots, n_2\}$, and (f) $\{\mathbf{x}_k, k = 1, \ldots, n_3\}$. The voronoi tessellation is included for visualization; additionally, the color map indicates the value of the corresponding $\{\psi_j(\mathbf{x}_k),\ j = 1, 2, 3,\ k = 1, \ldots, n_j\}$. 35

3.2 Inverse pole figures from ensembles of non-, macro-, and micro-textured (top to bottom) 224-grain polycrystal samples. 40

3.3 Histograms of the Euler angles from an ensemble of non-textured 224-grain polycrystal samples. 41

3.4 Histograms of the Euler angles from an ensemble of macro-textured 224-grain polycrystal samples. 42

3.5 Histograms of the Euler angles from an ensemble of micro-textured 224-grain polycrystal samples. 43

3.6 Histograms of the misorientation angles from ensembles of non-, macro-, and micro-textured (top to bottom) 224-grain polycrystal samples. 44

3.7 View of mesh using the overlay technique where elements do not conform to the grain boundaries 45

3.8 View of mesh where elements do conform to the grain boundaries 46

3.9 Comparison of tetrahedral meshed ellipsoid (left) and hexahedral meshed particle that comes out from Sculpt (right). 47

3.10 Comparison of principle stress at the inclusion-matrix boundary between tetrahedral mesh using scheme hybrid meshing scheme (left) and GB-conforming scheme (right). 49

3.11 Zoomed view of differences in principle stress between the hybrid and GB-conforming approaches. 49

3.12 View of pressure at surface of inclusion for model constructed using the scheme of Section 3.2.3. 50

3.13 Comparison of statistics resulting from different meshing schemes 50

3.14 Comparison of meshing approaches at the start of plastic deformation 51

4.1 Depiction of submodeling process: engineering scale solution, mapping displacements to mesoscale model, solving mesoscale model 53

4.2 Depiction of submodeling process: engineering scale solution, mapping displacements to mesoscale model, solving mesoscale model 54

4.3 Engineering scale model is decomposed to contain region $(\mathcal{D} \setminus \mathcal{D}_k = S$ (left) so that the microstructural model (right) has a tight fit. 54

4.4 Comparison of the multiscale modeling approaches showing the deformation of the polycrystal (a) and particle (b). 56

4.5 Maximum first-principle stress in the particle for MPC macro texture (red), MPC microtexture (blue), submodel macro texture (green) and submodel micro texture (pink). 56

4.6 Comparison of statistics resulting from different coupling schemes run for many realizations of microtexture. The data plotted are mean and +/- standard deviation for the MPC (red) and submodeling approachs (blue). 57

5.1 Multiscale DIC uses low magnification images to cover the entire specimen, and high magnification images to capture deformation details at stress concentrators. 59

5.2 Grain orientations in a 6-notch specimen relative to the (a) transverse direction (b) rolling direction, and (c) normal direction. 60

5.3 Failure in this specimen geometry is most likely at the center notches due to two diagonal shear bands whereas the distal notches only have one. 60

5.4 Low magnification montages were used to image the entire specimen. High resolution montages were used to image notch tips with sub-grain level details. 61

5.5 Speckle patterns created by several different settings (see Table 5.1) with coating thicknesses of 50 nm (top) and 80 nm (bottom). Images are consistently 64 μm wide, captured using backscatter electron imaging. 62

5.6 Challenges with montaging DIC data with SEM distortions. 63

5.7 SEM-DIC distortion correction technique taken from [1]. In this case, four steps are taken in the X and Y directions covering a total distance of one quarter of the field of view in each direction. 64

5.8 DIC strain measurement at notch tips just before specimen fracture achieved with copper powder speckling. The eventual fracture path is shown by the dashed line. 65

5.9 Grain level DIC strain accumulation at a notch tip. 65

5.10 MultiSEM imaging of large areas. 66

6.1 Boundary conditions for example 1. 68

6.2 A sample σ_{xx} distribution for a micro-textured example 1. 68

6.3 Estimated "truth" cumulative distribution for apparent modulus of a plane strain, micro-size plate with non-, macro-, and micro-textured cubic crystals. 70

6.4 Cumulative probability estimates of apparent modulus for a non-textured microstructure. 71

6.5 Cumulative probability estimates of apparent modulus for a macro-textured microstructure. 72

6.6 Cumulative probability estimates of apparent modulus for a micro-textured microstructure. 73

6.7 Two texture samples of an aluminum 6061-T6 rolled microstructure. The macro texture sample (left) does not include spatial correlation in the random-field model for crystallographic orientation whereas the micro texture sample (right) does. 73

6.8 Crystal plasticity calibration to average smooth tensile data. 74

6.9 Approximated yield surface for macro- and micro-textured polycrystals at 0.2% and 2.0% effective strain. 75

6.10 Particle/microstructure geometry for two instances of grain morphology. The images are taken at a cross-section intersecting the particle for display. 76

6.11 Particle stress-strain relations for a variety of surrounding textures. 78

6.12 Statistics of broken particles with mean stress metric when the particle is assumed to be an elasto-plastic material with power-law hardening. 79

6.13 Statistics of broken particles with maximum stress metric when the particle is assumed to be an elasto-plastic material with power-law hardening. 80

6.14 Calibration results for calibrating the Hill plasticity model with damage to the smooth, gradual-notch, and sharp-notch tenstion data. Calibrations were performed with MatCal. 81

6.15 Engineering scale simulation plotted on the experimental observations. 82

6.16 Effective stress contour contour plot (top) and triaxiality contour plot (bottom). 82

6.17 Magnified view of the triaxiality on a bisecting cross-section of the specimen at the middle notch identifying the hot spot from the engineering level simulation. 83

6.18 Statistics of broken particles when the particle is coupled to a Hill plasticity engineering scale model. 84

7.1 (a) Inverse pole figure (IPF) map of notched AA 6061-T6 sample strained to 2%. (b) GND density map generated from orientation data. (c-d) GND density map at 200 and 400 μm from surface, respectively. Insets in b-c show FEA predictions of elastic strain field. (e) column-wise average of GND density taken from b-d. Data are shown on a lograrithmic scale. 87

7.2 GND distribution in front of notch at (a) 0% strain, (b) 1.4% strain, and (2) 1.8% strain. GND density plotted on logarithmic scale from 10^3 to $10^{14.8}$ m^{-2}. Insets show dislocation accumulation around intermetallic constituent particles. 88

7.3 Inverse pole figure maps (a-c, g-i) and GND density maps (d-f, j-l) at 0%, 1%, and 2% strain at two regions of interest. GND density plotted on log scale from 10^{13} to $10^{15.6}$ m^{-2}. 89

7.4 Different microstructural representations of scan shown in Fig 7.1c. (a) IPF map, (b) grain size map, (c) GND density map, (d) proximity to second phase particles, 0 - 40 μm, (e) proximity to grain boundary, 0 - 20 μm, (f) proximity to triple junction, 0 - 20 μm. 91

7.5 Average GND density as a function of distance from microstructural feature of interest. 'None' indicates that no three of the listed features are with the given distance. (b) Data separated between large grains (D $>$ 40μm) and small grains (D $<$ 20μm). GND density plotted on logarithmic scale. 92

7.6 Secondary electron image (SEM) and HREBSD scan data around a cracked intermetallic particle found ahead of a crack tip. KAM map is overlaid on an EBSD pattern image quality map to give quasi-topographical information. White arrows in KAM map indicate the presence of dispersoids. KAM map scale is linear from 0 - 5°and for GND density map is logarithmic from $10^{13.85}$ to $10^{15.5}$ m^{-2}. 93

List of Tables

2.1 The chemical composition of AA 6061-T6 plate. 23

2.2 Mechanical properties of AA 6061-T6 from the manufacturer. 23

3.1 Sample mean and standard deviation of Euler angles. 36

3.2 Estimates of parameters for exponential fit to scaled covariance functions defined by Eq. 3.4 for each data set. 37

5.1 Settings used for each sputter. 62

6.1 Maximum likelihood estimates. 69

6.2 MLE parameters for beta for apparent modulus from 20 samples. 69

6.3 L_∞-norm comparing the CDFs of the models to the “truth” data. 71

6.4 L^2-norm comparing the CDFs of the models to the “truth” data. 72

6.5 Crystal plasticity material parameters. 74

6.6 Hill plasticity parameters calibrated to the available smooth, gradual-notched and sharp-notched tension data. 81

A.1 Code and data stored in Git repositories. 100

Summary

The primary goal of this research is to develop tools and capabilities for efficient multiscale uncertainty propagation (UP) using finite elements (FE) for tractable multiscale structural reliability calculations and uncertainty quantification (UQ). Recognizing many sources of uncertainty, this work focuses on materials-scale variability and its fundamental importance to failure governed by localization processes such as fracture. Homogenization techniques or hierarchical multiscale techniques are insufficient for a high-fidelity representation of the requisite physical processes and when the mission requires ultra-high reliability, *e.g.*, failure probability $< 1 \times 10^{-6}$. We do not develop a new multiscale numerical method (MNM), but we employ domain decomposition and multipoint constraints to achieve a continuum-to-continuum coupling of our engineering-scale domain with a polycrystalline, meso-scale domain. The tools and capabilities developed by this program are non-intrusive and strive to readily leverage ongoing developments in coupled multiscale calculations in the future.

We propose a hierarchical, multifidelity solution that systematically focuses computational resources at hotspots identified by engineering-scale simulations and combines the results from multiscale analyses to maximize efficiency. We have developed a Git repository of multiscale UP/UQ tools that strive to make Monte Carlo Simulation (MCS) tractable using stochastic reduced-order models (SROMs). The present work focuses on two length scales of a common engineering aluminum alloy 6061-T6: the engineering scale and the materials microstructural length scale. We employ the tools in our repository for reliability predictions of an aluminum engineering structure in which the primary ductile failure mechanism is void nucleation through fracture or pull-out of iron-bearing second-phase particles.

Our engineering-scale simulations used Hill anisotropic plasticity and damage. The multiscale simulations conducted for this project focused on the variability associated with random grain orientation, including spatial correlation to capture grain misorientation, and its influence on fracture load in second-phase particles. Apparently, including misorientation in microstructural models has an important effect on the probability distribution of particle loading. During research to prepare our microstructural finite element models for multiscale analysis, we explored the effect of a convenient simplification for the geometric representation of grain boundaries. We employed the newly developed Sandia tool Sculpt [2] to develop FE meshes of microstructures whose mesh boundaries conformed to the material's idealized grain boundaries. A simpler approach is to overlay grain orientation onto an existing background mesh resulting in grain boundaries that are not smooth and that have sharp corners introduced by the background mesh. For the problems that we considered for AA 6061-T6 and that explicitly include a second-phase in the microstructure, it appears less important to carefully treat the grain boundary. Further, an important contribution of this work was the development of random-field reduced order models (RFROMs) to expedite MCS of polycrystalline materials.

Our experimental efforts made developments towards a multiscale digital image correlation (DIC) technique for use in model validation, and through high-resolution electron backscatter diffraction (EBSD) measurements and serial section, identified key relationships between microstructural features and dislocation density leading to damage and crack nucleation. The multiscale DIC attempted to capture two distinctly different length scales of strain data in situ, so that engineering-scale and microstructural strain fields could be simultaneously observed. While ultimately unsuccessful in the lifespan of this project, many speckle patterns were ruled out and a thin-film remodeling method was identified as a strong candidate. Work on the topic will continue and the data will be useful for validating multiscale calculations. The high-resolution EBSD work was achieved through the Academic Alliance LDRD program and collaboration with Professor Josh Kacher at Georgia Institute of Technology (GT). The Kacher contract was extremely productive with the only regret being it was a one-year contract in the final year of this project. The GT data captured dislocation accumulations occurring in the presence of a strong gradient caused by a sharp notch at grain boundaries, grain boundary triple junctions, and second-phase particles. This information is measured at the surface of a specimen and at a multiple serial-sectioned depths below the surface approaching the midplane of the specimen. This data is very informative about ranking the importance of microstructural features for damage processes and can be use in the future for calibrating damage models at the microstructural length scale. The work also demonstrated dislocation accumulation near a broken second-phase particle near the tip of a sharp crack and suggested the accumulation caused the particle to fracture.

In summary, the following itemizes our findings and newly developed capabilities:

- a tool to model random fields, calibrated to data, that generates statistically equivalent samples for Monte Carlo simulation;
- a reduced-order model for random fields and it was shown to be accurate and efficient for propagating uncertainty;
- understanding of the impacts of modeling assumptions about grain boundaries in the presence of a material's second phase and concluded that overlay microstructures are sufficient in some cases, despite leading to artificially roughened grain boundaries;
- understanding of the effects of microtexture on particle breaking load in second-phase particles and found that microtexture broadens the probability density function for crack nucleating load in the particle;
- multiscale simulations coupling the engineering scale to the material microstructural scale concurrently and with one-way submodel coupling and noting various differences in the particle breaking load;
- concurrently coupling the engineering scale with a microstructure that contains a crack nucleating agent (second-phase), in 3D and with Monte Carlo simulation for estimates of probability;

- using a combined EBSD/in situ SEM deformation approach, it was shown that dislocation accumulation occurs preferentially near intermetallic particles, in particular those that are located in small grains.

This list falls short of our ambitious goals at the outset of the project, which hoped to have a coherent tool for multiscale UQ. Nevertheless, the state of understanding and capability for multiscale uncertainty quantification has significantly progressed over the coarse of the investigation.

This report provides details on the progress, archives the code capabilities, and identifies the future steps to continue the success of the work.

Chapter 1

Introduction

The primary goal of this research is to develop tools and capabilities for efficient multiscale uncertainty propagation (UP) using finite elements (FE) for tractable multiscale structural reliability calculations and uncertainty quantification (UQ). The outcomes will impact Sandia's safety and security mission, which requires ultra-high reliability, *e.g.*, failure probability $< 1 \times 10^{-6}$. There are many sources of aleotoric and epistemic uncertainty that impact the S&S mission, *e.g.*, environment, boundary conditions, materials processing, personnel handling, constitutive model error, and discretization errors. This work focuses on materials-scale variability and its fundamental importance to failure governed by localization processes such as fracture, a very complex and stochastic phenomena as illustrated by the image in Figure 1.1.

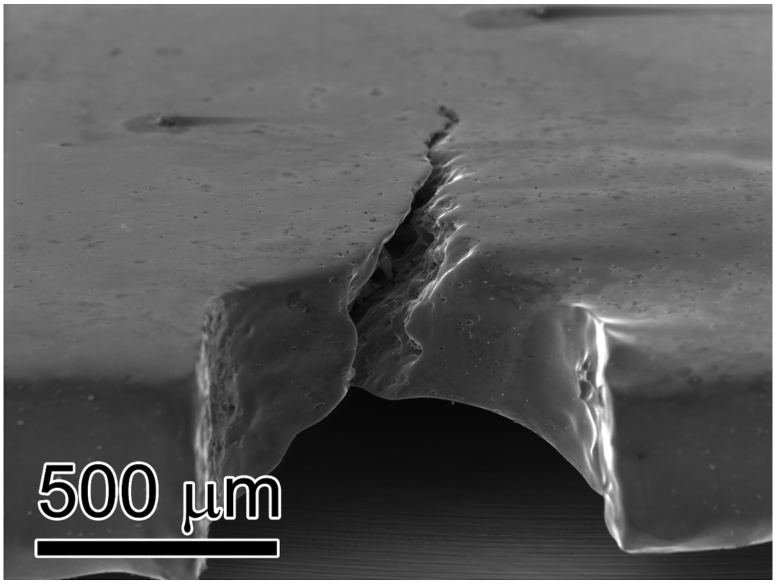

Figure 1.1: High resolution SEM image of crack propagation at the tip of a sharp notch demonstrating the complex and stochastic nature of fracture in polycrystalline materials (Kacher Lab.)

Philosophically, we believe that homogenization techniques or hierarchical multiscale techniques are insufficient for a high-fidelity representation of the requisite physical processes and mechanisms present during a localization event, especially when ultra-high reliability requirements exist. We do not develop a new multiscale numerical method (MNM). Rather, the focus of this work is on what we consider to be the larger aspect of multiscale UQ: how to effeciently make use of a MNM for reliability predictions. Practical applications cannot include fine-scale details throughout the problem domain due to exorbitant computational demand. A concurrent MNM is necessary but not sufficient.

Example: A multiscale FE analysis including a polycrystalline subdomain at one hotspot in a component can easily require the solution to tens of millions of equations or more for one realization of the microstructure a very computationally expensive endeavor. However, this solution represents only one data point for the conditional probability of failure assuming failure occurs at that hotspot. There are presumably many hotspots. To complete the reliability assessment, Monte Carlo simulation (MCS) is necessary at each hotspot, requiring many thousands of such analyses - this is intractable.

We introduce an novel hierarchical approach for multiscale reliability that employs stochastic reduced-order models (SROMs) as a surrogate to perform MCS at multilple length scales, and a multifidelity algorithm to leverage results from both low- and high-fidelity physics calculations [3, 4]. The core of this hierarhcy is discussed below in Section1.1, and the entire report supports the framework with important details. Brute force direct numerical calculation cannot generate sufficient Monte Carlo samples for prediction of ultra-high reliability, i.e., probability of failure less than 1×10^{-6}, when the analyses are as cumbersome as described in the above example. SROMs provide a reduced-order representation of the uncertain inputs that enable construction of a response surface for rapid Monte Carlo sampling [5]. For proof of concept, we focus on localization in an idealized "component" constructed from polycrystalline aluminum alloy 6061-T6 rolled sheet, which is commonly used in nuclear weapons (NW) and aerospace applications. However, the developments remain sufficiently general that future applications could be extended to address other multiscale problems of interest, *e.g.*, failure of bolted structures.

Our hierarchical multiscale approach requires a model at the engineering scale, which we do not focus on in this report. The engineering scale would follow the developments of [6] closely. We do present some engineering scale calculations with the numerical examples to motivate the multiscale example. There we use Hill plasticity [7] and damage [8] to model the physical behavior. In the hierarchical framework, SROMs [9, 5] following [6] would be used to propagate uncertainty in constitutive model parameters calibrated to available test data. For our microstructural models, we explore several options for geometry and mesh modeling, we include a material second-phase particle, and we use a common crystal plasticity formulation to relate deformation to stress [10]. These models are discussed at length in Chapter 3. To connect the length scales – reiterating that we were not focused on the development of a new MNM – we employ a rather unsophisitcated domain decomposition method with multipoint constraints (MPC) to achieve continuum-to-continuum coupling of our engineering-scale domain with a polycrystalline, meso-scale domain [11]. Further, we make some simple comparisons between the MPC approach and a traditional sub-modeling approach, which achieves only one-way coupling. These preliminary findings support our emphasis on concurrent coupling and are discussed in Chapter 4. The computational efforts are summarized through numerical examples in Chapter 6, which demonstrate the a number of elements of the hierarchical approach. The tools and capabilities developed by this program are non-intrusive and strive to readily leverage ongoing developments in coupled multiscale calculations in the future [12].

Our experimental efforts made developments towards a multiscale digital image correlation (DIC) technique for use in model validation, and through high-resolution electron backscatter diffraction (EBSD) measurements and serial section, identify key relationships between microstructural features and dislocation density leading to damage and crack nucleation. Chapter 5 outlines the multiscale DIC method, which attempted to capture two distinctly different length scales of strain data in situ, so that engineering-scale and microstructural strain fields could be simultaneously observed. While ultimately unsuccessful in the lifespan of this project, significant progress on development of the multiscale speckle pattern was made. Several speckle patterns with a variety of methods were ruled out and a thin-film remodeling method was identified as a strong candidate. Work on the topic will continue and the data will be useful for validating multiscale calculations. The high-resolution EBSD work, summarized in Chapter 7, was achieved through the Academic Alliance LDRD program and collaboration with Professor Josh Kacher at Georgia Institute of Technology (GT). The Kacher contract was extremely productive with the only regret being it was a one-year contract in the final year this project. The GT data captures dislocation accumulations occurring in the presence of a strong gradient caused by a sharp notch at grain boundaries, grain boundary triple junctions, and second-phase particles. This information is measured at the surface of a specimen and at a multiple serial-sectioned depths below the surface approaching the midplane of the specimen. This data is very informative about ranking the importance of microstructural features for damage processes and can be use in the future for calibrating damage models at the microstructural length scale.

1.1 Hierarchical multiscale simulation

We propose a hierarchical methodology for multiscale uncertainty quantification, shown with the notional flowchart in Figure 1.2. The present report is focused on crack nucleation in AA 6061-T6 but the methodology is readily adaptable to other multiscale problems. In fact, the lower-fidelity modeling approach is based on prior research to propagate uncertainty for estimates of probability of system failure due to laser welds in abnormal mechanical environments [6]. Crack nucleation in AA 6061-T6 and the laser weld problem differ only subtly in the material ductility, form and polycrystalline properties, but in general the hierarchical approach could be applied to vastly different types of multiscale problems. Each level in the hierarchy takes a set of random inputs (left) and results in a probabilistic prediction of system performance (right). The random inputs can include all known sources of aleatoric uncertainties, *e.g.* materials properties and boundary conditions. In addition, each successive level in the hierarchy has two additional inputs, the prediction from the preceding model and model specific inputs. The prediction from the preceding level is used to focus the higher level model on specific "hot spots", and outcomes of the performance predictions from each level are synthesized by some multifidelity modeling technique, *c.f.* [13, 14, 15]. Model specific inputs at each level may include probabilistic descriptions that are likely related to the improved physics model. The hierarchy can continue to burrow down in length scale as long as there is sufficient value in adding more layers. This follows the development of a similar tool, called DDSim, that was designed to make fatigue life predictions [3, 4]. The intent is to start with relatively low-cost computational tools and gradually increase the fidelity by improving the physical models, presumably at greater cost. Thus, Level I sacrifices accuracy, emphasizing speed and volume, while the finest length scale considered, Level XX, is computationally heavy yet very physically accurate.

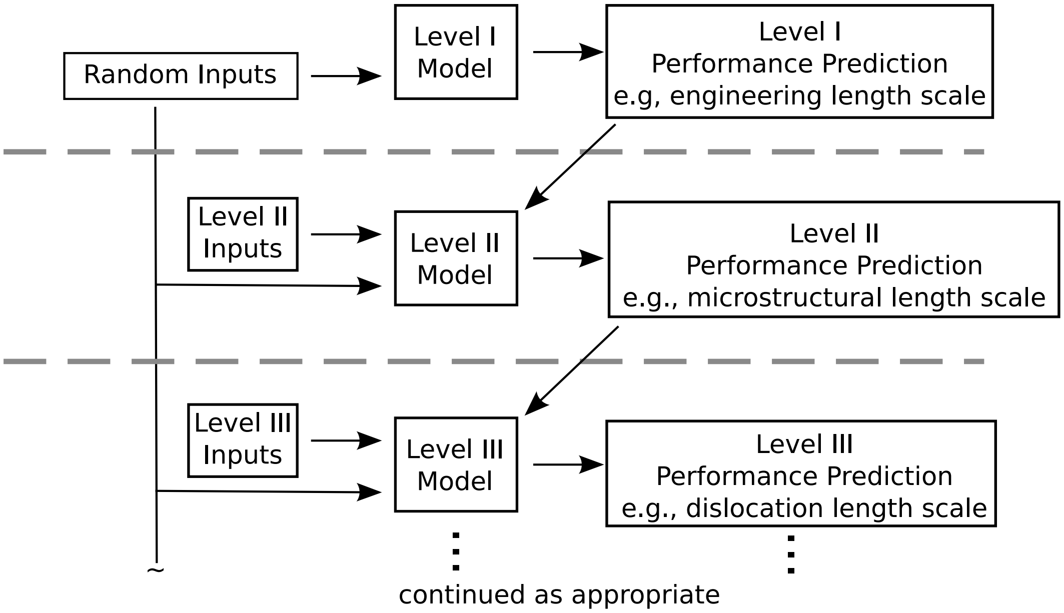

Figure 1.2: Schematic flowchart of the hierarchical multiscale approach.

To illustrate the application of the hierarchy to our solid mechanics problem, consider Figure 1.3, which illustrates an arbitrary solid defined on spatial domain $\mathcal{D} \subset \mathbb{R}^3$ subjected to applied load q. It is of interest to determine, for example, the load q at which the solid fails. In reality, the material makeup of the solid has random defects, spatial inhomogeneities, and other variabilities that lead to general uncertainty in the material behavior. Because of this, the load at which failure occurs is uncertain and treated as a random variable, denoted by Q. Our objective is to determine the probability law of Q. There are many choices of models to account for the materials defects, but in this work we consider modes at two distinct length scales: the Engineering length scale, S, which assumes spatial homogeneity, and the Microstructural length scale M, which includes details of the materials' microstructure.

Ideally, we would use the fine scale M model everywhere in $\mathcal{D}$, and perform direct Monte Carlo simulation by drawing many random samples of M and computing the corresponding samples of Q, the load at failure. This approach is not feasible for two reasons. First, the computational cost associated with using the fine scale material model is so great that its use must be limited to a small spatial subset of the domain $\mathcal{D}_M \subset \mathcal{D}$. Second, performing this type of calculation thousands of times as needed for traditional Monte Carlo is also not

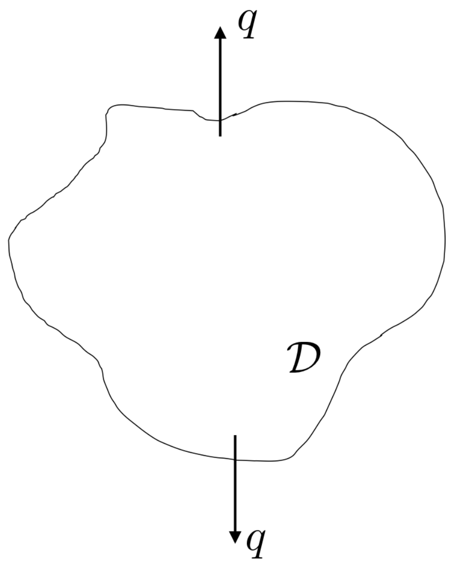

Figure 1.3: Arbitrary solid subjected to applied load.

feasible. The first reason can be addressed by multiscale calculations while utilizing the fine scale material model at a *carefully chosen and finite* number of spatial subdomains, perhaps one location at a time. The use of stochastic reduced order models (SROMs) has been shown previously to be one possible solution for the second reason. We will make use of the SROM here, too.

The algorithm for our solid mechanics problem looks like this:

1. Assemble a model for the solid with the engineering scale material model S. Draw one sample of S and compute the corresponding sample of loading Q at failure; also observe and record the spatial location of failure.
2. Repeat step 1 as many times as possible to achieve a low fidelity estimate of the probability law of failure $\Pr_L(Q \leq a)$ as well as an idea of where the "hot spots" are located and how likely failure is to occur at each location.
3. Partition domain $\mathcal{D}$ into n non-overlapping regions $\mathcal{D}_1, \ldots, \mathcal{D}_n$ as illustrated by Fig. 1.4.
4. Insert the fine scale material model M into region $\mathcal{D}_k$ and use the engineering scale material model S everywhere else, that is, in $\mathcal{D} \setminus \mathcal{D}_k$. We represent this modeling scenario with notation $(\mathcal{D} \setminus \mathcal{D}_k = S, \mathcal{D}_k = M)$.
5. Construct an SROM for the random parameters associated with $(\mathcal{D} \setminus \mathcal{D}_k = S, \mathcal{D}_k = M)$ and compute the corresponding probability law of Q, the load at failure. Let $\mathcal{F}_k$ denote the event that failure occurs in region $\mathcal{D}_k$, then in this step we have computed $\Pr_H(Q \leq a \mid \mathcal{F}_k)$, the probability of failure conditioned on the event occurring in regiong $\mathcal{D}_k$.
6. Repeat steps 4 and 5 for a selection of the n regions illustrated by Figure 1.4.

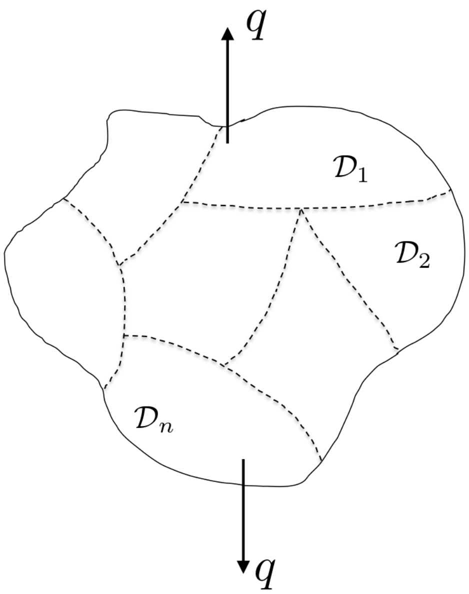

Figure 1.4: Spatial partition of solid into n regions.

With $\mathcal{F}_k$ denoting the event that failure occurs in region $\mathcal{D}_k$. The high fidelity probability law of Q can then be quantified by the theorem of total probability, *i.e.*,

$$\Pr_H(Q \leq a) = \sum_{k=1}^{n} \Pr_H(Q \leq a \mid \mathcal{F}_k) \Pr(\mathcal{F}_k) \tag{1.1}$$

where the marginal probabilities $\Pr(\mathcal{F}_k)$, $k = 1, \ldots, n$, can be estimated by step 2 above. Note further that low fidelity estimates of the conditional probability $\Pr_L(Q \leq a \mid \mathcal{F}_k)$ can be obtained from step 2. In the case that there is very low, or zero, probability for a subregion, the low fidelity estimate for conditional probability could be used in Equation 1.1, thus saving the considerable computational effort of coupling the microstructure in that region.

In this report for crack nucleation in thin sheet form AA 6061-T6, we use a Hill plasticity [7] constitutive model with damage [8] to relate stress with strain for the materials behavior at the engineering scale S. Our model for the fine scale M explicity includes a model for the geometry of the grains with a crystal plasticity constitutive formulation [10] governing the deformation behavior. Further, we explicitly include a model for the geometry of a sub-grain second-phase particle, assuming it behaves rather simply with elastic or elastic-power-law-hardening constitutive behavior. Both S amd M are assumed to contain materials uncertainties that are propagated with liberal application of SROMs. The higher-fidelity model couples S with M through multiscale calculations, either with a domain decomposition method using multipoint constraints (MPC) to achieve the coupling or with sub-modeling for one-way coupling.

Chapter 2

Material form and behavior of the AA 6061-T6

This work focused on AA 6061-T6 rolled plate because it was readily available and affordable, it is frequently used in nuclear weapons and aerospace applications, and it has been richly studied in the literature, *c.f.*, [16, 17, 18, 19, 20, 21]. The latter point alleviates to some degree the requirement for us to dive deeply into the exploration of mechanisms and materials science because we can leverage the work of previous investigators. Nevertheless, we needed to collect data and information about a specific material for for our purposes. This chapter describes the material we used in our investigation and provides some details on the characterization of it.

2.1 Metallurgical details of AA 6061-T6

This work studied strain localization and damage progression in AA 6061-T6 rolled plate form. A single 1.2 m x 1.2 m x 0.8 mm (4 ft x 4 ft x 0.032 in) plate was procured from Alcoa Inc. via McMaster-Carr. The composition of the plate is listed in Table 2.1 below. A few key structural properties from the manufacturer are listed in Table 2.2.

	Si	Fe	Cu	Mn	Mg	Cr	Zn	Ti	Al (bal)
% alloy	0.63	0.4	0.24	0.05	1.0	0.17	0.03	0.02	97.46

Table 2.1: The chemical composition of AA 6061-T6 plate.

UTS (MPa)	337
Yield Stress (MPa)	276
Elongation (%)	13.8

Table 2.2: Mechanical properties of AA 6061-T6 from the manufacturer.

As shown in Table 2.1, several alloying elements are present. These elements primarily take the form of precipitates with a size of roughly 0.2 μm and inclusions around 5 μm as shown in Figure 2.1. Later in this work, we attempt to explicitly include the larger particles in a FE mesh to study the effects the surrounding matrix on the load in the particle. X-ray diffractions was used to investigate the composition of these precipitates and inclusions. The elemental peaks are shown in Figure 2.2. Spatial distributions of elements are shown in Figure 2.3. Most of the inclusions are Si and Mg with some are Fe-bearing particles also present. The precipitates are too small to be resolved with X-ray diffraction, but are thought to be of similar composition.

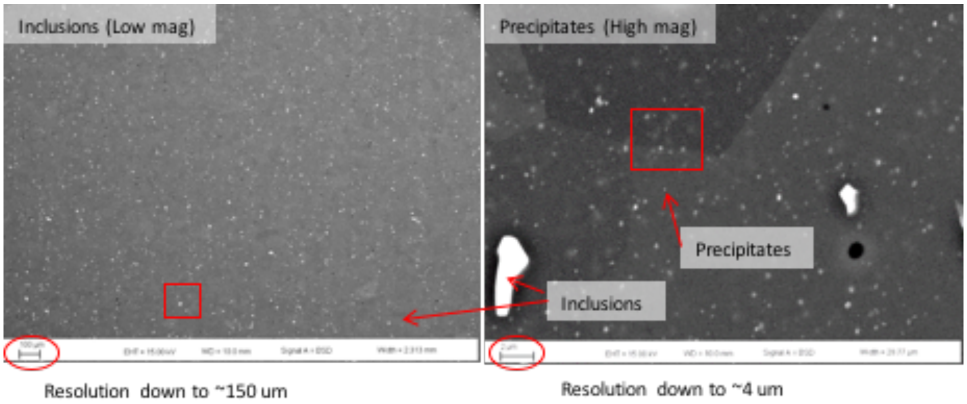

Figure 2.1: Micrographs showing inclusions and precipitates in AA 6061-T6. Originally, it was thought that these might provide a basis for a DIC speckle pattern, but they are too sparse and they lose contrast upon loading.

Electron backscatter diffraction (EBSD) was performed on samples of this material to establish the grain size, grain aspect ratio, and texture. The coordinate system used for crystallographic data is shown in Figure 2.4. EBSD maps are shown in Figure 2.5. From these figures, it is apparent that the grains have a diameter of approximately 50 μm in the normal plane direction. In the other directions, the grains are elongated in the rolling direction so that their widths are approximately 20 μm. Pole and inverse pole figures of the crystallographic texture are shown in Figure 2.6 and 2.7. There is a texture of strong 100 orientation with respect to the rolling direction and 110 orientation with respect to the other two.

Crystallographic orientation can also be quantified with three rotations, known as Euler angles, which can be calculated from the EBSD measurements. The Euler angles describe the orientation of the crystal lattice with respect to the lab reference frame as described by rotations from the reference in a specified pattern. There are many choices for convention, but here we follow the z-x-z convention. The first angle rotates the crystal away from the reference frame about the z-axis of the reference frame. The second angle rotates the lattice about the current x-axis. The final angle rotates the lattice about the current z-axis again. Figure 2.8 plots the normalized histograms for each of the three Euler angles from the plan EBSD measurements.

Following [22] one can compute the rotation matrix for crystal A from the euler angles

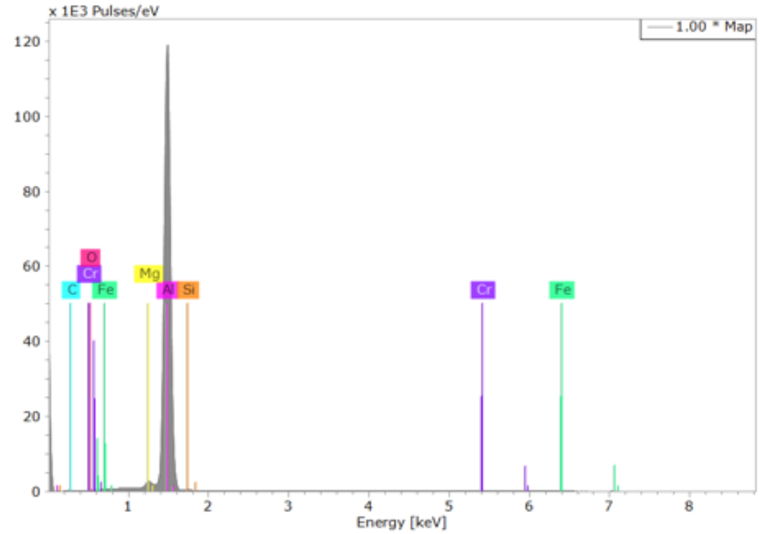

Figure 2.2: X-ray diffraction peaks showing some of the detected elements in this alloy.

using

$$g_A = \begin{bmatrix} c1c3 - s1c2s3 & s1c3 + c1c2s3 & s2s3 \\ -c1s3 - s1c2c3 & -s1s3 + c1c2c3 & s2c3 \\ s1s2 & -c1s2 & c2 \end{bmatrix} \tag{2.1}$$

where $c1$ is the cosine of the first Euler angle, $c2$ is the cosine of the second Euler angle, $c3$ is the cosine of the third Euler angle, $s1$ is the sine of the first Euler angle, $s2$ is the sine of the second Euler angle, and $s3$ is the sine of the third Euler angle. To describe the orientation of one grain with respect to another grain, on can write the rotation of grain B with respect to grain A's orientation as

$$g_B = \Delta g_{AB} g_A \tag{2.2}$$

so that

$$\Delta g_{AB} = g_B g_A^{-1} \tag{2.3}$$

describes the rotation from grain A to grain B. Converting this to the axis/angle convention for describing crystallographic orientation yields a measure or the grains' misorientation given as

$$\Theta = arccos((tr(\Delta g_{AB}) - 1)/2) \tag{2.4}$$

where $tr(\bullet)$ represents the sum of the diagonal of the matrix. The misorietation angles for each of the plan, longitudinal and transverse EBSD data are plotted in Figure 2.9.

Ductile fracture is attributed to the mechanisms of void nucleation, growth and coalescence. This has been studied extensively over the course of time and there are a nice series of papers in particular on AA 6061-T6 [16, 18, 17, 21]. The findings in these papers provided partial motivation for our focus on AA 6061-T6. Given the complexities of modeling growth and coalescence at the mesoscale, we've chosen to focus on nucleation, which requires a clear definition. In general, void nucleating sites in an alloy can be attributed to a vast number of properties ranging from lattice vacancies to grain boundary imperfections to other-phase

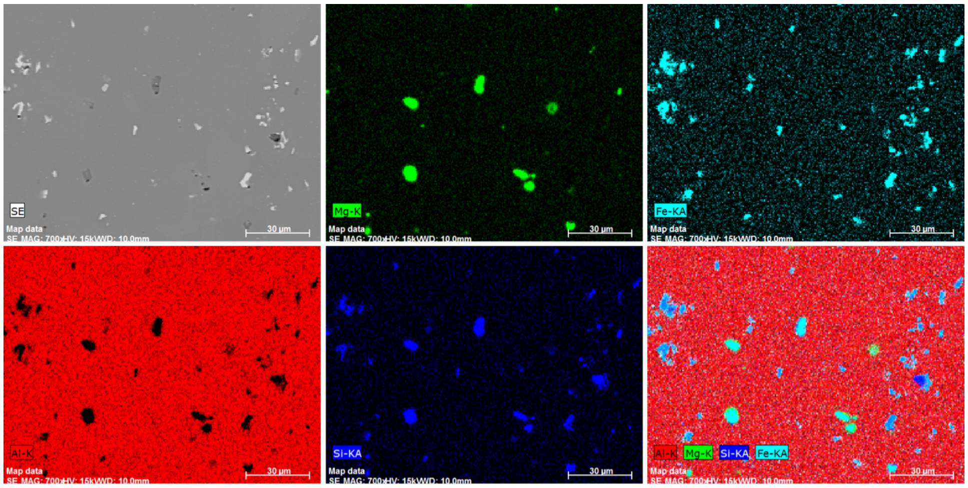

- Very fine precipitates of Fe (~1um) throughout specimen.
- Larger precipitates of Mg_2Si and of Fe on the scale of 10 um.

Figure 2.3: Spatial distribution of chemical constitituents measured by X-ray diffraction for AA 6061-T6 rolled plate.

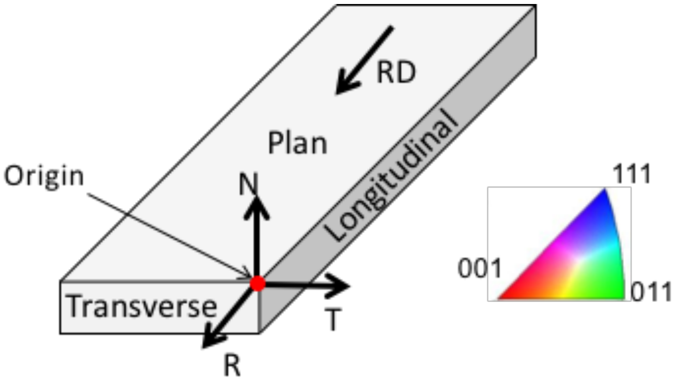

Figure 2.4: Orientation convention for crystallographic plots.

particles and inclusions. For the aluminum alloy we're focused on, our measurements above, which are confirmed in the literature, show there are nominally two populations of second-phase for concern, see Figure 2.3. There are finer, micron-size iron (Fe) precipitates, and there are larger, 10 mm magnesium-silicon (Mg2Si) and iron precipitates, which refer to as particles. From careful consideration of the image in Figure 2.3, the average particle dimensions are taken to be $5\mu m$ in the rolling direction with waste of $2\mu m$. It may be unconventional to discuss future work in the introductory chapter, but the bimodality of the precipitate size suggest the idea of coupling damage nucleation and growth models to account for the finer precipitates, with crystal plasticity models that explicitly include the larger particles in the mesh. The size and spacing of the larger particles would set a length scale, so local damage models would be convergent [23].

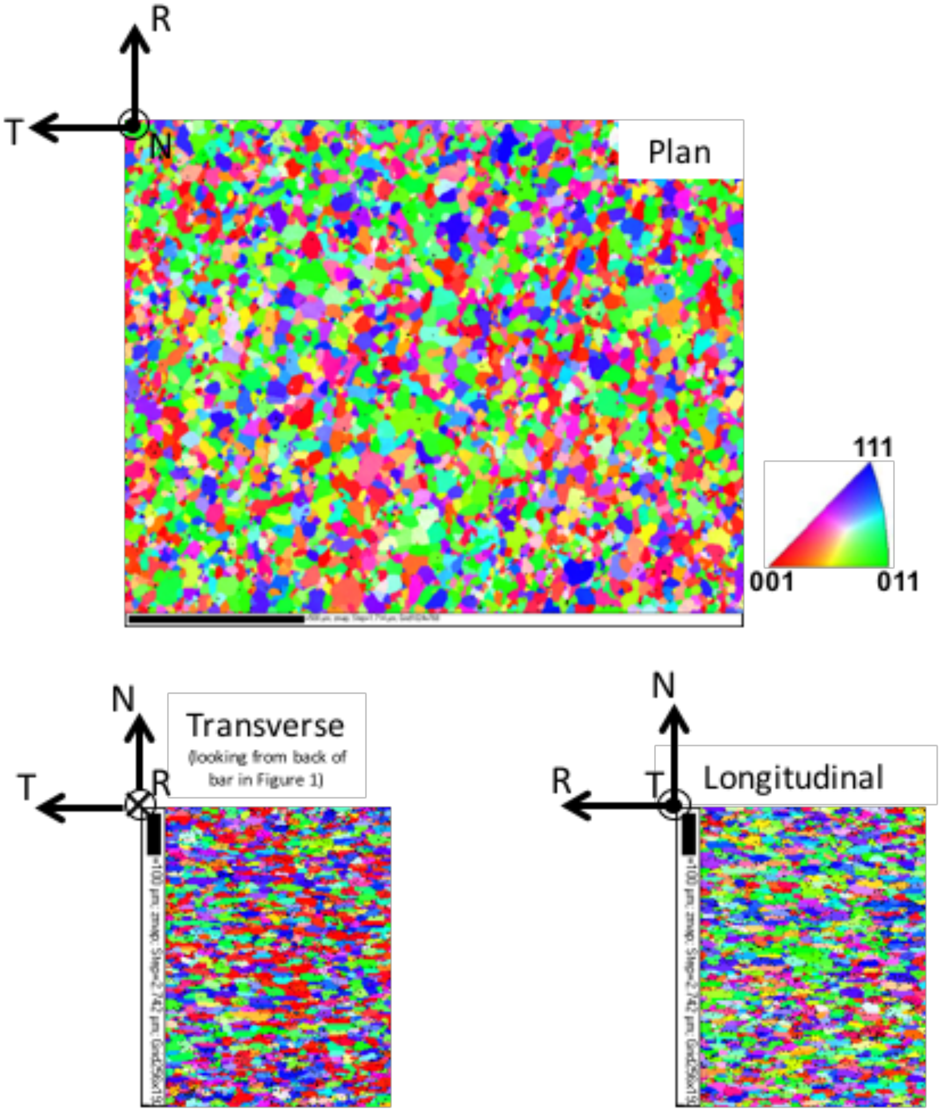

Figure 2.5: EBSD maps from three primary directions of the plate colored according to the legend in Figure 2.4 with respect to the direction of view (normal, rolling, and transverse respectively).

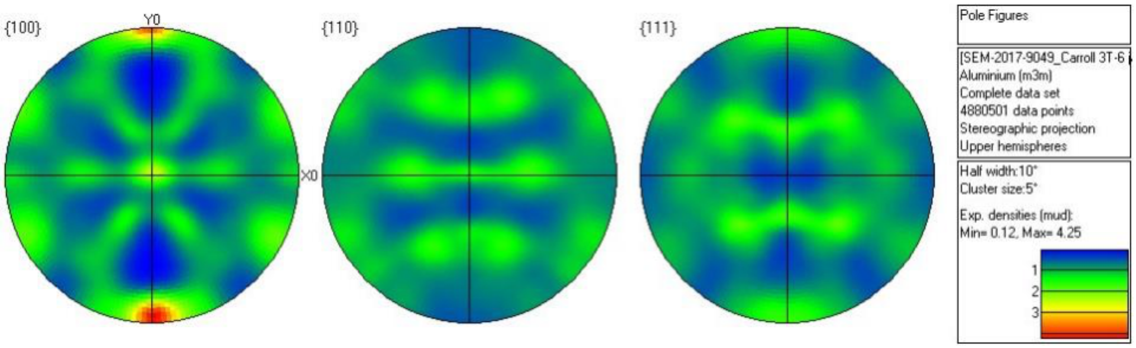

Figure 2.6: Pole figures showing the texture of the AA 6061-T6. There is some preference for [100] texture in the rolling direction and a slight [110] bias in the other two directions. This is similar to a Goss texture.

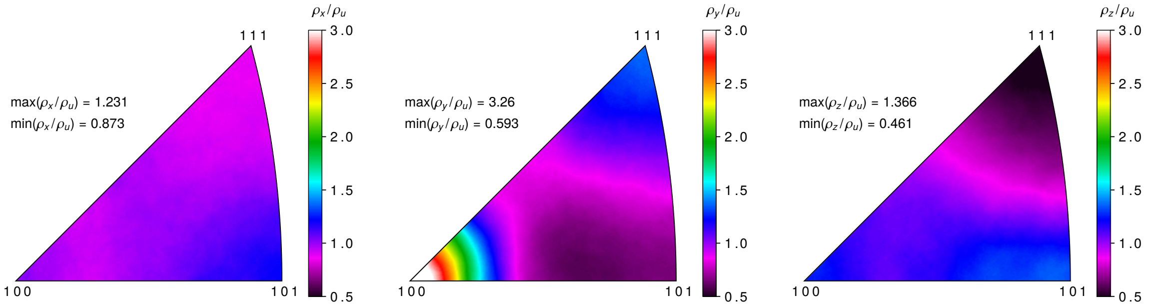

(a) Plan T (b) Plan R (c) Plan N

Figure 2.7: Inverse pole figures of the AA 6061-T6 microstructure showing a 100 texture in the rolling direction with a slight secondary 111 rolling texture and preferential 100 and 110 orientations in the normal direction.

2.2 Specimens

Approximately 200 specimens of five types were cut from the sheet of AA 6061-T6 in both the rolling and transverse direction including dogbone tension specimens, 2-notch-sharp, 2-notch-gradual, and 6-notch specimens with dimensions shown in the drawings included in Appendix B. Tension specimens were created to characterize base material properties and natural variability. The 2-notch sharp and gradual specimens test the variability associated with strain localization for differing triaxialities. Figure 2.10 shows an example of the notched specimens with a faile sharp-notced specimen.

Figure 2.11 plots engineering stress-strain curves for the smooth, gradual-notched, and sharp-notched tensile specimens in both rolling and transverse directions. The plasticity behavior is apparently anisotropic and relatively repeatable, or deterministic, however there is a wide range in strain to failure. Note that the data as presented has been smoothed and spline fit for convenience in further processing. These data are used in Chapter 6 to calibrate an engineering scale plasticity model.

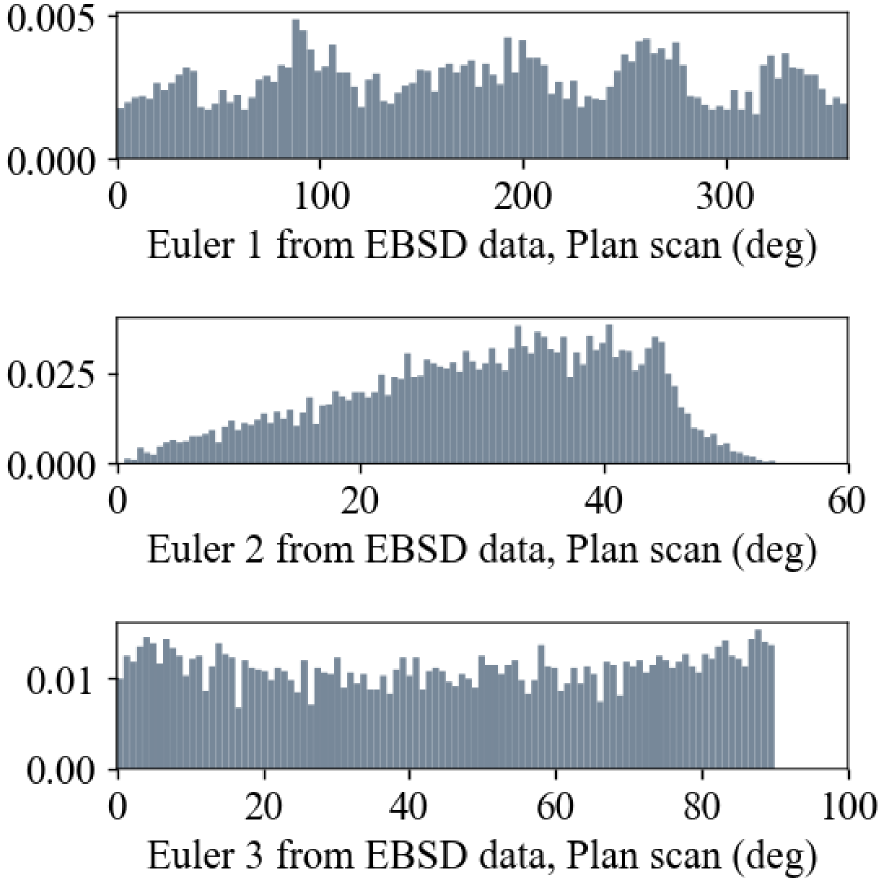

Figure 2.8: Normalized histograms of the Euler angles from the plan EBSD measurement.

The 6-notch specimens were designed to investigate stochastic failure with multiple possible crack initiation locations, and are discussed in further detail in the subsequent chapters. The tension and two-notch specimens were generally inputs into models whereas the 6-notch specimens served as validation target specimens. Figure 2.12 shows a series of medium magnification images at the root of the notches. The nucleation event was dominated in the middle set of notches. Figure 2.13 shows the performance of the 6-notched specimens with load normalized by the nominal plate area (not including the notches). Again, the plasticity of the plates is repeatable with variability arising in strain-to-failure.

A senior design project was leveraged at Howard University to compliment this project. In one year, a team of four undergraduate seniors built a tensile testing load frame, building on progress in previous years. They also set up the load frame for in situ DIC measurements. Sandia support not only included guidance, but also the delivery of 50 of the 4-notch specimens for testing at Howard university. The results from those studies primarily focused on specimen-to-specimen variability in force and displacement. For more details, the reader is referred to the report [24].

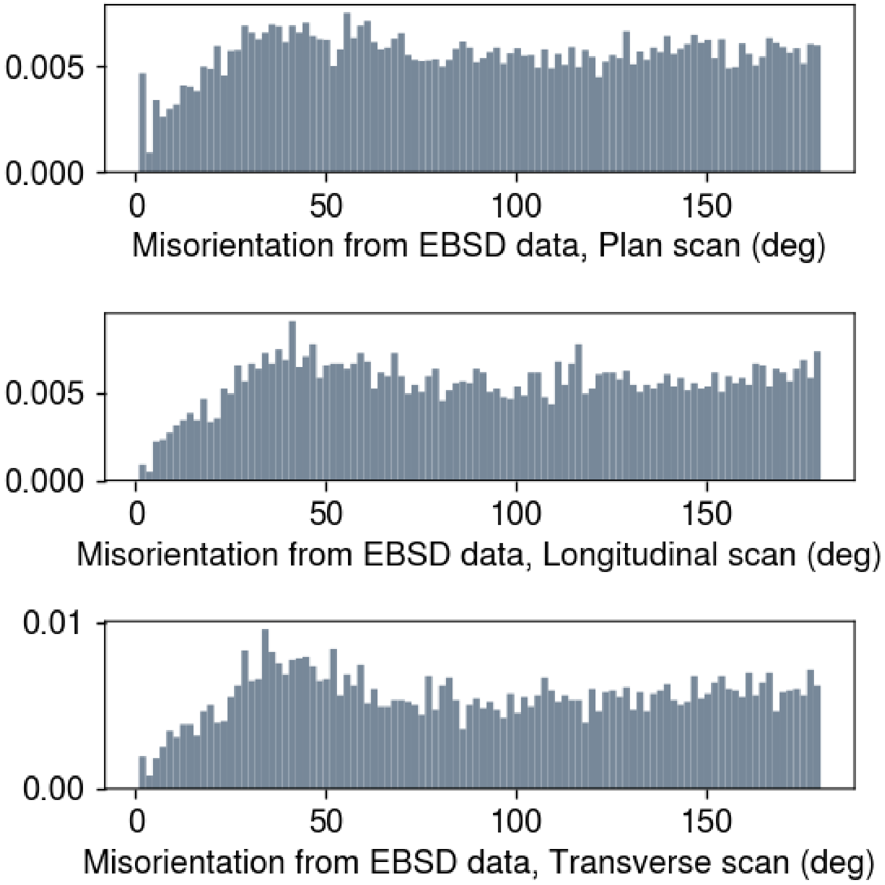

Figure 2.9: Normalized histograms of the lattice misorientations from the plan, longitudinal, and transverse EBSD measurements.

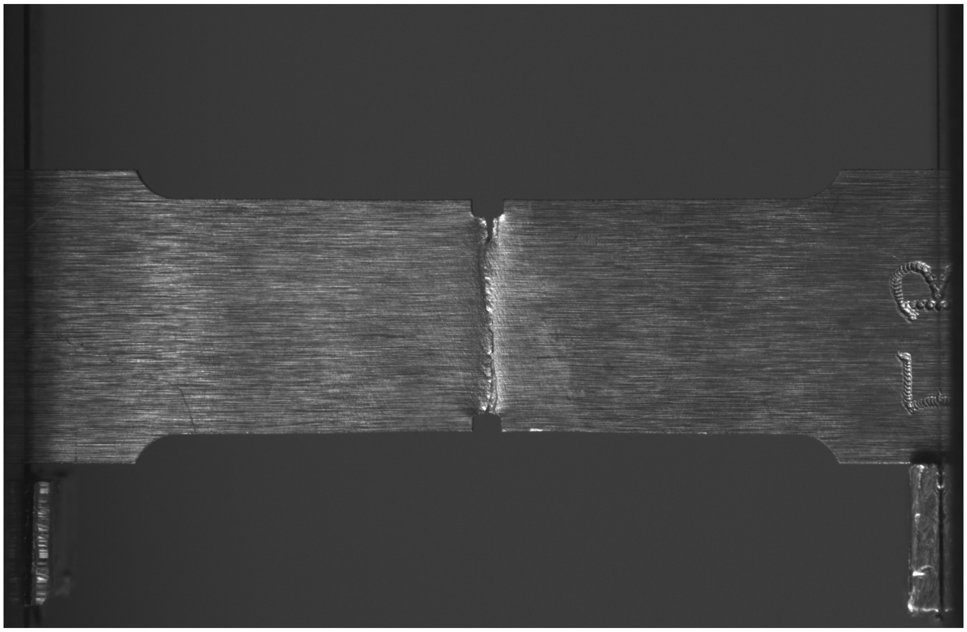

Figure 2.10: In situ image of a broken sharp-notch specimen.

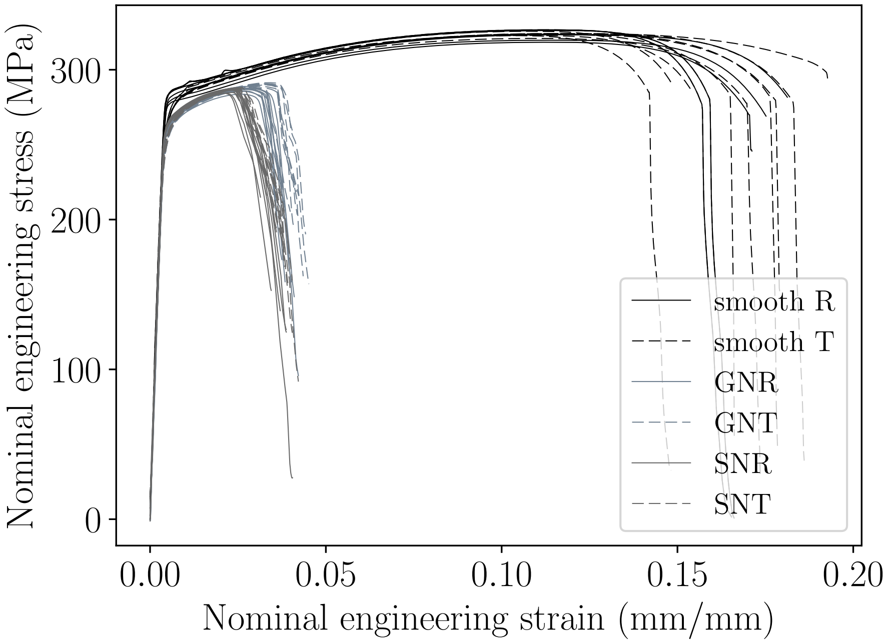

Figure 2.11: Engineering stress-strain curves for a the smooth, gradual-notched (GN), and sharp-notched (SN) tensile specimens in both rolling (R) and transverse (T) directions used for characterization.

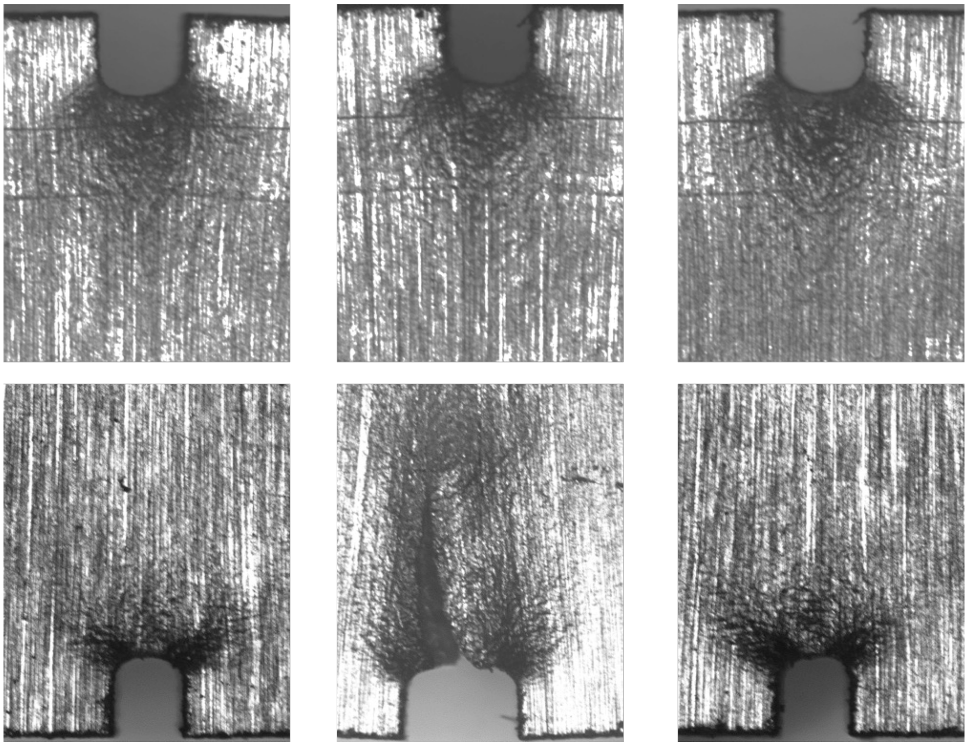

Figure 2.12: Series of medium magnification images at the root of the six notches. Fracture sets up in the middle set of notches.

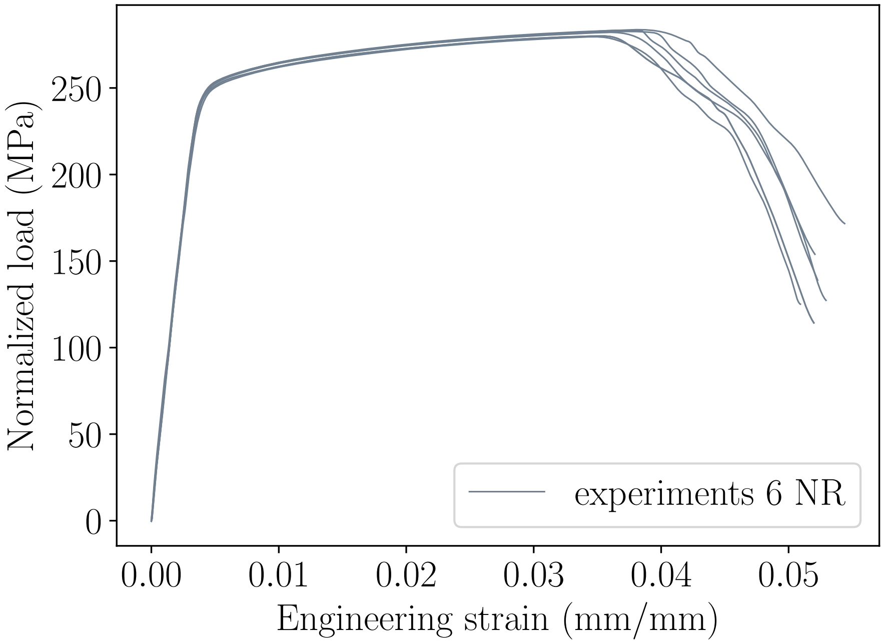

Figure 2.13: Normalized load versus strain curves for a the 6-notched tensile specimen serving as our “idealized component” for model validation.

Chapter 3

Microstructure modeling

A key element in the research is development of tractable computational microstructural models to predict crack nucleation events. We employ a very basic crystal plasticity model to account for crystallographic slip [10], noting that like multiscale numerical methods this is an active area of research at Sandia with which we intend to intersect in the future [12, 25]. So far, we are focused on texture, that is, the distribution of crystallographic orientation in a polycrystal [22]. We are interested in how texture affects the homogenized response of a polycrystal, and its effects on the statistical distribution of, *e.g.* maximum stress/strain in an idealized second-phase particle. To study the effects on the homogenized response we have developed some so-called voxellated, or overlay, geometries whereby the grains are constructed by overlaying a Poisson Voronoi tessellation onto a uniform hexahedra mesh of varying densities [26, 27] and textures are generated with a random field model following [28]. In this Chapter we discuss the vector-valued random-field models for texture, a reduced-order version of it, geometry and mesh model concerns for generating polycrystals with second-phase particles, and we present some observations from meso-structural calculations.

3.1 Translation model for generating polycrystalline texture models

Let $\mathbf{\Theta}(\mathbf{x}) = (\Theta_1(\mathbf{x}), \Theta_2(\mathbf{x}), \Theta_3(\mathbf{x}))'$ denote a model for the three Euler angles that decribe the crystallographic orientation at a location of interest $\mathbf{x} \in D \subset \mathbb{R}^3$ in a material microstructure. The proposed model, developed by Arwade and Grigoriu [28], is a translation random field, a particular type of non-Gaussian random field defined by a nonlinear, spatially invariant, mapping of a Gaussian random field. This approach has several advantages that make it attractive for problems of this type: (1) one can match any non-Gaussian marginal distribution; (2) one can match the covariance function of the non-Gaussian field, with some exceptions; (3) the method is conceptually simple; and (4) the generation of random samples via Monte Carlo simulation is straightforward and efficient.

3.1.1 Analysis of the available EBSD data

Electron backscattered diffraction (EBSD) measurements of the three Euler angles describing crystallographic orientation of the ductile polyscrystalline AA 6061-T6, discussed in Chapter 2, are analyzed. The data have been recorded at n distinct locations (or grid points) within a domain of interest, D. The data are denoted by $\{\psi_{j,k} = \psi_j(\mathbf{x}_k),\ j = 1,2,3,\ k = 1,\ldots,n\}$, where subscripts j and k are indices on the coordinate of the vector of Euler angles and spatial location, respectively. Three data sets are available for study. Data sets #1, #2, and #3, which are of size $\mathbf{n} = \{n_j,\ j = 1,2,3\} = \{1866, 6610, 1938\}$, describe the crystallographic orientation of the aluminum alloy in the longitudinal, plan, and transverse directions, respectively. The scanned area for each directional data set is roughly $\mathbf{a} = \{a_j = l_j \times h_j,\ j = 1,2,3\} = \{l_1 \times h_1, l_2 \times h_2, l_3 \times h_3\}$. Histograms of $\{\psi_j(\mathbf{x}_k),\ j = 1,2,3,\ k = 1,\ldots,n_j\}$ for the longitudinal direction of the aluminum alloy can be seen in Figures 3.1(a),(c), and (e). The measurement locations, $\{\mathbf{x}_k, k = 1,\ldots,n_j\}$, for the longitudinal direction can also be seen in Figures 3.1(b), (d), and (f).

3.1.2 Analysis of Euler angle experimental observations for the purpose of informing the translation random vector model

We will make the following assumptions about the experimental data,

1. All measurements are made without error;
2. The measurements come from a statistically homogeneous and mean-square ergodic random field with finite variance;
3. The covariance function of the random field is isotropic; and
4. The correlation length normalized by the average grain size is approximately the same for each data set.

By assumption 2, we can treat the measurements $\{\psi_{jk}\}$ as independent samples of random field $\mathbf{\Theta}(\mathbf{x})$. Therefore,

$$\hat{\mu}_j = \frac{1}{n}\sum_{k=1}^{n} \psi_{j,k},\ \hat{\sigma}_j^2 = \frac{1}{n-1}\sum_{k=1}^{n} \left(\psi_{j,k} - \hat{\mu}_j\right)^2,\ \text{and}\ \hat{F}_j(\theta) = \frac{1}{n}\sum_{k=1}^{n} 1(\psi_{j,k} \leq \theta) \tag{3.1}$$

provide estimates of $\mu_j = \mathrm{E}[\Theta_j(\mathbf{x})]$, $\sigma_j^2 = \mathrm{Var}[\Theta_j(\mathbf{x})]$, and $F_j(\theta) = \Pr(\Theta_j(\mathbf{x}) \leq \theta)$, the mean, variance, and marginal probability distribution of $\Theta_j(\mathbf{x})$, $j = 1,2,3$. Estimates of the means and standard deviations are listed in Table 6.4.

By assumption 4, the average grain size is an important feature of the data. To define this quantity, let

$$\delta_j = \min_{\substack{k=1,\ldots,n \\ k \neq j}} \|\mathbf{x}_j - \mathbf{x}_k\| \tag{3.2}$$

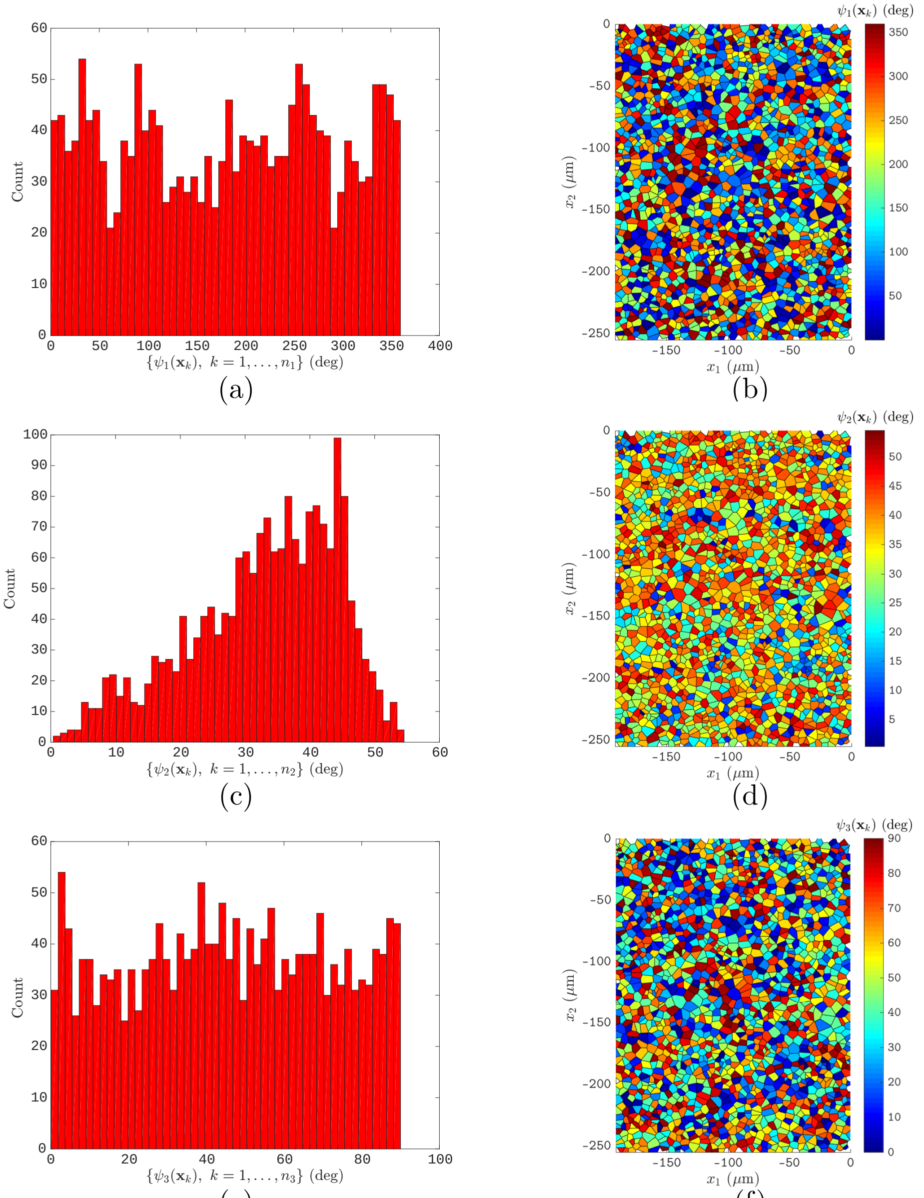

(a) (b) (c) (d) (e) (f)

Figure 3.1: Histogram and measurement locations of $\{\psi_j(\mathbf{x}_k), j=1,2,3, k=1,\ldots,n_j\}$ for the longitudinal direction of the aluminum alloy. The presented histograms illustrate the difference in the PDFs of the euler angles (a) $\{\psi_1(\mathbf{x}_k,\ k=1,\ldots,n_1\}$, (c) $\{\psi_2(\mathbf{x}_k,\ k=1,\ldots,n_2\}$, and (e) $\{\psi_3(\mathbf{x}_k,\ k=1,\ldots,n_3\}$. The measurement locations are also illustrated for (b) $\{\mathbf{x}_k, k=1,\ldots,n_1\}$, (d) $\{\mathbf{x}_k, k=1,\ldots,n_2\}$, and (f) $\{\mathbf{x}_k, k=1,\ldots,n_3\}$. The voronoi tessellation is included for visualization; additionally, the color map indicates the value of the corresponding $\{\psi_j(\mathbf{x}_k),\ j=1,2,3,\ k=1,\ldots,n_j\}$.

denote the distance between grid j and its nearest neighbor; $\delta_j > 0$ can be interpreted as the "size" of the grain centered at grid $\mathbf{x}_j$, and $\delta_{\text{avg}} = (1/n)\sum_{j=1}^{n}\delta_j$ denotes the average grain size.

Data set	Orientation	Mean (deg)	Standard deviation (deg)
#1	Longitudinal	$(181.4, 32.85, 45.54)'$	$(106.8, 11.33, 25.75)'$
#2	Plan	$(181.8, 30.13, 45.42)'$	$(99.86, 11.37, 26.97)'$
#3	Transverse	$(181.4, 30.70, 44.27)'$	$(108.7, 14.13, 22.59)'$

Table 3.1: Sample mean and standard deviation of Euler angles.

Next consider two locations $\mathbf{u}, \mathbf{v} \in D$ and let

$$\xi_{kl}(\mathbf{u}, \mathbf{v}) = \xi_{kl}(\|\mathbf{u} - \mathbf{v}\|) = \frac{\mathrm{Cov}\,(\Theta_k(\mathbf{u}), \Theta_l(\mathbf{v}))}{\sigma_k\, \sigma_l}, \quad k, l = 1, 2, 3, \tag{3.3}$$

be scaled versions of the covariance functions of $\boldsymbol{\Theta}(\mathbf{x})$, where the first equality is true by assumption 3. We can obtain estimates of $\{\xi_{kl}\}$ using the available data $\{\psi_{j,k} = \psi_j(\mathbf{x}_k),\ j = 1, 2, 3,\ k = 1, \ldots, n\}$. The auto- $\xi_{k,l}$ $k = l$ and cross-covariances $\xi_{k,l}$ $k \neq l$ are along the top and bottom rows, respectively. The plots indicate that the correlation length for data set #1 is roughly 1-2 times the average grain size, and roughly 3-4 times the average grain size for data set #2. In addition, there is little if any cross-correlations among the different angles. The red curves, corresponding to estimates made from data set #2, are smoother than the blue curves because data set #2 is almost four times larger than data set #1.

It is convenient to approximate the scaled covariance functions defined by Eq. (3.3) by exponential functions of the following form

$$\xi_{kl}(\eta) \approx \gamma_{kl}\, e^{-\alpha_{kl}\, \eta}, \tag{3.4}$$

where α_{kl} and γ_{kl} are constants satisfying $\alpha_{kl} > 0$, $\gamma_{kk} = 1$, and $-1 < \gamma_{kl} < 1$, $k \neq l$. Estimates for these parameters can be obtained by least-squares minimization and are listed in Table 3.2. We make use of these approximations when calibrating the model proposed in the following section.

It should be noted that in data sets #1 and #3, some off-diagonal terms of $\hat{\alpha}_{kl}$ are estimated to be of value ∞. By Equation 3.4, this simply implies that the correlation lengths of these off-diagonal terms are 0. The physical interpretation of this implication is that the grains in the orientation of interest are not correlated with respect to those Euler angles. For example, in data set #1, it is noted that $\hat{\alpha}_{3,2} = \hat{\alpha}_{2,3} = \infty$. This ultimately indicates that for the longitudinal orientation, the Euler angles ψ_2 and ψ_3 are not correlated.

3.1.3 Vector-valued translation random field model definition

Let $\mathbf{G}(\mathbf{x}) = (G_1(\mathbf{x}), G_2(\mathbf{x}), G_3(\mathbf{x}))'$ be a vector-valued homogeneous and isotropic Gaussian random field with zero mean, unit variance, and covariance functions $\rho_{kl}(\|\mathbf{u} - \mathbf{v}\|) = \mathrm{E}[G_k(\mathbf{u})\, G_l(\mathbf{v})]$, $k, l = 1, 2, 3$. Our proposed model for $\boldsymbol{\Theta}(\mathbf{x})$ is defined as a simple nonlinear

Data set	Orientation	$\{\hat{\alpha}_{kl}\}$	$\{\hat{\gamma}_{kl}\}$
#1	Longitudinal	$\begin{pmatrix} 0.945 & 0.363 & 0.662 \\ 0.363 & 0.263 & \infty \\ 0.662 & \infty & 2.00 \end{pmatrix}$	$\begin{pmatrix} 1 & 0.0134 & -0.037 \\ 0.0134 & 1 & -0.006 \\ -0.036 & -0.006 & 1 \end{pmatrix}$
#2	Plan	$\begin{pmatrix} 0.279 & 0.068 & 0.064 \\ 0.068 & 0.048 & 0.184 \\ 0.064 & 0.184 & 0.245 \end{pmatrix}$	$\begin{pmatrix} 1 & -0.007 & 0.008 \\ -0.007 & 1 & 0.008 \\ 0.008 & 0.008 & 1 \end{pmatrix}$
#3	Transverse	$\begin{pmatrix} 0.534 & \infty & \infty \\ \infty & 1.016 & 0.338 \\ \infty & 0.338 & 2.212 \end{pmatrix}$	$\begin{pmatrix} 1 & 0.024 & 0.011 \\ 0.024 & 1 & 0.014 \\ 0.011 & 0.014 & 1 \end{pmatrix}$

Table 3.2: Estimates of parameters for exponential fit to scaled covariance functions defined by Eq. 3.4 for each data set.

transformation of $\mathbf{G}(\mathbf{x})$, called a translation random field [29, Section 5.3.3]. The form of the transformation is given by [28],

$$\boldsymbol{\Theta}(\mathbf{x}) = \boldsymbol{\mu} + \mathbf{a}\,\mathbf{Y}(\mathbf{x}) = \begin{pmatrix} \mu_1 \\ \mu_2 \\ \mu_3 \end{pmatrix} + \begin{pmatrix} \sigma_1 & 0 & 0 \\ 0 & \sigma_2 & 0 \\ 0 & 0 & \sigma_3 \end{pmatrix} \mathbf{Y}(\mathbf{x}), \tag{3.5}$$

where $\mathbf{Y}(\mathbf{x})$ is a vector-valued translation random field with zero mean, unit variance, and coordinates,

$$Y_k(\mathbf{x}) = h_k(G_k(\mathbf{x})) = F_k^{-1} \circ \Phi(G_k(\mathbf{x})),\ \ k = 1, 2, 3, \tag{3.6}$$

each F_k is a cumulative distribution function (CDF) satisfying,

$$\int_{\mathbb{R}} u \,\mathrm{d}F_k(u) = 0 \quad \text{and,} \quad \int_{\mathbb{R}} u^2 \,\mathrm{d}F_k(u) = 1,$$

and $\Phi(z) = (2\pi)^{-1/2} \int_{-\infty}^{z} e^{-u^2/2}\,\mathrm{d}u$ denotes the CDF of the standard Gaussian random variable. We can show that $\boldsymbol{\Theta}(\mathbf{x})$ is a homogeneous and isotropic random field with the following properties,

1. The mean value of the random field is constant and equal to $\boldsymbol{\mu}$ defined by Eq. (3.5), *i.e.*, $\mathrm{E}[\Theta_k(\mathbf{x})] = \mu_k$. Likewise, the standard deviation of each coordinate is constant and equal to σ_k, $k = 1, 2, 3$.

2. The marginal CDF of Y_k is F_k defined by Eq. (3.6). It follows that $\Pr(\Theta_k(\mathbf{x}) \le z) = F_k((z - \mu_k)/\sigma_k)$, $k = 1, 2, 3$, are the marginal CDFs of $\boldsymbol{\Theta}(\mathbf{x})$.

3. $\mathbf{Y}(\mathbf{x})$ is a homogeneous and isotropic random field with covariance functions

$$\begin{aligned}\xi_{kl}(\|\mathbf{u}-\mathbf{v}\|) &= \mathrm{E}[Y_k(\mathbf{u})\,Y_l(\mathbf{v})] \\ &= \mathrm{E}[h_k(G_k(\mathbf{u})\,h_l(G_l(\mathbf{v}))] = \int_{\mathbb{R}^2} h_k(y)\,h_l(z)\,\phi_2(y,z;\rho_{kl}(\|\mathbf{u}-\mathbf{v}\|))\,\mathrm{d}y\,\mathrm{d}z,\end{aligned} \tag{3.7}$$

where,

$$\phi_2(y,z;\rho) = \frac{1}{2\pi\sqrt{1-\rho^2}}\exp\left(-\frac{y^2-2\,y\,z\,\rho+z^2}{2(1-\rho)^2}\right)$$

denotes the joint probability density function (PDF) of two standard Gaussian random variables with correlation ρ. It follows that the covariance functions of $\boldsymbol{\Theta}(\mathbf{x})$ are $\sigma_k\,\sigma_l\,\xi_{kl}(\eta)$.

3.1.4 Model calibration and implementation of translation model

The calibration and implementation of the previously defined model for generating polycrystalline orientations represented as proper Euler angles is rather straightforward and can be accomplished in a relatively simple manner. The process for calibrating the model is as follows,

1. Set the elements of $\boldsymbol{\mu}$ and $\mathbf{a}$, as denoted in Equation 3.5, equal to the estimates of $\hat{\mu}_k$ and $\hat{\sigma}_k$, $k = 1, 2, 3$, which are defined in Equation 3.1;
2. Use estimates of $\hat{F}_k$, defined in Equation 3.1, for the CDFs F_k in the mappings $h_k(G_k(\mathbf{x})) = F_k^{-1} \circ \Phi(G_k(\mathbf{x}))$, $k = 1, 2, 3$;
3. Set the covariance functions $\{\xi_{kl}\}$ defined by Equation 3.7 equal to the approximations for $\{\xi_{kl}\}$ defined by Equation 3.4, where the parameters $\hat{\alpha}_{kl}$ and $\hat{\gamma}_{kl}$ are determined via experimental observations; and
4. Solve Equation 3.7 for $\{\rho_{kl}\}$, the covariance functions of $\mathbf{G}(\mathbf{x})$, where $\mathbf{G}(\mathbf{x})$ is the Gaussian image of $\boldsymbol{\Theta}(\mathbf{x})$.

It is useful to further elaborate on Step 4. Given a value of ρ_{kl}, we solve Equation 3.7 to obtain the corresponding value for ξ_{kl}; the integration is typically done numerically. This procedure is repeated for different values of ρ_{kl} until the interval $-1 \leq \rho_{kl} \leq 1$ is sufficiently represented, resulting in a collection of $\{(\rho_{kl}, \xi_{kl})\}$. Linear interpolation on this collection can then be used to determine ρ_{kl} for a specified value of ξ_{kl}.

Once the translation model has been calibrated using experimental observations, creating samples of $\boldsymbol{\Theta}(\mathbf{x})$ on an arbitrary finite element (FE) mesh becomes exceedingly straightforward and involves three steps. The process for generating samples of $\boldsymbol{\Theta}(\mathbf{x})$ is as follows,

1. Generate samples of Gaussian random field $\mathbf{G}(\mathbf{x})$ over the FE mesh;
2. Using Equation 3.6, translate the samples of $\mathbf{G}(\mathbf{x})$ to obtain the corresponding samples of $\mathbf{Y}(\mathbf{x})$; and
3. Apply Equation 3.5 to shift and scale the samples of $\mathbf{Y}(\mathbf{x})$ to obtain the corresponding samples of $\boldsymbol{\Theta}(\mathbf{x})$.

Textures were generated for a synthetic microstructure using the translation random field model and calibrated to our EBSD data in Chapter 2. The texture samples were generated at grain centroids chosen by a Poisson close-packing algorithm [30], with a linear mapping applied in the normal direction to achieve approximate aspect ratio of the grains in our AA 6061-T6. Figure 3.2 shows inverse pole figure (IPF) plots of texture generated with the translation model for the three cases of no texture, macro- and micro-texture. A truly non-textured structure would be uniformly 1.0 times random in IPF magnitude and the samples generated with the translation model range from 0.92 to 1.12. The textured samples reasonably reproduce the EBSD data shown in Figure 2.3. It is not possible to differentiate between micro- and macro-texture with IPFs. For this, we use misorientation. Figures 3.3 – 3.5 plot histograms of the three Euler angles. Noteworthy, although well known in the texture analysis community, a naive approach to generate non-textured microstructures might be to choose three Euler angles with uniform distribution in some range of support. However, because of their relationship in the rotation matrix, which belongs to a special orthogonal group, the second Euler angle is not uniformly distributed. As with the pole figures, the textured samples reasonably reproduce the EBSD data shown in Figure 2.8.

Following the discussion in Chapter 2, we can compute misorientation for the samples from the translation model. Figure 3.6 plots the misorientation angles for the three models, no texture, macro-texture and micro-texture. The non-textured misorietations show tendency for grains to be more drammatically misoriented, with the density continuously rising from 0° to 180°. There are symmetries that could be employed that we neglect in these plot [31]. Otherwise, there are only subtle differences in the distributions of the macro- and micro-textured samples, with the micro-texture rising a bit more steeply for 0° and peaking a bit more sharply in the neighborhood of 30°.

3.1.5 Reduced-order model for vector-valued random field

In Section 3.1, we utilized a translation model to generate samples of the crystallographic orientation of a material of interest for an arbitrary 3D FE model. Using this methodology, one can generate a vast number of samples, which, depending on the refinement of the FE mesh, can be impractical to solve for all crystallographic orientation realizations due to computational cost and constraints. With this being the case, it would be useful to be able to select a small number of samples from the total number of generated crystallographic orientation realizations while maintaining relevant statistical characteristics. In light of this,

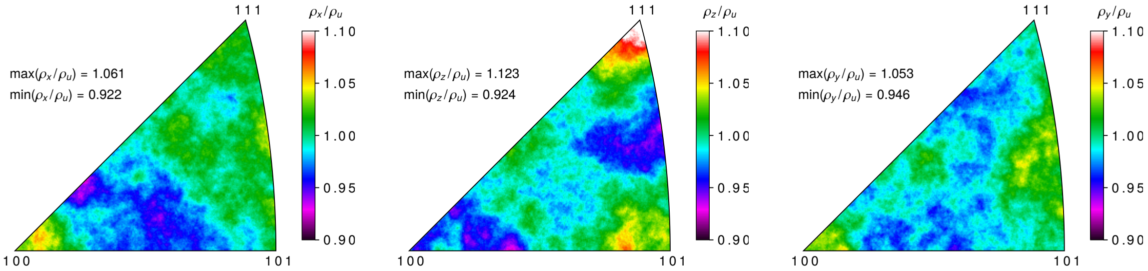

(a) Non-texture T (b) Non-texture R (c) Non-texture N

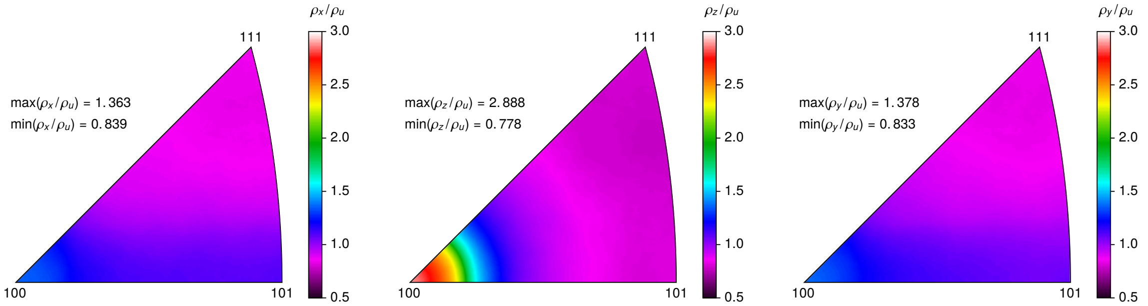

(d) Macro-texture T (e) Macro-texture R (f) Macro-texture N

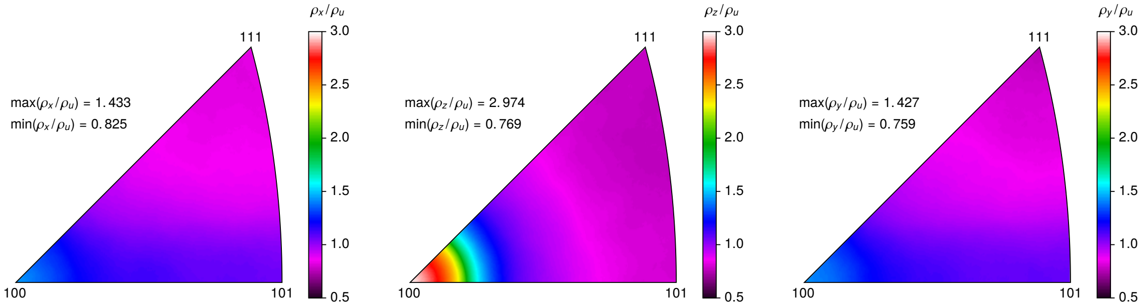

(g) Micro-texture T (h) Micro-texture R (i) Micro-texture N

Figure 3.2: Inverse pole figures from ensembles of non-, macro-, and micro-textured (top to bottom) 224-grain polycrystal samples.

we apply the stochastic reduced-order model (SROM) methodology developed by Grigoriu [32] to assist in the selection of a comparatively small number of samples which have been generated via the translation model methodology.

Let $\tilde{\mathbf{\Theta}}(\mathbf{x}) = \{\tilde{\boldsymbol{\theta}}(\mathbf{x})^{(1)}, \ldots, \tilde{\boldsymbol{\theta}}(\mathbf{x})^{(m)}\}$ be defined as elements of the SROM of $\mathbf{\Theta}(\mathbf{x})$, where $\{\tilde{\mathbf{\Theta}}(\mathbf{x}) : \tilde{\mathbf{\Theta}}(\mathbf{x}) \subset \boldsymbol{S}(\mathbf{x})\}$, where $\boldsymbol{S}(\mathbf{x})$ defines the support of $\mathbf{\Theta}$. The SROM samples have corresponding probabilities $(\tilde{p}^{(1)}, \ldots, \tilde{p}^{(m)})$, which are defined such that $\tilde{p}^{(i)} \geq 0 \; \forall \; i$, $i = 1, \ldots, m$, and $\sum_{i=1}^{m} \tilde{p}^{(i)} = 1$. The SROM sample, which is of size m, thus has the following sample-probability pairs, $(\tilde{\boldsymbol{\theta}}^{(i)}, \tilde{p}^{(i)})$, $i = 1, \ldots, m$. Additionally, the corresponding marginal cumulative distribution function, moments, and correlations are defined as,

$$\tilde{F}_k(\theta_k) = \Pr(\tilde{\Theta}_k \leq \theta_k) = \sum_{i=1}^{m} \tilde{p}^{(i)} \mathbf{1}(\tilde{\theta}_k^{(i)} \leq \theta_k), \tag{3.8}$$

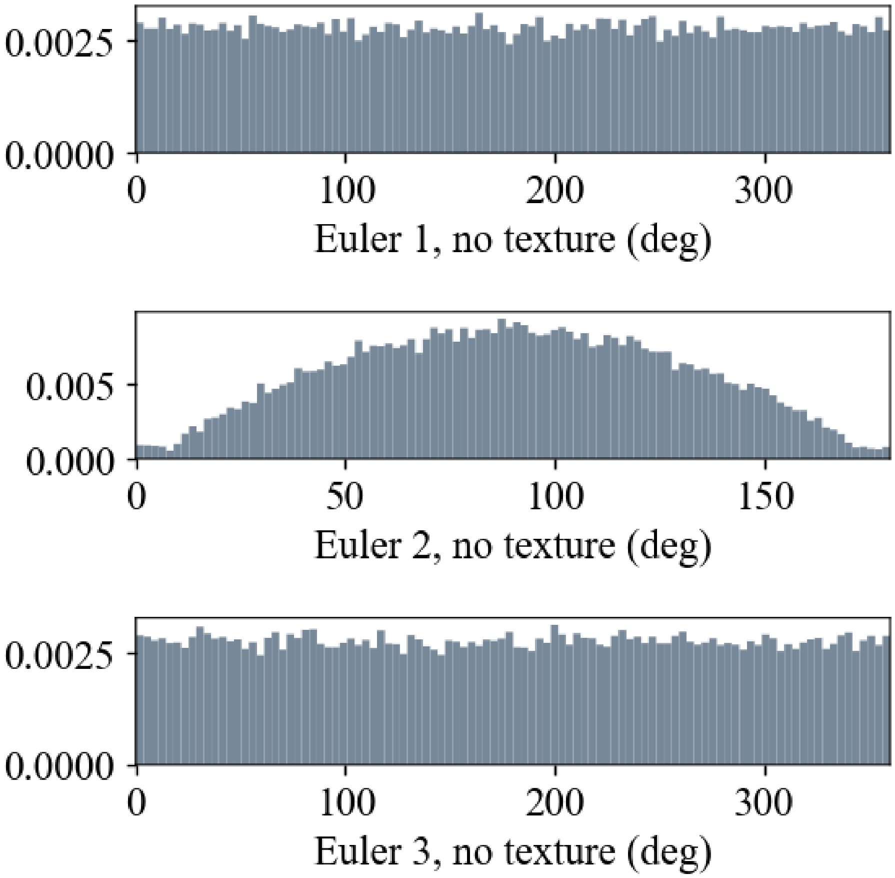

Figure 3.3: Histograms of the Euler angles from an ensemble of non-textured 224-grain polycrystal samples.

$$\tilde{\mu}_k(q) = \mathrm{E}[\tilde{\Theta}_k^q] = \sum_{i=1}^{m} \tilde{p}^{(i)} (\tilde{\theta}_k^{(i)})^q, \tag{3.9}$$

$$\tilde{c}(k,l) = \mathrm{E}[\tilde{\Theta}_k \tilde{\Theta}_l] = \sum_{i=1}^{m} \tilde{p}^{(i)} \tilde{\theta}_k^{(i)} \tilde{\theta}_l^{(i)}, \tag{3.10}$$

Where $\mathrm{E}[\cdot]$ is the expectation operator, $\mathbf{1}(\cdot)$ is the indicator function, and q is the order of the marginal moments. Using Equations 3.8–3.10, we can impose a criteria to choose the sample-probability pairs of the SROM to optimally represents the probability law of full set of realizations, by some measure. For example, we may use an objective function that seeks to minimize the error between the marginal distributions, moments, and correlations of $\boldsymbol{\Theta}$ and $\tilde{\boldsymbol{\Theta}}$. The expressions that define the error between the SROM and target marginal distributions, moments, and correlations are as follows,

$$\min \left\{ \sum_{r=1}^{3} w_r e_r(\mathbf{p}) \right\}, \tag{3.11}$$

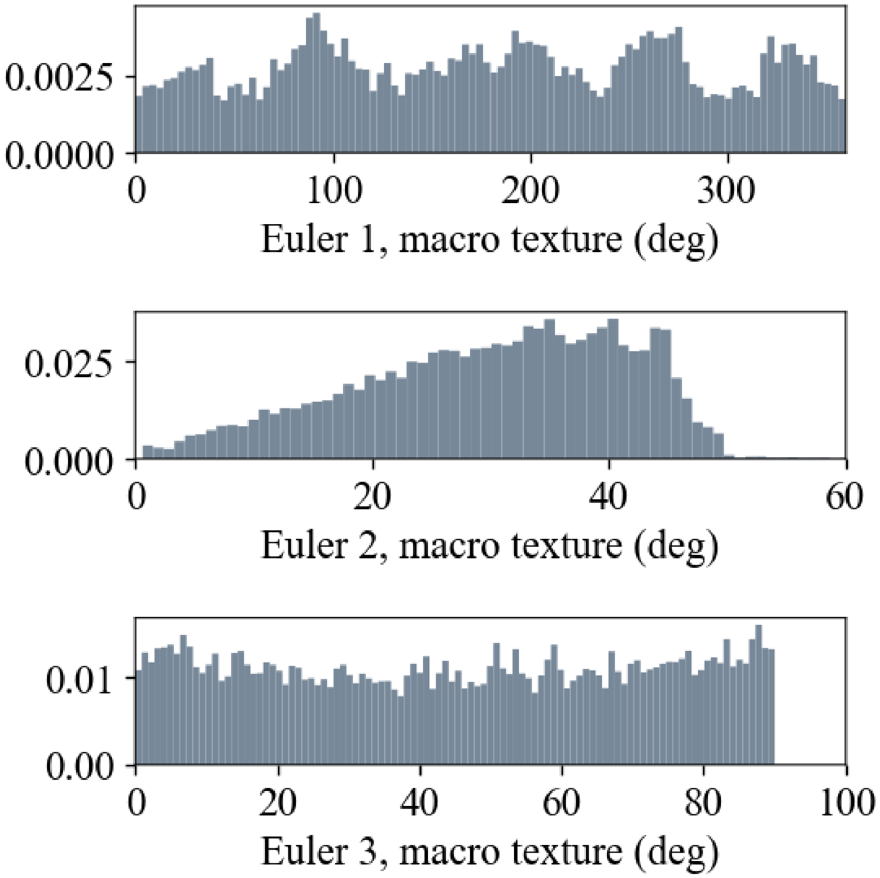

Figure 3.4: Histograms of the Euler angles from an ensemble of macro-textured 224-grain polycrystal samples.

where w_r are weight factors which are to be defined such that $w_r \geq 0$ and $\sum_{r=1}^{3} w_r = 1$ and e_r are discrepancy (or error) functions. For our purposes, the discrepancy functions seek to determine the difference between the marginal CDF, moments and correlations of $\boldsymbol{\Theta}$ and $\tilde{\boldsymbol{\Theta}}$. The generalized definition of e_r, where $r = 1, 2, 3$, is,

$$e_1(\mathbf{p}) = \max_{1 \leq k \leq 3} \; w_1 \left| \tilde{F}_k(x) - F_k(x) \right| , \tag{3.12}$$

$$e_2(\mathbf{p}) = \max_{1 \leq q \leq \bar{q}} \max_{1 \leq k \leq 3} \; w_2 \left| \tilde{\mu}_k(q) - \mu_k(q) \right| , \tag{3.13}$$

$$e_3(\mathbf{p}) = \max_{k,l} \; w_3 \left| \tilde{c}(k,l) - c_k(k,l) \right| , \tag{3.14}$$

where e_1, e_2, and e_3 denote the difference between the marginal CDF, moments, and correlations of $\boldsymbol{\Theta}$ and $\tilde{\boldsymbol{\Theta}}$, respectively, and $\bar{q}$ is the number of moments. By solving Equations 3.11-3.14, the max of the discrepancy between the $\boldsymbol{\Theta}$ and $\tilde{\boldsymbol{\Theta}}$ can be minimized, thus providing the optimal SROM $\tilde{\boldsymbol{\Theta}}$ of $\boldsymbol{\Theta}$.

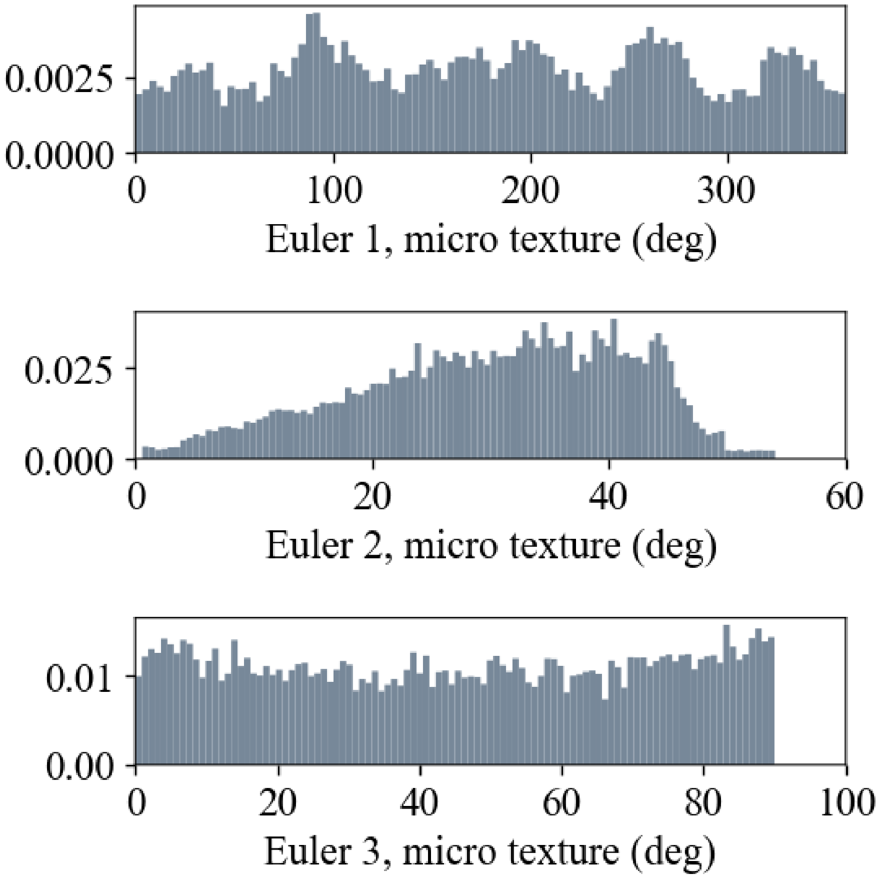

Figure 3.5: Histograms of the Euler angles from an ensemble of micro-textured 224-grain polycrystal samples.

3.2 Microstructure mesh model development

Much of the work in this project is completed using a microstructure model where the mesh does not conform to the polycrystal grain geometry. The details of that approach are discussed in Section 3.2.1. To better understand the implications of this scheme we compare these results with a model constructed using a new meshing tool called Sculpt that can produce meshes that conform with the grain geometry [2]. This scheme is discussed in Section 3.2.2. An artifact of the sculpting process is that it makes, sometimes not so subtle, changes to the underlying geometry. Because of this, it was not possible to compare directly the outcomes of an overlay microstructure with a sculpted microstructure. Consequently, a third scheme was devised so that the overlay was performed on a sculpted geometry, thus guaranteeing the geometry of the particle was consistent. This scheme is used to identify the influence of grain boundary treatment on particle breaking load and described in Section 3.2.3.

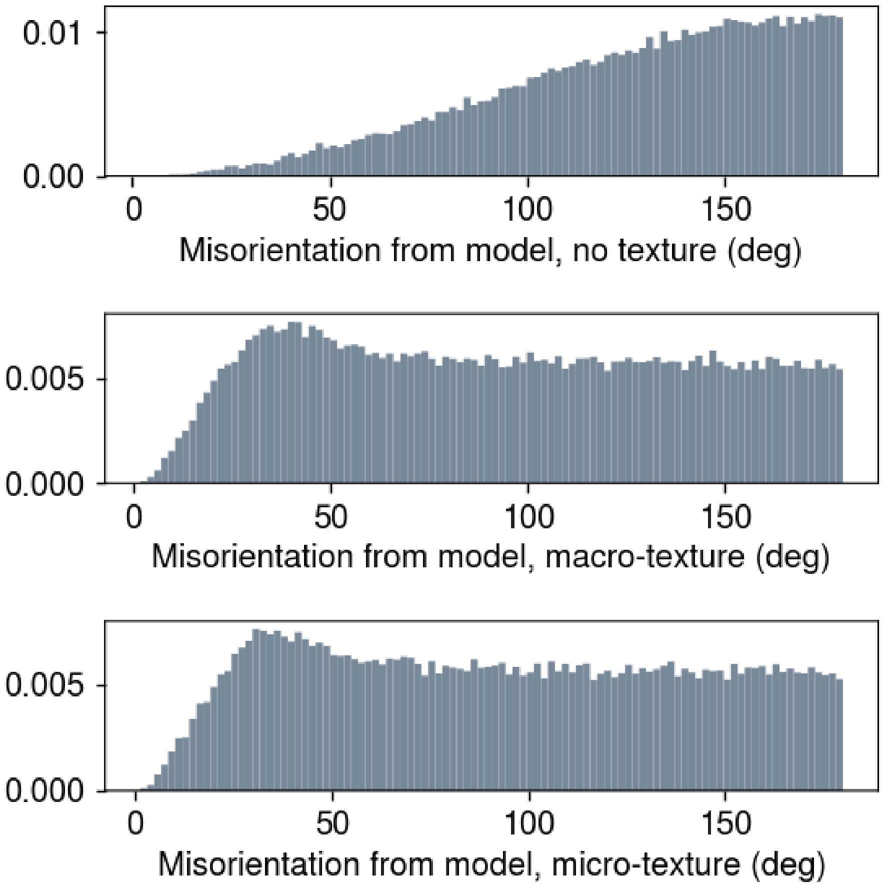

Figure 3.6: Histograms of the misorientation angles from ensembles of non-, macro-, and micro-textured (top to bottom) 224-grain polycrystal samples.

The following discussion holds for both a single-phase microstructure or a multi-phase microstructure. We generate single-phase microstructures to evaluate the effects of texture on yield behavior. We generate two-phase microstructures, including an idealized iron-bearing, second-phase particle, to study the load in the particle as a function of the texture model applied. The particle is idealized to have ellipsoidal geometry, which is a common but not accurate assumption, with approximate aspect ratio consistent with the average particle size observed in our AA 6061-T6.

3.2.1 Grain independent meshing

The simplest approach to incorporate the crystallographic structure into the FE model is to independently mesh the background geometry and overlay crystallographic details on the mesh. For this, we use a close-packing algorithm to generate a Voronoi tessellation describing grain centroids [30]. There are shortcomings in this approach to modeling grain morphology, but its accessibility is attractive. Subsequently, we loop through every element in the background mesh and assign the element properties, in our case grain orientations via Euler angles, based on the Voronoi cell the element is contained in. In Figure 6.7 this was performed with a background mesh of hexahedra elements. In the present discussion when we include a second-phase particle, we choose to use unstructured tetrahedral meshing. The outcome of the overlay approach at the intersection of several grains on the surface of a polycrystal model is shown in Figure 3.7. Because each element is independently assigned to its parent grain, with no smoothing along the grain boundary, the result is an artificially roughened grain surface whose tortuosity is dictated by the local mesh, not physics. For purposes of modeling fracture, a localization event that is driven by microstructural defects that cause stress concentrations, this artificial stress concentration is alarming. We continue to argue that, for our special case of aluminum matrix with a stiff and brittle second phase, the artificially roughened grain boundary might not be terribly dominant.

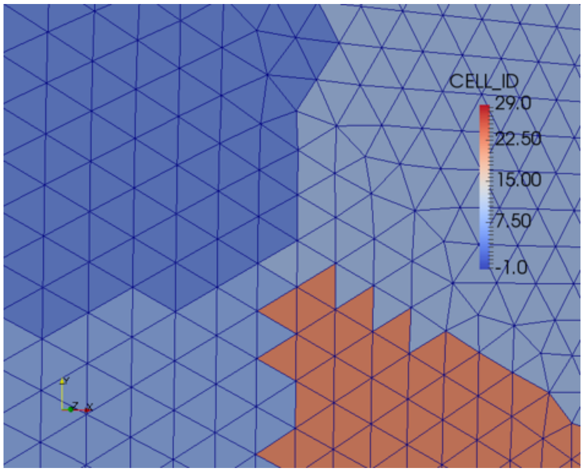

Figure 3.7: View of mesh using the overlay technique where elements do not conform to the grain boundaries

3.2.2 Grain boundary conforming meshing

To construct a finite element mesh that conform to the grain boundaries the Sculpt tool was used [2]. This tool constructs a hexahedral mesh that aligns with the defined boundaries. The input to Sculpt is a combination of an STL file defining the ellipsoid particle geometry and a Cartesian grid that defines the grains. The Cartesian grid is a voxellated representation of grain geometry similarly to the mesh constructed in Section 3.2.1 when hexahedral elements are used. Each cell in the Cartesian grid is assigned a parent grain. Sculpt smooths this jagged boundary definition to construct the mesh shown in Figure 3.8. There is a cost analysis that must be applied that balances the Cartesian grid spacing with smoothing to result in the most accurate microstructure. After meshing, grain orientation can be assigned to individual elements. Due to variations in the precise alignment of the grain boundaries in the Sculpt meshes it was chosen to assign grain orientation to all elements within a particular block otherwise a jagged boundary may still occur.

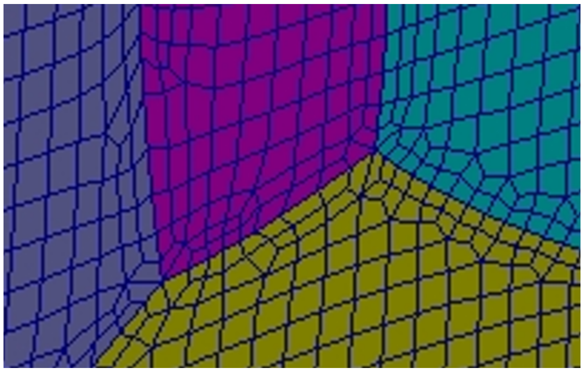

Figure 3.8: View of mesh where elements do conform to the grain boundaries

Significant complexity in the Sculpt meshing process arises from the smoothing and coarsening process that takes place internally due to the format of the grain definitions. Internally Sculpt converts the prescribed information to a grain density or 'volume of fluid' representation on each Cartesian grid cell. To remove the stair-stepped nature of the Cartesian grid, Laplace smoothing is performed. For continuity, the Laplace smoothing is forced on the ellipsoid inclusion geometry, which has also been converted to a volume-of-fluid representation internally. As the length scale of the ellipsoid inclusion is small relative to the grains the Laplace smoothing compresses further the size of the particle. There are some fundamental difficulties that arise from converting all the geometry to a volume-of-fluid representation and then operating on that. A hypothesis for future investigation is that retaining a level set implicit representation of geometry may alleviate some of the difficulties experienced by the Sculpt tool.

Additionally, our team supported an effort to strengthen the Sculpt and tetrahedral meshing tools available in Cubit. As such, we collaborated with the Sculpt development team during this work and discovered inconsistencies with the current parallel implementation of the Sculpt tool. For certain grain configurations some domain decompositions (number of processors) would result in a well formed mesh with no inverted elements while others would yield inverted elements. The meshing appears to be dependent on the the mesh partition in some non-obvious way. The adaptive mesh refinement feature was also found to be problematic. For microstructure meshes the adaptive mesh refinement feature in sculpt coarsens the mesh away from grain boundaries, which would be useful in constructing meshes that well represent the ellipsoid and grains while not being prohibitively expensive. The adaptive mesh refinement was found to generally yield inverted elements when prescribed for the meshing described in this work.

3.2.3 Consistent discretization of the second phase particle

There are three primary differences between the meshes of Sections 3.2.1 and 3.2.2: alignment of element faces with grain boundaries (a "smooth" grain boundary), the element type or topology (hexahedral versus tetrahedral) and finally the precision of the geometry of the second-phase particle. In the overlay approach, the particle geometry is consistent with the background geometry model in geometry and mesh modeling tool, Cubit in our case. Because of the Laplace smoothing in the BG-conforming approach, the geometry model for the particle can stray a long ways from ellipsoidal. Figure 3.9 shows an example of the differences in that can arise in the particle geometry. On the left side of the figure is the ellipsoidal particle included in the overlay approach, and on the right side of the figure is picture of a particle after the Laplace smoothing of Sculpt. The effects are random, dictated by the grain morphology, and increasingly deleterious as the disparity between particle size and grain size grows. For particles on the order of $5\mu m$ as measured for our AA 6061-T6, the effects can be quite bad. In this section we describe a meshing strategy that combines the discretized brittle inclusion geometry of Section 3.2.2 with the grain meshing scheme of Section 3.2.1.

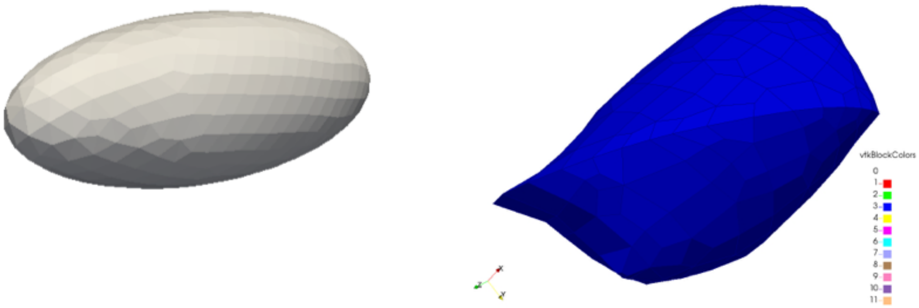

Figure 3.9: Comparison of tetrahedral meshed ellipsoid (left) and hexahedral meshed particle that comes out from Sculpt (right).

The process goes like this:

1. perform the meshing of Section 3.2.2;
2. load the mesh into the meshing software Cubit;
3. extract the discretized surface between the inclusion and the rest of the mesh;
4. convert that surface from quadrilaterals to triangles;
5. insert that surface in an analytically defined box (exterior of the mesoscale domain);
6. mesh that entire domain with tetrahedra; and finally,
7. perform the overlay process described in Section 3.2.1.

This procedure results in a tetrahedral mesh that does not conform to the grain boundaries, and that contains a particle domain whose geometry is correspondent to the equivalent microstructure resulting from the GB-comforming approach.

3.2.4 Comparing particle breaking load for GB-conforming and non-conforming microstructures

The primary objective in this section is to explore the effects of grain boundary conforming or non-conforming meshes on the particle breaking load. We want to use the overlay approach because it is faster, least pathological, and simpler to perform. We cannot directly compare results from the overlay approach to the GB-conforming approach because the particle geometry is so drastically different. So, we devised an approach to first Sculpt, changing the geometry of the particle, then overlay. Here we apply our meshing methods for a small polycrystal with 32 grains, one particle, and one realization of macro-texture. The model inclusion was five times larger than the average particle observed in our AA 6061-T6 and it was assumed to be pure iron with modulus of elasticity of 211 (GPa) and Poisson's ratio of 0.29. For these calculations, the particle is five times larger than the average particle in our AA 6061-T6 due to the pathologies of the sculpt meshing process, which had difficulties as the inclusion became small relative to the grain size.

Figure 3.10 shows the first principle stress contour plot for the two models: hybrid on the left; GB-conforming on the right. The figure shows cross-section through the polycrystal with normals to the rolling direction (top) and transverse direction (bottom) *with the particle removed*. The grain boundaries can be made out due to the stress fields, but there is not an obvious spike in the stress fields along the grain boundaries due to the non-conforming mesh scheme. Moreover, there is a philosophical debate to launch regarding our continuum representation of grain boundaries, but we won't digress down that path here. The stress at the interface between the inclusion and the crystalline matrix is noticeably higher in the tetrahedral mesh (left).

Figure 3.11 shows a more detailed view of the same stresses shown in Figure 3.10. The difference in stress is visible both at the inclusion-matrix interface as well as a region around that. In Figure 3.12 the pressure on the outer surface of the inclusion is shown for the tetrahedral mesh constructed according to Section 3.2.3. Here small elements with large pressure values are noticeable. The overall mesh quality on the surface and the geometric artifacts from Sculpt are visible.

In Figure 3.13 the difference in the stress-strain relationship for different meshing schemes is shown. These stress-strain curves plot the average first principle stress in the particle versus the nominal applied engineering strain on the representative polycrystal. The three different meshing schemes outlined in Section 3.2 are shown in addition to varying mesh refinement for each scheme. The red curves are results from the overlay scheme. The blue curves are results from the grain-boundary conforming scheme. The green curve is from the hybrid approach, which overlays the mesh with a particle geometry that came from Sculpt. We describe the curves in three regions: the primarily elastic region (steep initial slope), the transition to plasticity (abrupt change in slope in the curves) and the plastic deformation region. After plastic deformation develops (strains > 0.005) it is clear that the grain boundary conforming meshes (blue curves) describe a different particle response than the non-conforming scheme (red curves). Note, the plasticity in this case is in the surrounding matrix; the particle is

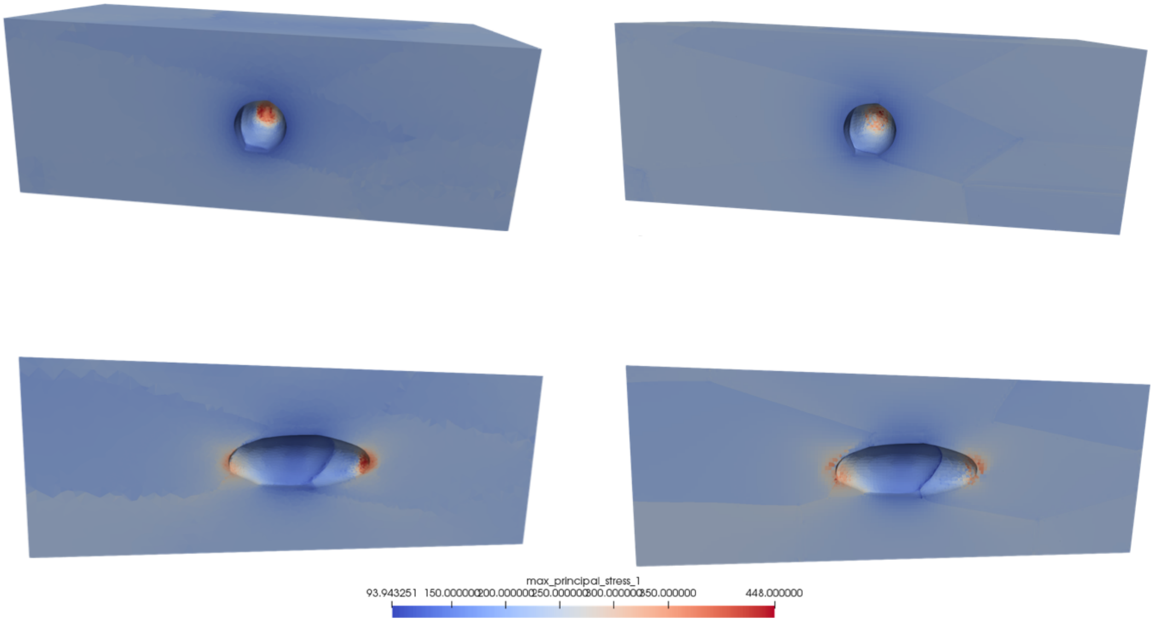

Figure 3.10: Comparison of principle stress at the inclusion-matrix boundary between tetrahedral mesh using scheme hybrid meshing scheme (left) and GB-conforming scheme (right).

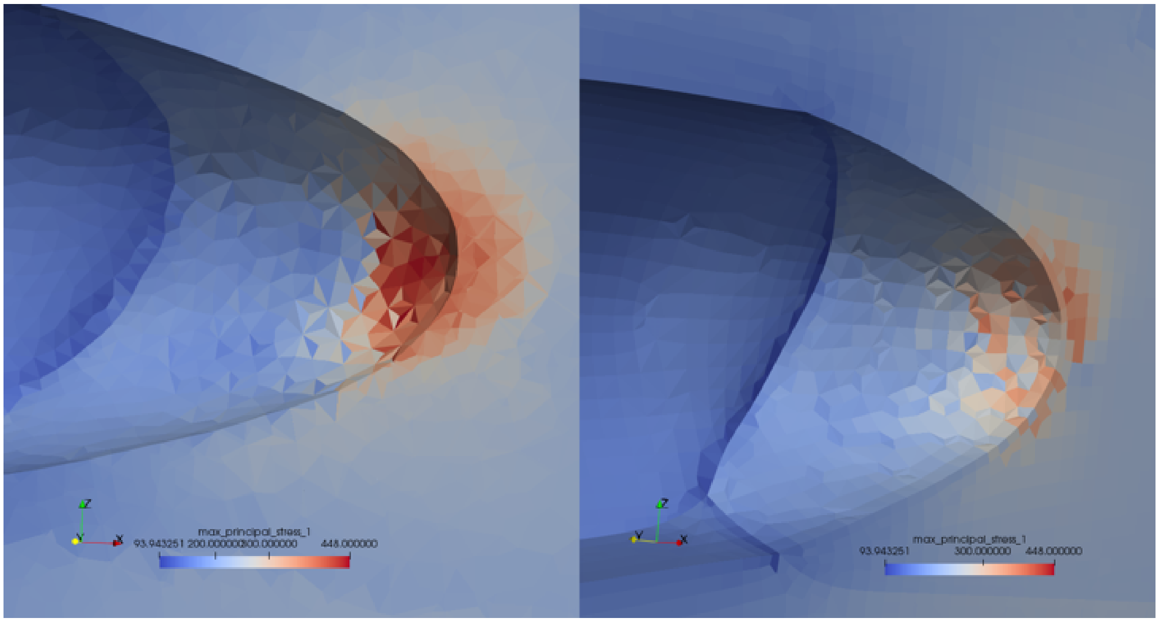

Figure 3.11: Zoomed view of differences in principle stress between the hybrid and GB-conforming approaches.

elastic. The grain conforming curves harden less then the non-grain-boundary-conforming curves. We suspected this was driven by effects of the Sculpt process on the geometry of the particle. Indeed, the response of the particle in the hybrid approach (green curve) lies directly atop the GB-conforming mesh results. It's not clear what role the 5x particle size

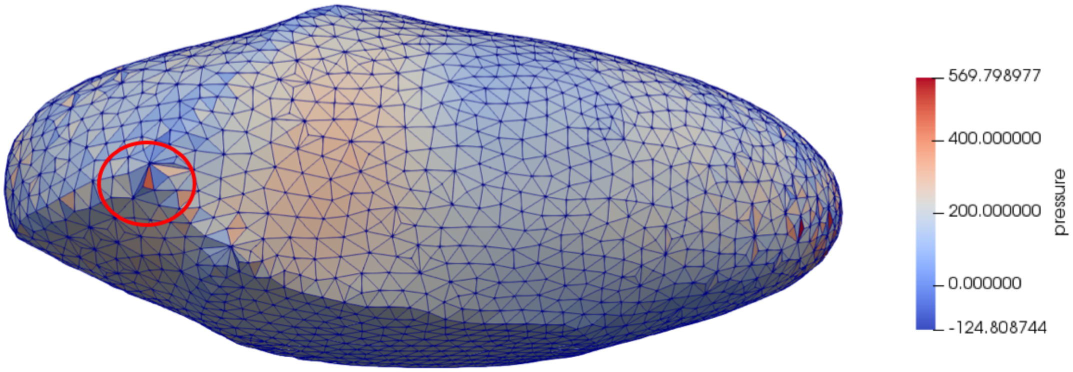

Figure 3.12: View of pressure at surface of inclusion for model constructed using the scheme of Section 3.2.3.

plays in these results and these results only include one realziation of macro-texture, but the conclusion from these results is important. Careful treatment of the grain boundaries when modeling a stiff particle in a soft matrix is unnecessary. The dominant fields are in the particle and remains unaffected by the treatment of the grain boundaries.

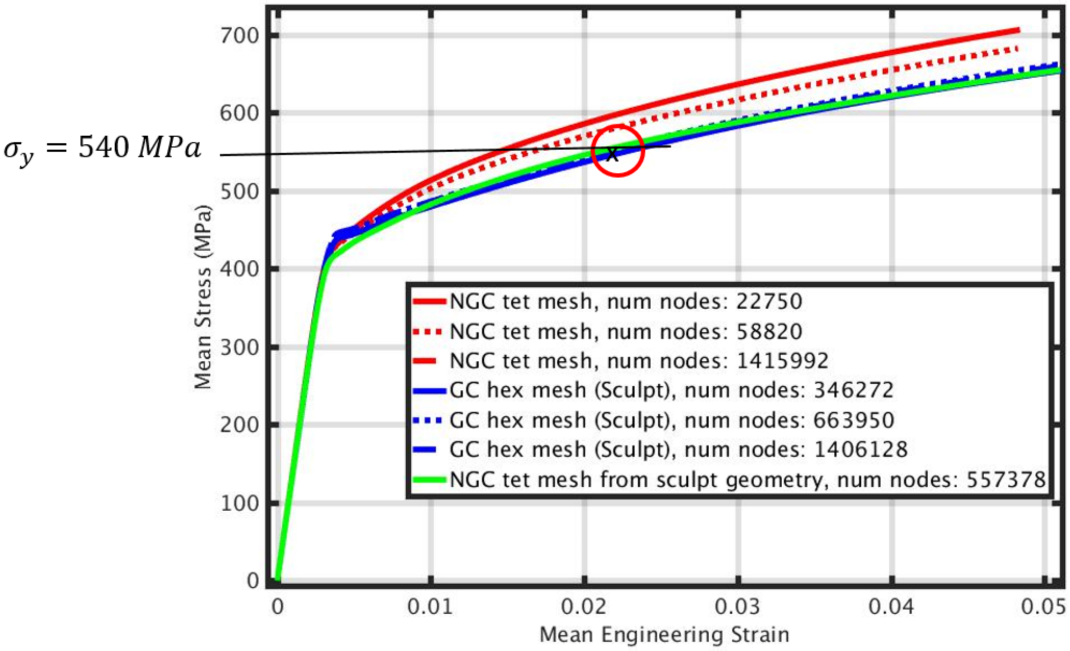

Figure 3.13: Comparison of statistics resulting from different meshing schemes

Figure 3.14 shows an enlarged view of the transition region between elastic and plastic behavior. Here there is evidence that treatment of grain boundary plays a role, with the transition apparently sensitive to the meshing choice. The grain-conforming mesh exhibits a much sharper transition between elastic and plastic behavior, while the non-grain-conforming meshes show a more gradual transition. It is hypothesized that this is due to the larger variation in local element-level strain conditions in the non-grain-conforming mesh resulting in a wider range of global strains that result in individual element transition to plasticity. It is also observed that the elastic-plastic transition is more senstive to mesh refinement for the grain-conforming mesh than the other schemes. Finally, this behavior may be particularly dependent on the texture as it closely related to the onset of plasticity in the grains. Further study of the meshes resulting from Sculpt seems necessary to understand all possible implications to the behavior observed.

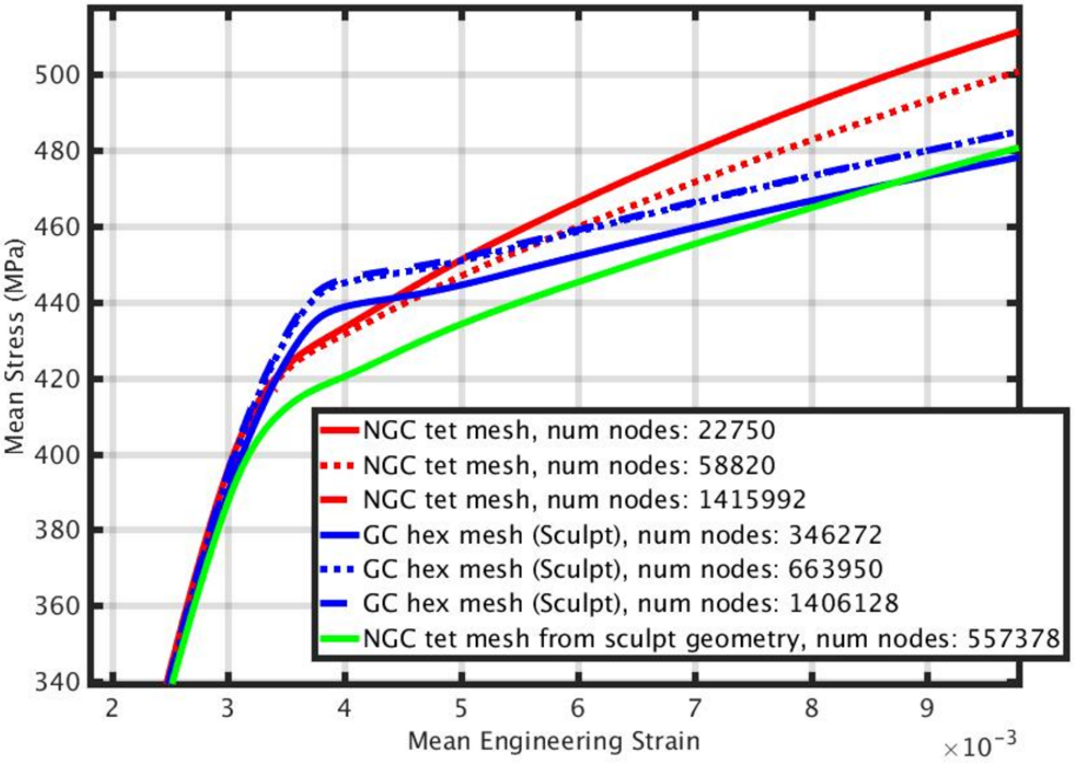

Figure 3.14: Comparison of meshing approaches at the start of plastic deformation

3.3 Chapter summary

In this chapter on microstructural modeling of AA 6061-T6, we presented a translation model for grain orientation and described a reduced-order form for that model. It was shown that when the translation model is calibrated to EBSD data, it accurately reproduces samples of texture and microtexture of that data. Subsequently, we described our method for developing finite element geometry and mesh models for microstructures and proved that for our purposes, we can use an overlay microstructure for computing crack nucleating load in an iron-bearing second-phase particle.

Chapter 4

Multiscale simulation

In this Chapter we outline the techniques we used to couple our engineering scale model with the microstructural models so that we may identify certain behavior within the mesoscale model that indicates the crack nucleation and incipient failure. Philosophically, we believe that homogenization techniques or hierarchical multiscale techniques are insufficient for a high-fidelity representation of the requisite physical processes, especially when ultra-high reliability requirements exist. The objective of concurrently coupling the models that represent physical phenomena occurring on differing length scales is to add physical fidelity where necessary, but not everywhere. This is a necessity given the complexity and computational expense of the fine-scale models. Moreover, for the complex, highly nonlinear behavior associated with ductile failure, it is insufficient to merely track deformation on the engineering scale and push boundary conditions downward with no feedback reminding the engineering scale of the particulars of deformation on the fine scale. This latter comment is tested within this Chapter.

We do not develop a new multiscale numerical method (MNM). To connect the length scales – reiterating that we were not focused on the development of a new MNM – we employ a rather unsophisitcated domain decomposition method with multipoint constraints (MPC) to achieve continuum-to-continuum coupling of our engineering-scale domain with a polycrystalline, meso-scale domain. Further, we make comparison between the MPC approach and a traditional sub-modeling approach, which achieves only one-way coupling. Submodeling is one-way coupling from the engineering scale solution to the mesoscale model. MPC coupling is the direct embedding and concurrent solution of the engineering and mesoscale models via Multi-Point Constraints (MPCs).

In the following, first we discuss our implementation of the submodeling approach using the existing capability in Sierra/SM [33]. Then we discuss the MPC approach for concurrent coupling of the differing length scales. Finally, we look at fields in a particle when coupled in both manners and attempt to iron out the necessity of concurrent coupling.

4.1 Submodeling

The submodeling capability that exists in Sierra/SM is used to couple our engineering length scale model with the microstructural models including second-phase particles. The procedure for submodeling is as follows:

1. solve the engineering scale model (with no knowledge of the mesoscale model);
2. given the prescribed position of the mesoscale model, map the displacements from the engineering scale model onto the outside surfaces of the mesoscale model; and
3. apply the mapped displacements as Dirichlet boundary conditions on the mesoscale model and solve for its response.

Figure 4.1 provides a visual flow chart for the procedure. Conveniently, this algorithm is performed automatically with Sierra/SM with the use of the Submodel block (refer to Section 7.14.11 [33]). In general, the input file contains details about both FE models with a list of "embedded" and "enclosing" blocks to signal when and where to perform the coupling. This approach only propagates information from the engineering scale to the mesoscale, there is no assurance that the resulting boundary conditions and mesoscale behavior are compatible with the behavior exhibited by the engineering scale model. This capability has been used for analysis of parts ranging in geometric length scale, *e.g.* parts containing small fasteners or welds, but to our knowledge it has not employed to couple distinctly different physical phenomena.

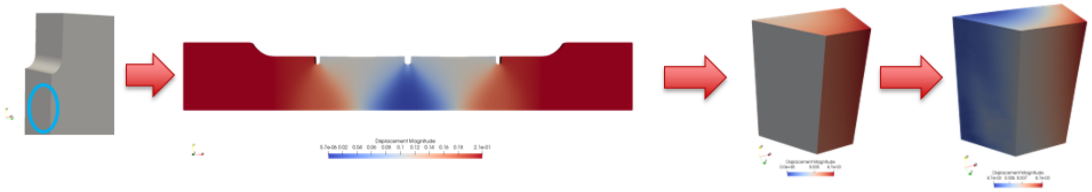

Figure 4.1: Depiction of submodeling process: engineering scale solution, mapping displacements to mesoscale model, solving mesoscale model

4.2 MPC coupling

The MPC coupling approach is a brute force method to couple the length scales [11, ?]. There are more eloquent methods coming online to perform this scale coupling [34, 35], but frankly, they are not mature enough for the present purposes. Moreover, it remains to be seen if they are beneficial for the current application given convergence issues and that they still require domain decomposition and special attention to meshing. Referring to notation from Section 1.1, the procedure is as follows:

1. identify the location to employ multiscale modeling, region $\mathcal{D}_k$, using the engineering scale calculation;
2. decompose the engineering scale geometry so that its domain is $(\mathcal{D} \setminus \mathcal{D}_k = S$ and mesh;
3. prepare the microstructural FE model to fit the domain in region $\mathcal{D}_k$;
4. prepare node and surface sets on both FE models;
5. make appropriate modifications to the analysis input file to add constrains coupling the displacements on the mating surfaces; and
6. solve the full problem to compute displacements in both domains simultaneously.

Figures 4.2 and 4.3 illustrate the procedure.

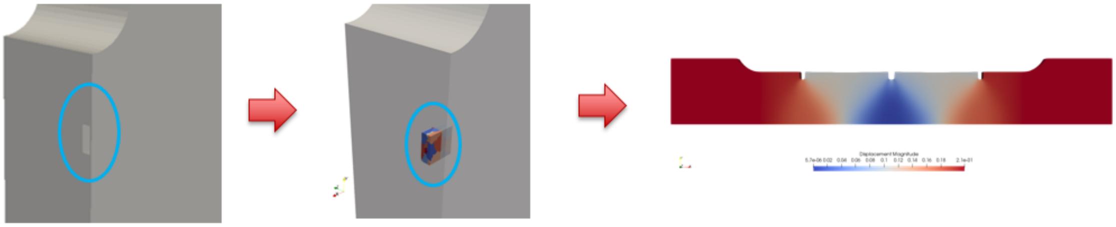

Figure 4.2: Depiction of submodeling process: engineering scale solution, mapping displacements to mesoscale model, solving mesoscale model

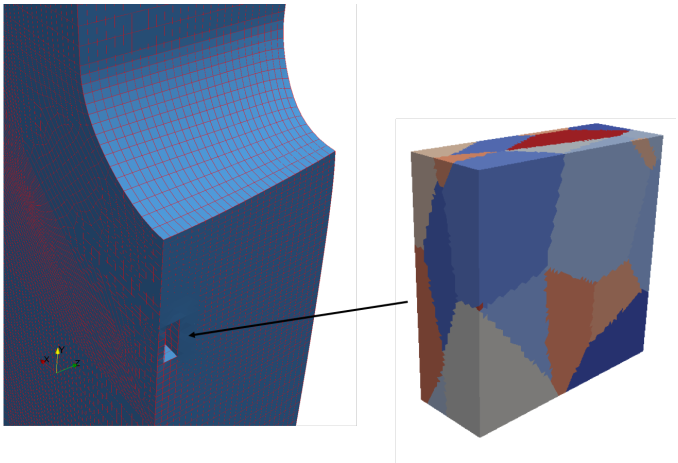

Figure 4.3: Engineering scale model is decomposed to contain region $(\mathcal{D} \setminus \mathcal{D}_k = S$ (left) so that the microstructural model (right) has a tight fit.

In the present implementation, the engineering scale model is constructed so that a set of elements exactly aligned with the mesoscale model. This facilitates the meshing because the elements are easily removed from the engineering scale model so that the mesoscale model could be embedded within it with no overlap (and no gap) between the models. The engineering scale meshing is evident in Figure 4.3 and can be seen to be quite coarse. We did not probe the sensitivity to the discretization, and we expect it to affect the results and it is a topic for furutre investigation.

4.3 Comparing the approaches

Engineering scale constitutive models are making dramatic improvements and with internal state variables and micromechanics, they can represent an awe-inspiring amount of fine-scale physics [36, 7]. One of the suppositions of this work is that concurrent coupling is necessary to accurately predict localization events. The question arises, do high fidelity engineering scale constitutive models obviate the necessity for concurrent coupling. Further, perhaps with an engineering scale model that accurately captions deformation and the onset of localization, perhaps a one-way coupling like our submodeling approach is sufficient. We use our multiscale approaches to explore this.

To ensure the best comparison between both approaches, the same engineering scale mesh (excepting elements removed to accommodate the mesoscale model) is used for both the submodeling and MPC coupling. The efforts in this report are admittedly light on mesh convergence investigation because of the rather cumbersome task of remeshing and assembling the multiscale calculations, a shortcoming that should be addressed with future work. Per our hierarchical approach, the location to embed the subdomain is chosen based on the engineer-scale solution. Discussed in Section 6.4, for ductile fracture we can use points of high-triaxiality to base the decision.

Our microstructural model is the same as presented in SubSection 3.2.4. We assume that the second phase particle in the mesoscale model, the ellipsoid, is elastic and brittle. The engineering scale model uses Hill anisotropic plasticity calibrated to the available tension data. The calibration and engineering scale model are is discussed in depth in Chapter 6. Figure 4.4 plots the deformed shape of the polycrystal and particle for both multiscale modeling approaches overlapped. There are small differences, but the deformations are distinctly different, which strengthens the notion that submodeling even with a high fidelity engineering constitutive model is not the same as concurrent multiscale.

Figure 4.5 plots the maximum first-principle stress in the particle versus simulation time for one sample of a macro- and micro-textured polycrystal run using MPC and submodeling. The first observation is that the stress in the particle is very high, probably due to the constraint caused by the coupling schemes, *i.e.* opposed to the simple boundary conditions applied in SubSection 3.2.4. The use of the elasto-plastic model for the particle was not possible at the time of this writing. In subsequent discussion we monitor the mean first-principle stress in the particle. The next observation is that at higher stress levels, the choice of texture model deviates widely for the MPC calculations, but more narrowly for submodeling. This seems to indicate the necessity for concurrent coupling. The figure inset shows contour plots of von Mises stress on a macro-textured polycrystal, cross-sectioned

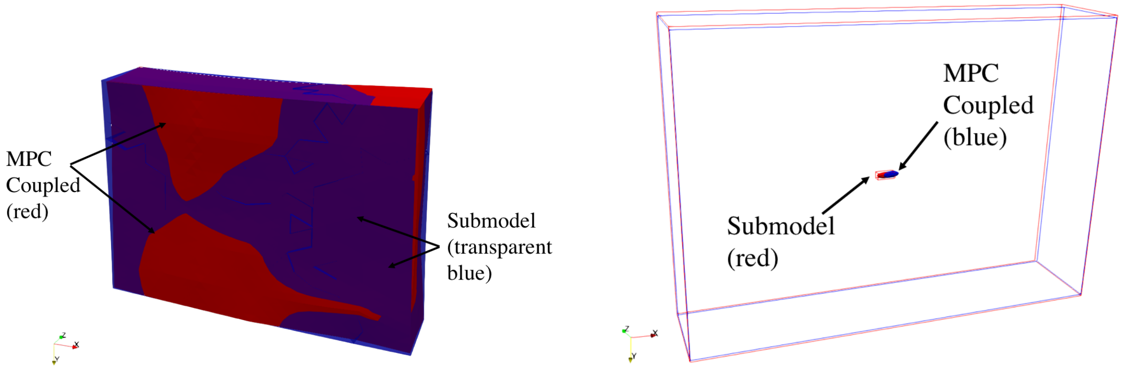

(a) Matrix (b) Particle

Figure 4.4: Comparison of the multiscale modeling approaches showing the deformation of the polycrystal (a) and particle (b).

through the particle. There are noticeable differences on the low end of the stress band, but the particle stresses look similar. The deformed shapes (included) have noticeable differences.

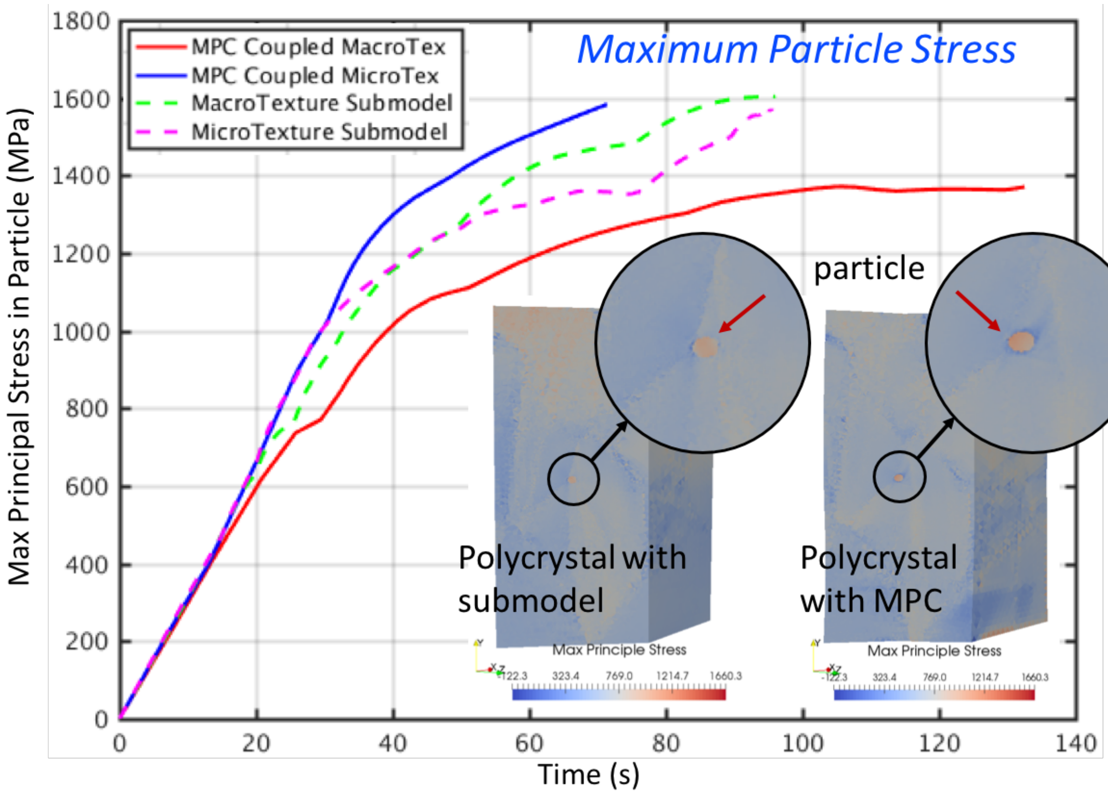

Figure 4.5: Maximum first-principle stress in the particle for MPC macro texture (red), MPC microtexture (blue), submodel macro texture (green) and submodel micro texture (pink).

In Figure 4.6 the mean first-principle stress is plotted versus nominal applied engineering strain on the engineering specime, computed as the displacements at the ends of the engineering scale domain normalized by it's original length. The solid lines represent the mean value of the stress-strain curve while the dashed lines are plus and minus one standard deviation. For this comparison ten Monte Carlo samples were used. The inflection points that are visible in the submodeling result correspond to the points at which the engineering scale displacement was recorded. The displacement applied to the exterior of the mesoscale model between these points was a linear interpolation between nearby records. A close inspection of Figure 4.6 shows that at the critical value of 540 MPa the mean values are similar but the distributions only overlap by a small fraction of their area.

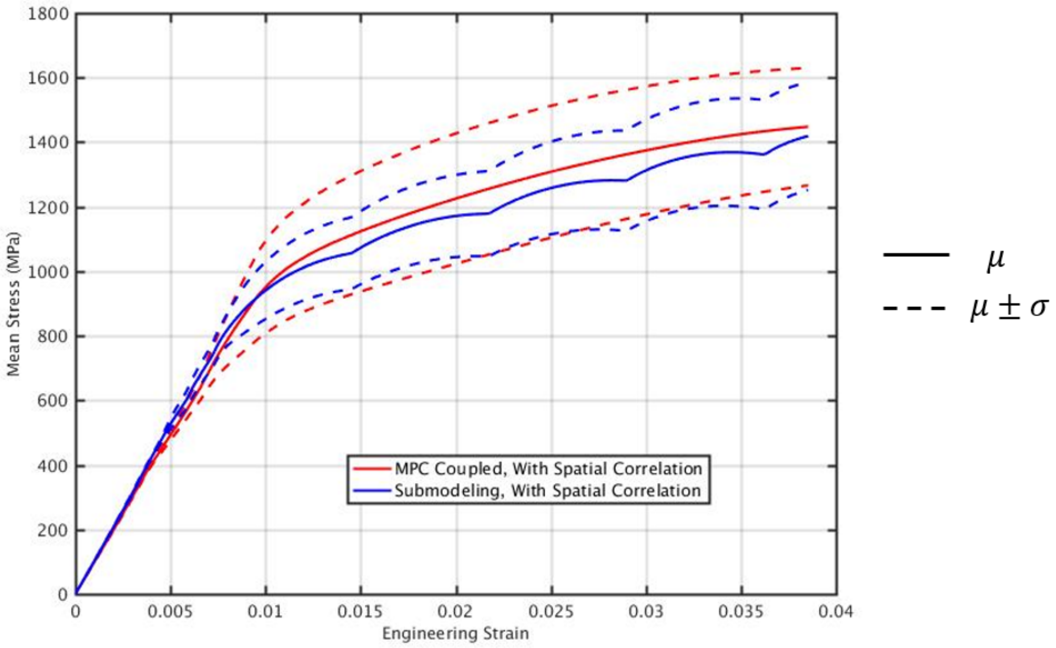

Figure 4.6: Comparison of statistics resulting from different coupling schemes run for many realizations of microtexture. The data plotted are mean and +/- standard deviation for the MPC (red) and submodeling approachs (blue).

4.4 Chapter summary

In this chapter we discuss two methods to couple a microstructure with an engineering scale structure. With submodeling, information flow is one-way down length scales from the engineering scale model to the microstructure in the form of kinematic boundary conditions. This implies that if the localization process in the microstructure influences the behavior of the engineering scale model, the effects are lost due to the one-way flow of information. It should be noted, our microstructural models do not soften, so this one-way coupling may be sufficient. Nevertheless, we compared the submodeling approach to an approach for brute force concurrent coupling. In this, we couple the two length scales via multi-point constraints on matching surfaces of the two domains. When the state of microstructural modeling is sufficiently mature as to nucleate cracks and propagate them through the microstructure, thereby simulating the localization of strain and attendant load shedding, this concurrency will be necessary.

Chapter 5

Multiscale digital image correlation

To support model development and validation, a multiscale, full-field experimental technique based on digital image correlation (DIC) was explored. Because the DIC technique lacks an inherent length scale, it can be used at a wide range of scales – from atomic force microscopy to entire rocket assemblies. A multiscale DIC approach is an ideal solution to validating hierarchical models since it will provide macroscale deformation measurements of the entire component while simultaneously providing details of hotspots with microscale resolution. Only a few researchers have attempted to use multiscale speckle patterns for DIC. For a large region of interest encompassing several meters, Reu [37] painted through two templates with different colors (black and grey) to generate overlapping speckle patterns with considerably different speckle sizes (20 mm and 2 mm). Other researchers have performed multiscale DIC at smaller scales [38, 39], but with limited range of scales because a single speckle pattern was used at different fields of view.

One goal of this project was to develop multiscale DIC techniques and to use the multiscale results to inform multiscale models. Although multiscale approaches had been investigated previously [40, 38, 37], none of the prior work attempted it at the high magnifications and large scale separation of interest in this work. The approach was to use a low magnification scale to capture the strain field throughout an entire "structure" such as the 6-notch specimen as illustrated in Figure 5.1.

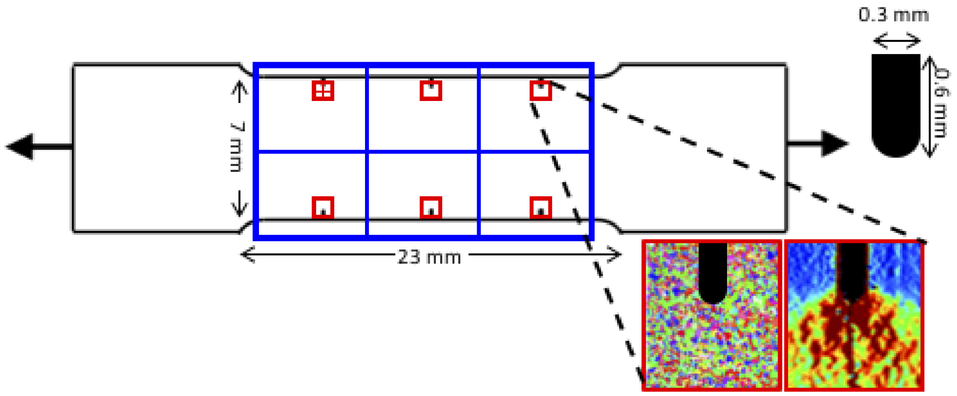

Figure 5.1: Multiscale DIC uses low magnification images to cover the entire specimen, and high magnification images to capture deformation details at stress concentrators.

Multiscale DIC techniques were developed and applied to several notched specimens loaded while being observed in situ in an SEM. In one case, the full surface microtexture was obtained through EBSD, *e.g.*, Figure 5.2. These EBSD measurements were used to plot the inverse pole figures in Figure 2.3, although they were independently confirmed with other EBSD scans.

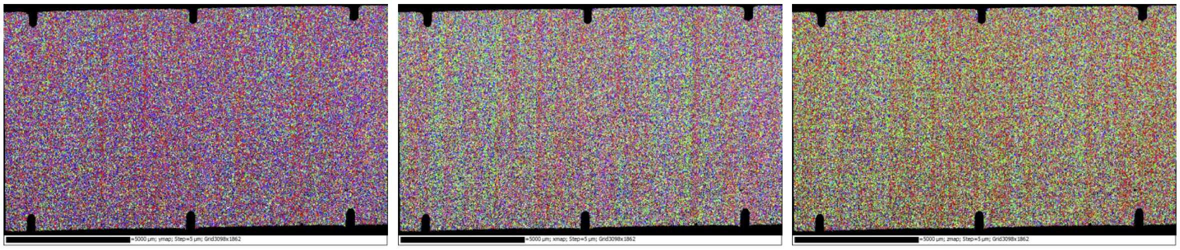

(a) (b) (c)

Figure 5.2: Grain orientations in a 6-notch specimen relative to the (a) transverse direction (b) rolling direction, and (c) normal direction.

At first glance, these six notches appear equally likely to initiate specimen failure. However, finite element modeling indicated that diagonal strain bands, which link the notches, create a bias toward crack nucleation and fracture occurring in the the center notches. These model results are shown and confirmed by experimental observation in Figure 5.3.

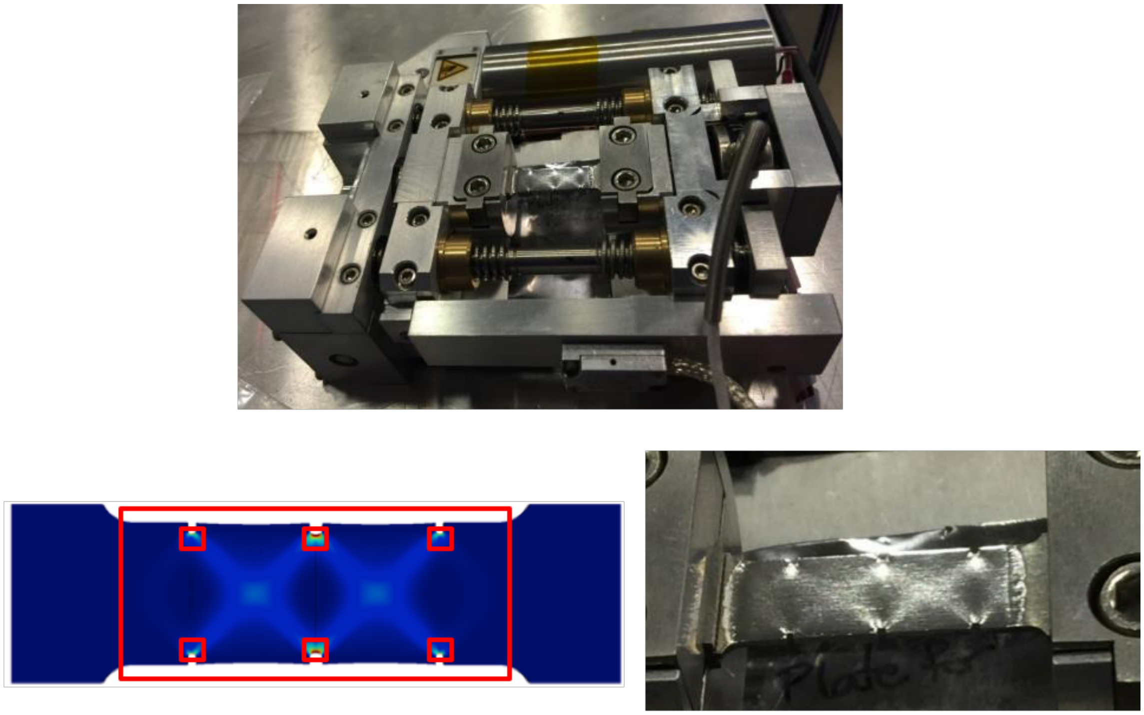

Figure 5.3: Failure in this specimen geometry is most likely at the center notches due to two diagonal shear bands whereas the distal notches only have one.

For multiscale DIC in the SEM, it was necessary to capture a fairly large montage of images to cover the entire specimen for low magnification DIC. At high magnification DIC, montages were again used to observe strain localizations at notch tips with sub-grain resolution. Examples of such images are shown in Figure 5.4.

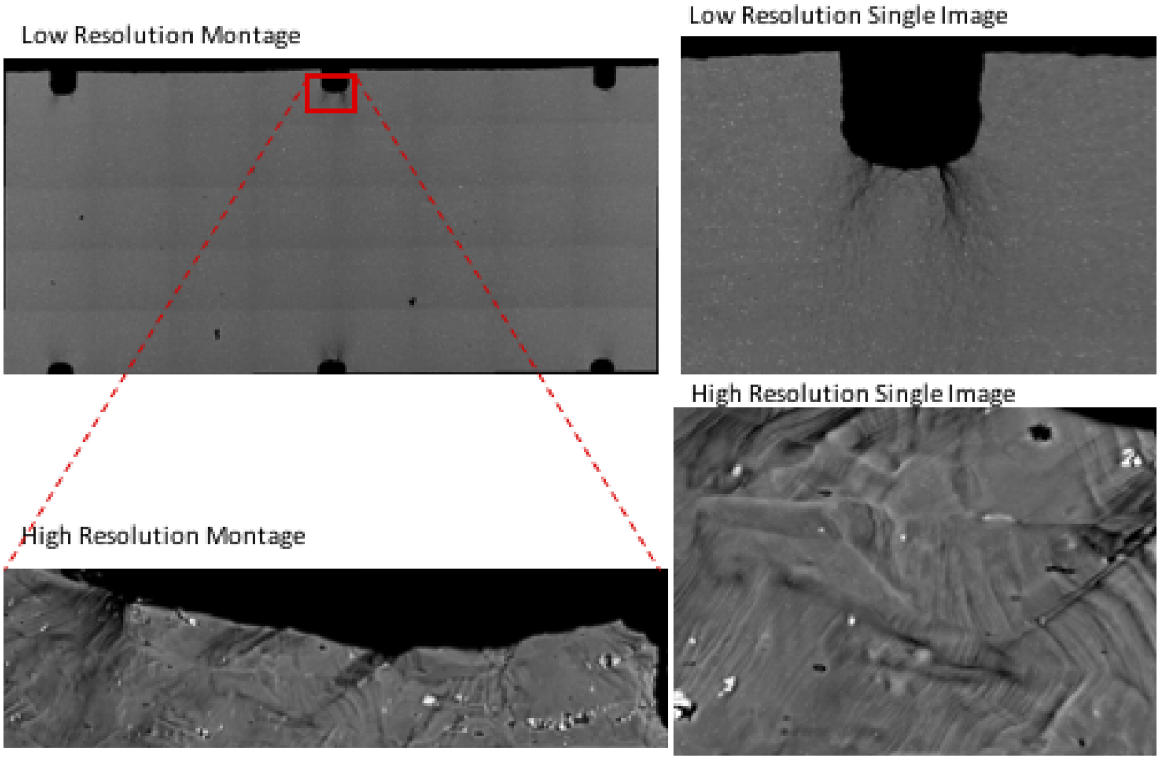

Figure 5.4: Low magnification montages were used to image the entire specimen. High resolution montages were used to image notch tips with sub-grain level details.

Making use of the multiscale imaging requires multiscale speckle patterns. Many techniques were attempted for applying such patterns to specimens. One significant challenge was getting a suitable small-scale speckle pattern. Many techniques were tried including 1. Inherent patterns, 2. Copper nanospeckle powder, 3. Self-assembled nanoparticles, 4. Electroplating island deposition, and 5. Thin film remodeling. These will be discussed in order. First, it was thought that the precipitates and inclusions shown in Figure 2.1 could be used. Unfortunately, upon significant loading, the contrast of these speckles decreased markedly, thereby rendering them nearly invisible at higher strains. This is demonstrated in Figure 5.4 by the fact that so few of the inclusions and precipitates can be seen in the images. Second, copper nanospeckle power was used following [38]. This technique is relatively easy and effective, but true SEM-DIC images for the goals of this study are near the particle size and spacing limit of the technique: it is challenging to make speckles small enough with this technique. Third, a visit was made to the University of California Santa Barbara (UCSB) to meet the leading researchers in this field and to learn some of their speckling techniques. The self-assembled nanoparticles approach by Kammers *et al.* [39] was learned and applied for Sandia specimens. Fourthly, electroplating deposition was attempted in which coatings were electrodeposited on top of specimens with settings chosen such that they would form islands rather than a solid coating. This technique showed great promise for one specimen, but did not appear to be easily repeated. Finally, a thin film remodeling technique was used in which specimens were sputtered with a thin layer of gold and subsequently subjected to humidity to shrink the gold into islands suitable for high magnification DIC. Many iterations of settings were attempted for this technique and at this point it appears to be the most promising for the applications of this project. Some of the resulting speckle patterns from this technique are shown in Figure 5.5 along with the settings chosen to make these patterns in Table 5.1.

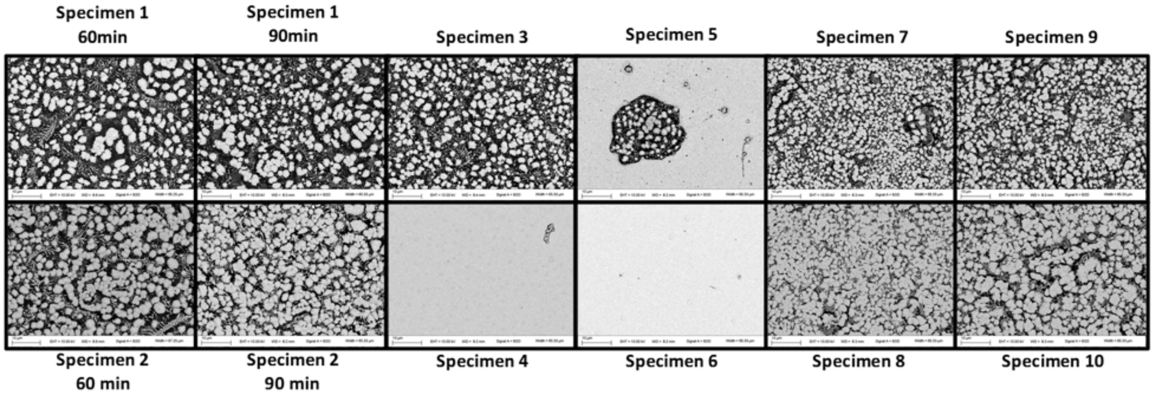

Figure 5.5: Speckle patterns created by several different settings (see Table 5.1) with coating thicknesses of 50 nm (top) and 80 nm (bottom). Images are consistently 64 μm wide, captured using backscatter electron imaging.

Specimen	Au thickness (nm)	Set Temp (C)	Duration (min)	Chamber Vol. (cm^3)	Vapor Flow (mL/hr)	Flow Area (mm^2)	Insulated (Y/N)
1	49.4	342(280)	60	1158	80	256	N
2	78.6	342(280)	60	1158	80	256	N
1-repeat	49.4	342(280)	30	1158	80	256	N
2-repeat	78.6	342(280)	30	1158	80	256	N
3	49.4	342(280)	60	1158	60	96	N
4	78.6	342(280)	60	1158	60	96	N
5	49.4	342(280)	60	1158	70	256	Y
6	78.6	342(280)	60	1158	70	256	Y
7	49.4	342(280)	60	2835	100	478	N
8	78.6	342(280)	60	2835	100	478	N
9	49.4	342(280)	60	2835	100	179	N
10	78.6	342(280)	60	2835	100	179	N

Table 5.1: Settings used for each sputter.

Performing DIC on SEM images creates special challenges. In particular, SEM images have much more distortion than conventional images due to the fact that SEM images are captured using a rastering technique. Early attempts at DIC in the SEM were unsuccessful due to these SEM distortions. One example of this is the horizontal strain field from a montage of images shown in Figure 5.6. The general strain field is captured in this image, but it is interrupted by purple bands of distorted results because the left edge of each of these images was distorted. Correction techniques for SEM distortions have been developed by Kammers and Daly [1]. These techniques allow images to be corrected to remove the distortions associated with SEM images. To correct for distortion, images are captured of a speckled, unloaded specimen at various locations. By extracting and analyzing the strain fields of these rigid motions (the true strain field is zero everywhere), the distortions due to SEM imaging can be quantified spatially. Figure 5.7 shows a schematic of the technique from [1] in the upper left inset. The rest of the figure shows the e_{xx} strain field calculated for these rigid motion images thereby demonstrating the spatial distortion. This distortion can then be corrected in functional DIC images.

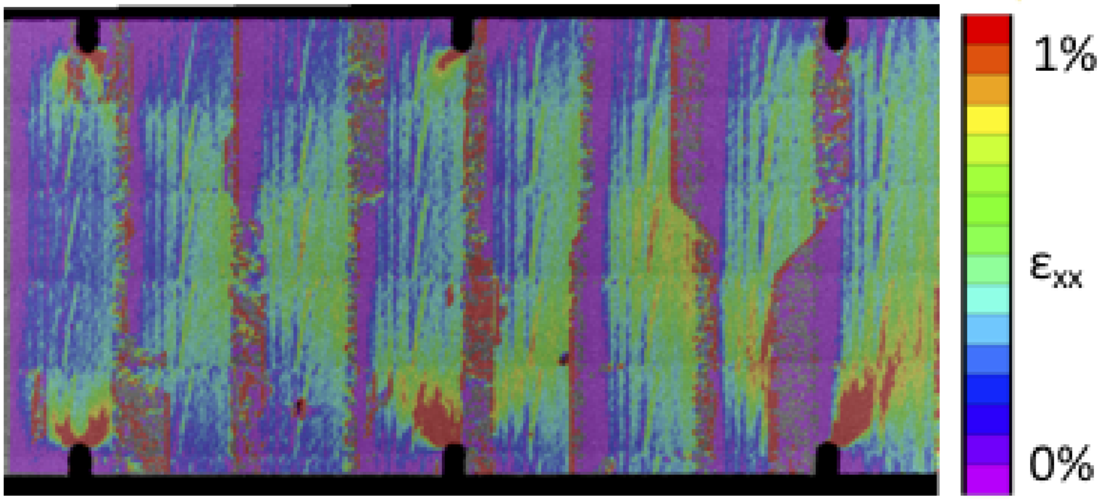

Figure 5.6: Challenges with montaging DIC data with SEM distortions.

High magnification DIC measurements were made on notch tips in a few specimens with limited success due to time constraints. Unfortunately, simultaneous multiscale DIC was not achieved. However, the majority of the techniques and capabilities necessary to achieved this was developed in this LDRD. One example of a notch tip strain field is shown for a similar specimen in Figure 5.8 using copper powder. These strain fields show the two strain bands emanating from the tips with strain localizations around the grain scale. Yet another, higher magnification strain field around a crack tip is shown in Figure 5.9.

Another approach to multiscale in the SEM is to use the multiSEM – a 61 beam SEM capable of incredibly fast imaging rates. As a trial, the multiSEM was used to image precipitates and inclusions in the aluminum as a trial for high resolution DIC over large areas. One example of MultiSEM imaging is shown in Figure 5.10 in which two 2.5 x 2.5 mm regions were imaged with 4 nm resolution in one hour. This tool has great promise, but the extremely fine speckle patterns required to take advantage of it are not currently capable of being produced.

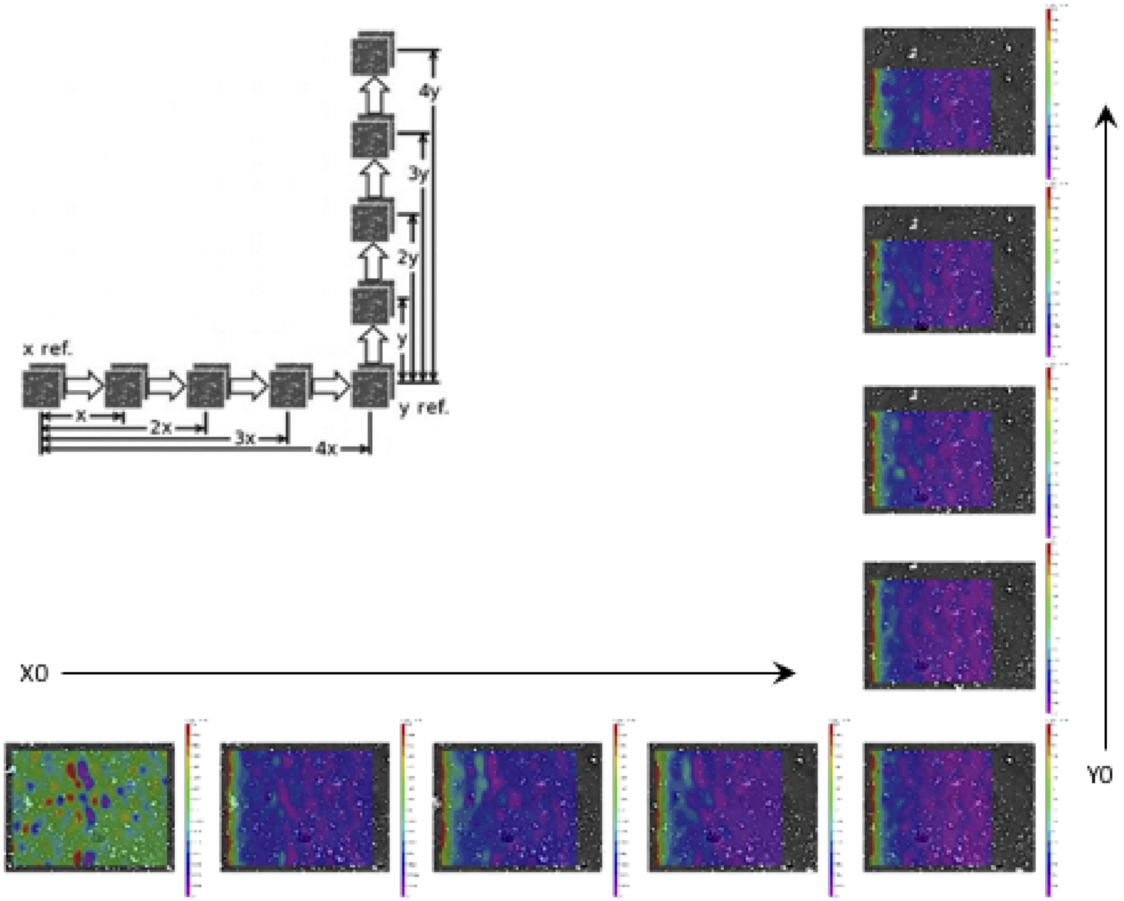

Figure 5.7: SEM-DIC distortion correction technique taken from [1]. In this case, four steps are taken in the X and Y directions covering a total distance of one quarter of the field of view in each direction.

As shown earlier, notched specimens exhibit significant differences in ductility with the primary drivers being geometrical tolerances and microstructure. DIC measurements such as the ones shown here are valuable for validating models to predict failure distributions. These measurements can be made even more powerful if combined with HR-EBSD measurements such as those supplied by Professor Kacher at Georgia Tech for this project, described in Chapter 7. DIC can give surface strain measurements of hotspots in situ. This data can be bolstered by HR-EBSD measurements, which can destructively provide strain measurements internally as well as information on GNDs in the same region as the high resolution DIC to add yet more understanding to the failure mechanisms in FCC metals.

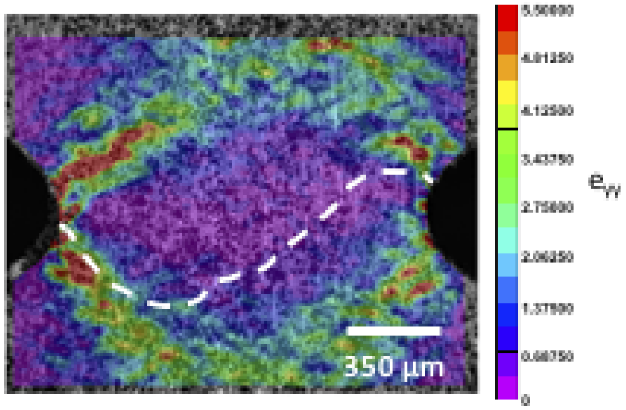

Figure 5.8: DIC strain measurement at notch tips just before specimen fracture achieved with copper powder speckling. The eventual fracture path is shown by the dashed line.

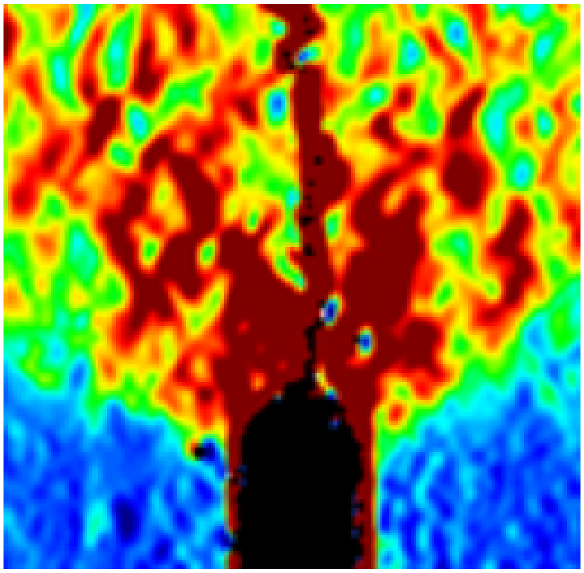

Figure 5.9: Grain level DIC strain accumulation at a notch tip.

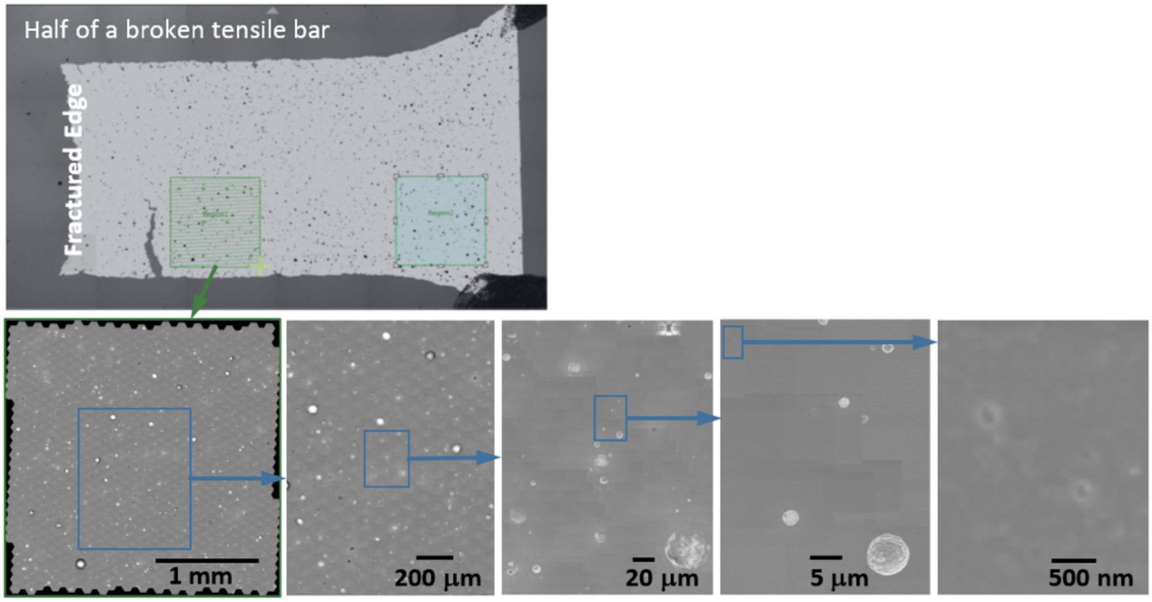

Figure 5.10: MultiSEM imaging of large areas.

Chapter 6

Numerical examples

We present 4 examples to demonstrate the tools. In the first example, we use the microstructure modeling tools for treatment of a small scale plate whose dimensions only allow for a small number of grains. It is idealized to be cubic elastic and pure aluminum, but having the same texture as measure for our AA 6061-T6. The takeaway message is the efficiency and accuracy of the random field reduced-order model. In the second example, we construct yield surfaces for polycrystals modeled with macro- and micro-texture and demonstrate subtle, but we assert important, differences between the two texture models. In the third example, we add the second-phase particles and consider the load on the particle for simple applied loadings on the microstructure. In the final example, we explore the multiscale models and effects that including the full engineering scale boundary value problem has on the load in the particle.

6.1 Example 1 – cubic elasticity and micron-size plate in plane strain

This example is a hypothetical scenario with significantly reduced complexity. We formulate the problem so that we consider cubic elasticity in a small polycrystal. Constitutive data is taken from the literature. Multiscale coupling is avoided because the microstructure can tractably be modeled over the entire domain. The tractability of the problem enables us to generate our own “truth” data by performing a large number of direct numerical calculations of the microstructural model, thereby allowing us to evaluate the accuracy and efficiency of the random-field reduced-order model (RFROM).

6.1.1 Formulation

Consider a plate in plane strain with dimensions $240\mu m$ x $120\mu m$ x $0.5\mu m$. The plate is comprised of a cubic-elastic pure aluminum with elastic constants taken from [41]. The average grain size is approximately $40\mu m$, so that there are approzimately 18 grains in the specimen. Suppose that the plate has stringent design requirements for extension displacement when loaded longitudinally, so developing the probability law for apparent modulus of elasticity E_{app} can be used to quantify failure. We generate "truth" data by FE simulation, varying crystallographic orientation using the models in 3 and EBSD data presented in 2, with 400 instantiations of non-textured, macro-textured and micro-textured crystals. Figure 6.1 shows the assumed boundary conditions and Figure 6.2 is a contour plot of the xx-component of stress, showing the random distribution of load in the plate. The FE mesh uses selectively-reduced integration hex elements on a uniformly spaced grid with grid spacing equal to the plate thickness. This results in approximately 80 brick elements per grain edge, sufficiently resolving the fields [27].

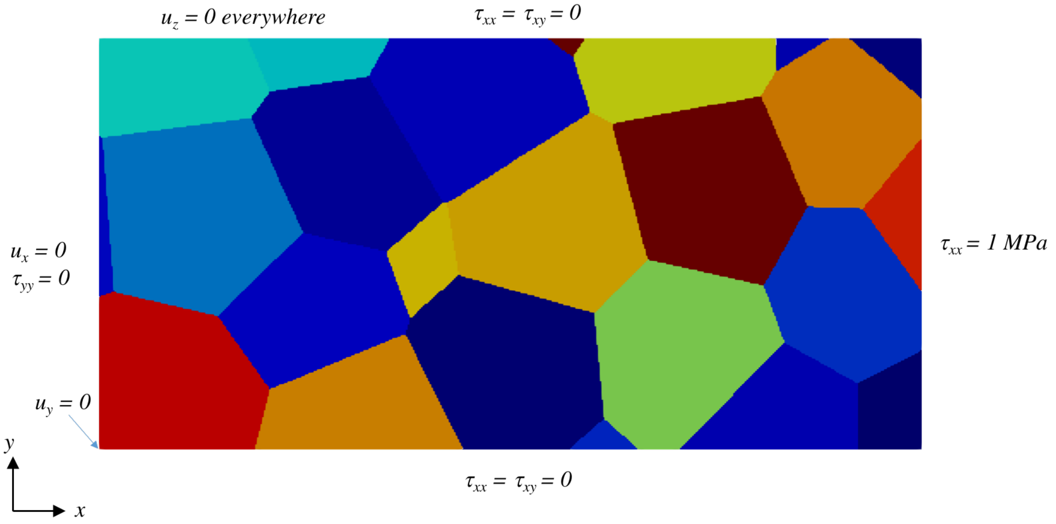

Figure 6.1: Boundary conditions for example 1.

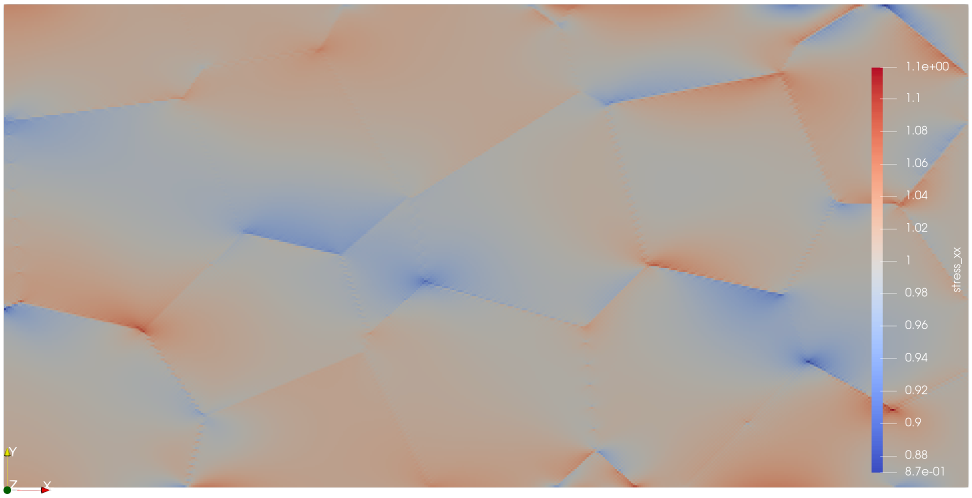

Figure 6.2: A sample σ_{xx} distribution for a micro-textured example 1.

We randomly draw 20 samples from each set of truth data to simulate load-displacement test data samples from which to estimate apparent modulus. The estimates of apparent modulus are then used to compute the maximum likelihood estimators (MLE) for a given set of probability distributions, and the best fit is chosen based on the minimum of the negative log-likelihood. This model serves as the engineering-scale model for this illustration. Note that in the context of a real engineering problem, twenty samples of test data is on the high end of reality. Very often, there are fewer samples available. Table 6.1 summarizes the estimates of negative log-likelihood for the 20 samples and for the full set of 400 calculations. In all cases, the beta distribution is chosen. Table 6.2 tabulates the parameters for beta as determinted from the MLE for both the 20 samples. The engineering scale performance estimate is generated with 100 Monte Carlo samples drawn from these beta distributions, which is done to simulate reality when an engineering scale model is less expensive than the microstructural model but not free.

	no texture		macro texture		micro texture	
beta	3162.6	154.3	3190.3	161.0	3239.4	157.0
pareto	3506.0	168.3	3454.4	173.6	3526.7	166.6
norm	3163.2	163.5	3190.6	165.6	3240.3	162.6
gamma	3164.2	163.4	3190.5	165.8	3241.2	162.4
rayleigh	3278.6	inf	inf	inf	inf	162.4

Table 6.1: Maximum likelihood estimates.

	a	b	location	scale
no texture	1.327	0.7743	67079	3657.9
macro	2.566	0.9038	65839	5037.5
micro	0.8275	0.9716	67694	3262.8

Table 6.2: MLE parameters for beta for apparent modulus from 20 samples.

The fine scale performance estimate is achieved with recoarse to a RFROM as described in Chapter 3. The direct numerical calculation is conducted for a realization corresponding to each of 50 RFROM samples. The

6.1.2 Results

Figure 6.3 plots the cumulative distribution of apparent modulus computed with the sets of 400 simulation results, the so-called “truth” data. There are subtle differences in the distributions between no-, macro-, and micro-texture. It appears that correlation in the micro-textured microstructures lends to polycrystals that are both stiffer and more compliant, so that the tails of the distribution extend further on both ends. On the other end of the spectrum, the non-textured results suggest a lower variance, which suits intuition suggesting these grains are optimally disorganized. As expected, the macro-textured results tend to split the difference.

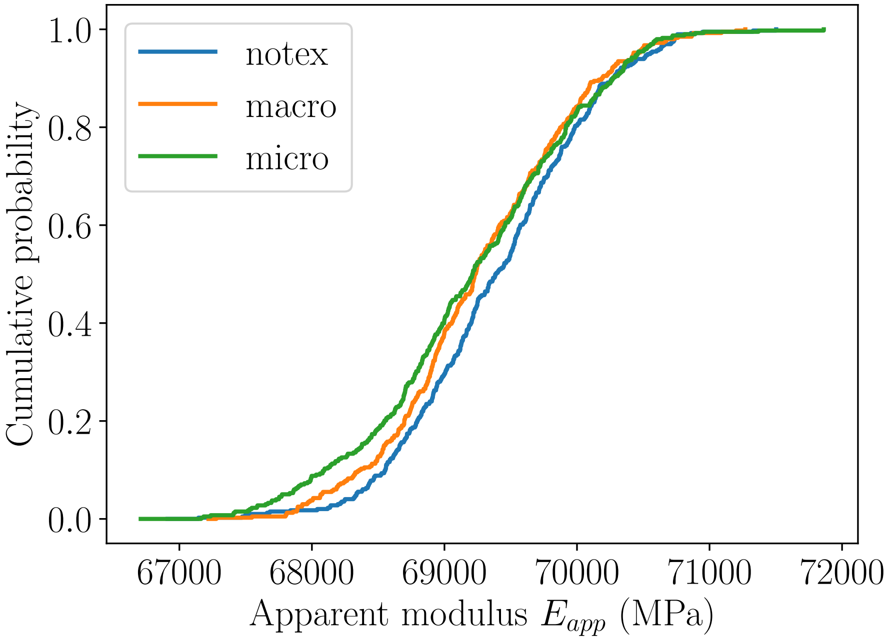

Figure 6.3: Estimated "truth" cumulative distribution for apparent modulus of a plane strain, micro-size plate with non-, macro-, and micro-textured cubic crystals.

Figures 6.4–6.6 plot the cumulative probability for the apparent modulus. Each plot includes the cdf computed three ways: by the MLE-estimated beta distribution of the engineering-scale model; by the RFROM of the microstructural-scale model; and by the truth estimate from the direct numerical calculations. A common measure for comparing probability distributions to a reference is the Kolmogorov-Smirnov (K-S) two-sample test [42, Section 10.1]. However, this approach requires the samples of both random variables to be independent and identically distributed (iid), and the SROM samples violate this requirement. Nevertheless, we compute the maximum difference norm and tabulate in Table 6.3. We further develop an alternative measure for the comparison. Let $F(x)$ denote the empirical cdf obtained from the "truth" sample data. Let $F_1(x)$ denote the empirical cdf obtained from the engineering-scale sample data. Let $\tilde{F}(x)$ denote the cdf of the SROMs. An appropriate error metric used here is the the L^2 norm of the difference between two CDFs, *i.e.*,

$$\begin{aligned} m_1 &= \int_{\mathbb{R}} \left(F_1(x) - F(x)\right)^2 \mathrm{d}x \\ \tilde{m} &= \int_{\mathbb{R}} \left(\tilde{F}(x) - F(x)\right)^2 \mathrm{d}x \end{aligned} \tag{6.1}$$

These errors are listed in Table 6.4 for the cases of no texture, macro texture, and micro texture. It is evident that, in every case, the SROM micro-scale model outperforms the engineering-scale model.

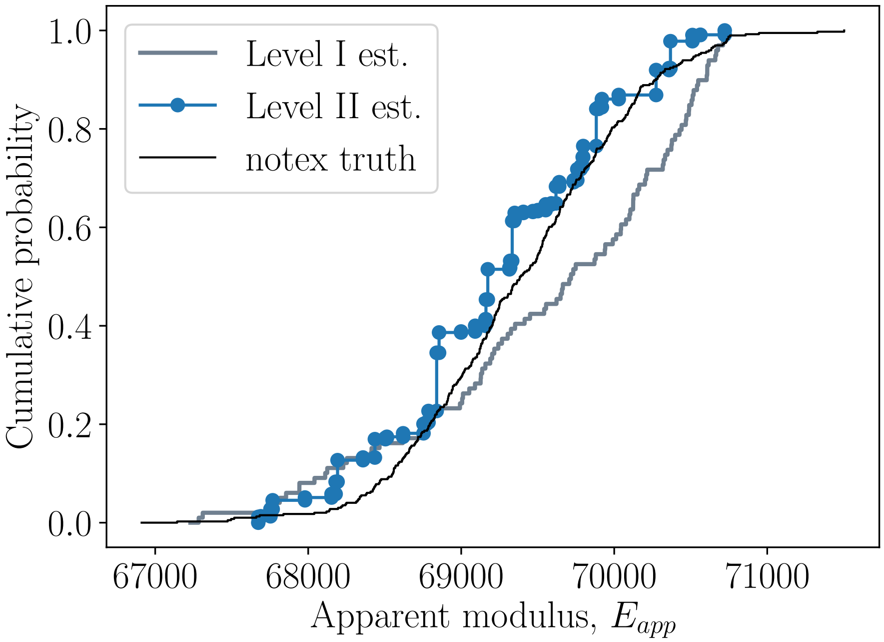

Figure 6.4: Cumulative probability estimates of apparent modulus for a non-textured microstructure.

	No texture	Macro texture	Micro texture
LI engineering scale	0.224	0.166	0.131
LII microstructure scale	0.154	0.197	0.196

Table 6.3: L_∞-norm comparing the CDFs of the models to the "truth" data.

6.1.3 Comments

The Level I engineering scale model is trivial in this example and we could have chosen many thousands of samples. However, more MCS samples does not correct for errors due to sparse data, *i.e.*, only 20 tests. There is a subtle point to be made here that supports higher-fidelity, and therefore multiscale, modeling. In real engineering examples, there is often limited data available to calibrate models. In some sense, this sparsity of data outweighs the accuracy of the engineering scale model. On the other hand, as with the present example, we often have a large amount of data to calibrate fine-scale models.

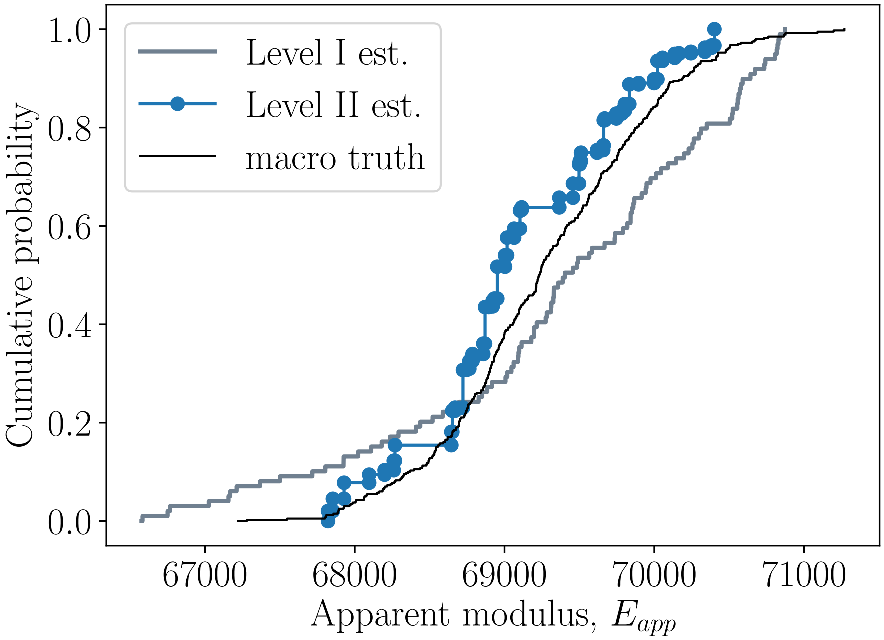

Figure 6.5: Cumulative probability estimates of apparent modulus for a macro-textured microstructure.

	No texture	Macro texture	Micro texture
LI engineering scale	41.02	40.7	23.3
LII microstructure scale	12.1	18.6	22.8

Table 6.4: L^2-norm comparing the CDFs of the models to the "truth" data.

6.2 Example 2 – microstructure texture models

6.2.1 Formulation

To study the effects on the homogenized response we have developed so-called voxellated, or overlay, geometries following the grain-independent mesh model scheme described in Chapter 3. The geometry and mesh models are constructed by overlaying a Poisson Voronoi tessellation onto a uniform hexahedra mesh of varying densities following closely [43, 27]. Figure 6.7 illustrates one morphological sample of overlayed geometry with macro-textured (left) and micro-textured (right) crystal orientations. Note that, the grain shapes are not equiaxed. Rather, the average dimensions in the "N" direction is smaller than the average "R" and "T" direction to simulate the measured average grain dimensions of the rolled plate. This was achieved by a linear mapping from the output of the Voronoi tessellation to

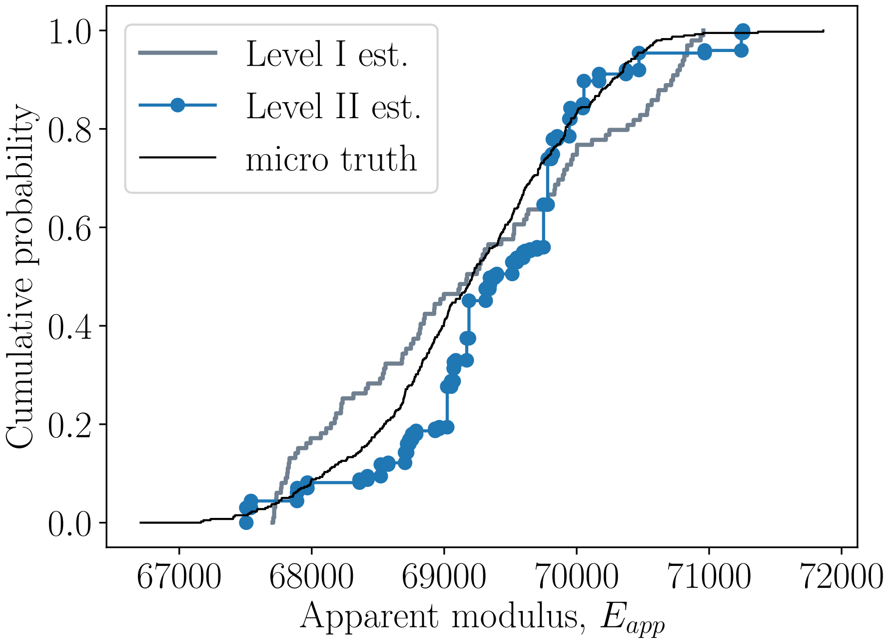

Figure 6.6: Cumulative probability estimates of apparent modulus for a micro-textured microstructure.

a "rolled" state. The colors plotted are the first Euler angle in each grain so that the grains are obvious.

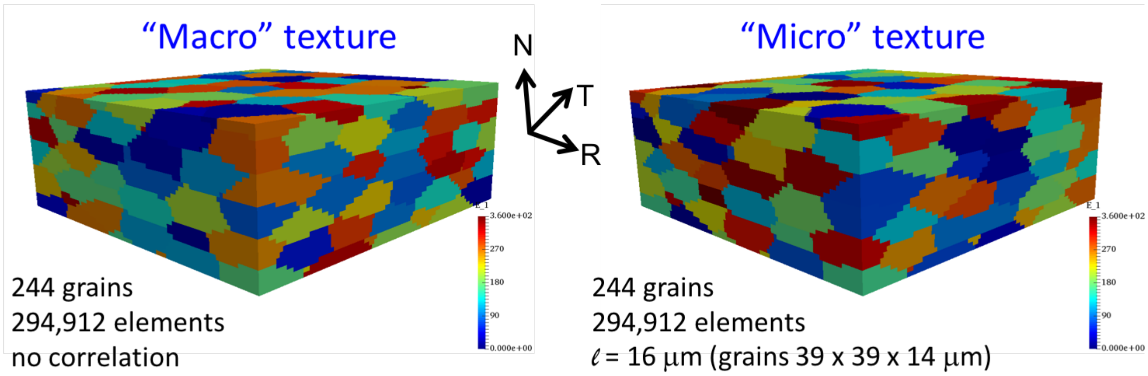

Figure 6.7: Two texture samples of an aluminum 6061-T6 rolled microstructure. The macro texture sample (left) does not include spatial correlation in the random-field model for crystallographic orientation whereas the micro texture sample (right) does.

With samples like these, we have simulated applied bi-axial loadings and extracted homogenized response following [27] and compared with a von Mises approximate of the yield surface. Our crystal plasticity model closely follows [10], and was calibrated to the average of smooth tensile data measured for our AA 6061-T6 and presented in Chapter 2. The fit and properties appear below in Figure 6.8. We use these properties throughout for the crystal plasticity simulations contained herein.

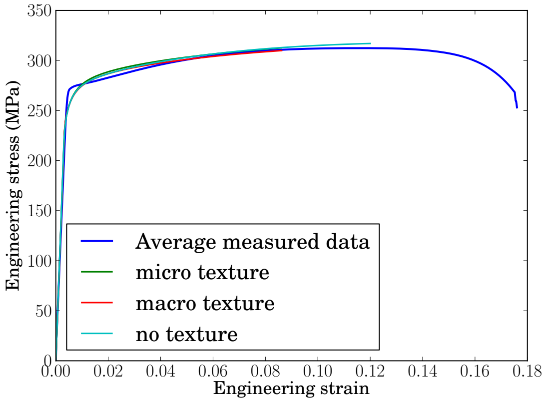

Figure 6.8: Crystal plasticity calibration to average smooth tensile data.

	no	macro	micro
g_0 (MPa)	110.6	115.2	114.0
g_{s0} (MPa)	169.4	174.7	172.8
G_0 (MPa)	116.6	116.6	116.6
m	0.01	0.01	0.01

Table 6.5: Crystal plasticity material parameters.

6.2.2 Results

The yield surfaces for three random samples of macro- and micro-texture are shown in Figure 6.9. The salient point is that when spatial correlation is maintained in the texture model, there are subtle differences and variations in the corresponding yield behavior. These differences can lead to significant differences in yield-surface normals compared with traditional J2-based engineering scale plasticity models, as illustrated by the overlap of the von Mises yield surface in the figure.

6.3 Example 3 – microstructure and second-phase particle

6.3.1 Formulation

Next, we further employ the grain-independent meshing algorithm to explore the impacts of texture on second-phase particles, idealizing the second-phase particle as an ellipsoid. Two examples of this type of microstructure are shown in Figure 6.10 where the roughened edges of the grain boundaries are obvious. Interestingly, by chance in both of these morphological realizations the particle is located on or intersecting the grain boundaries, an effect that bears deeper investigation. This microstructure is considerably smaller than would be recommended for applications predictions, but is tractable enough that we can perform some studies and compare with our reduced order model. In the end, there are 32 grains and 548,351 composite tetrahedral elements.

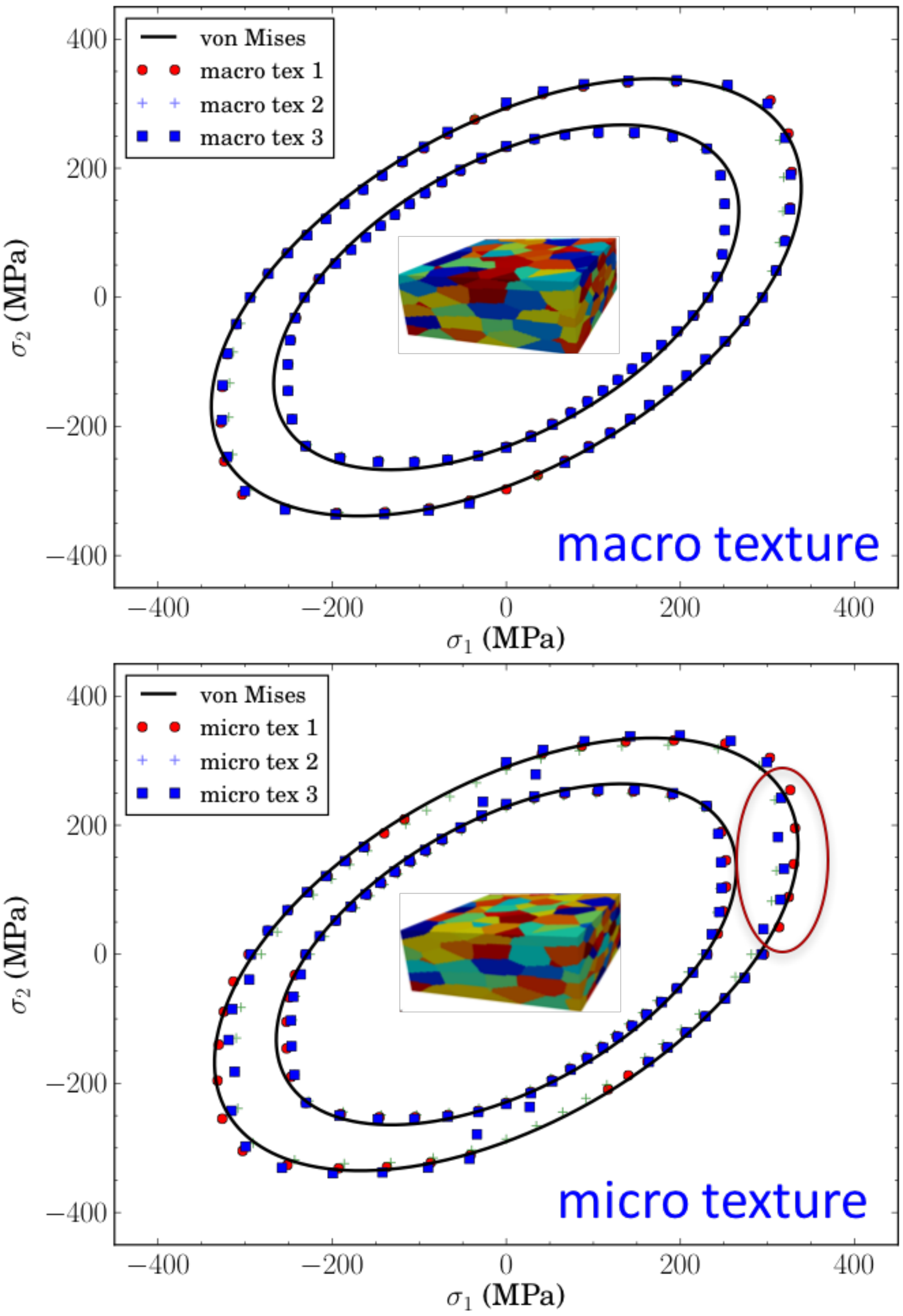

Figure 6.9: Approximated yield surface for macro- and micro-textured polycrystals at 0.2% and 2.0% effective strain.

Due to its simplicity, we have used the models in Figure 6.10 to study the mean and max stress in the idealized particle for a large number of both macro- and micro-texture samples surrounding it. From these simulations, we show an influence of micro-texture on the mean/max stress distribution, specifically a broadening in the tails. The thought experiment suggests that with correlation (micro-texture) there is a certain higher probability that the

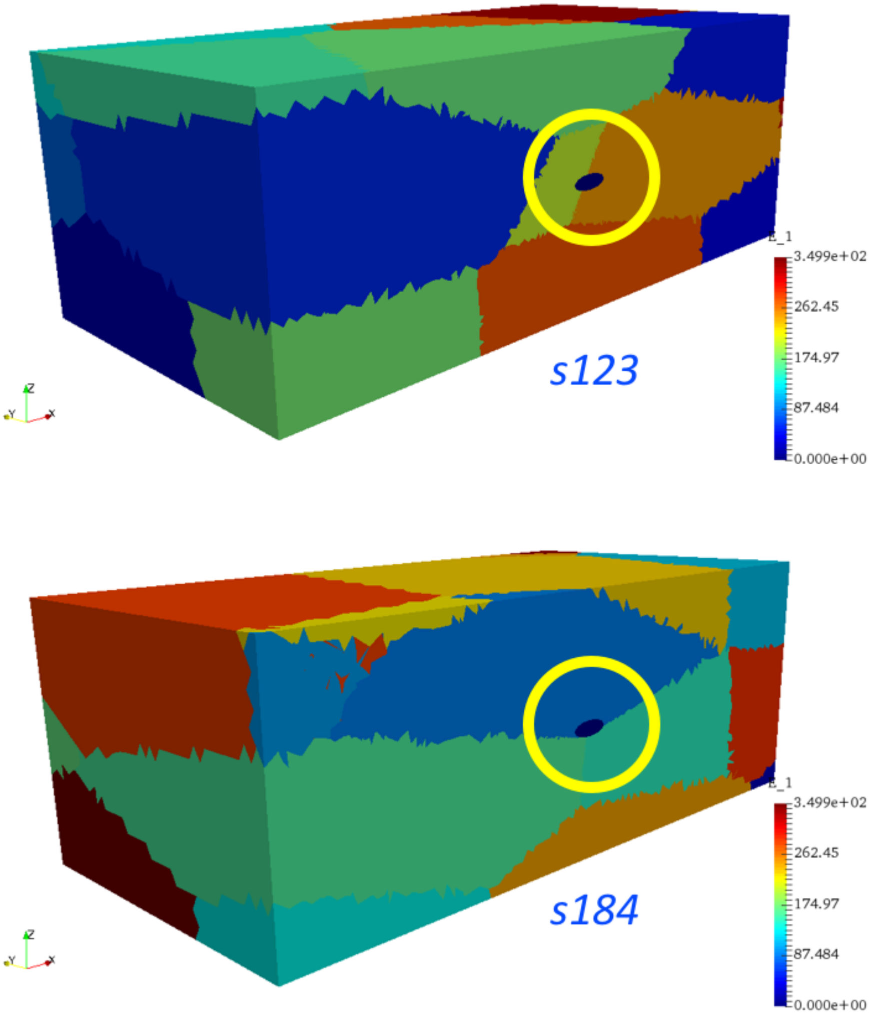

Figure 6.10: Particle/microstructure geometry for two instances of grain morphology. The images are taken at a cross-section intersecting the particle for display.

particle will be located in/near some grains that are aligned in a softer/stiffer manner. Indeed, Figure 6.3 seems to suggest there is a tendency for grains to align in some manner that facilitates (elastic) extension, which suggests a more compliant microstructure. We assume the particle acts elastically and is perfectly bonded at the interface. The particle is iron, with assumed modulus of elasticity of 211 (GPa) and Poisson's ratio of 0.29. We apply displacements extending the simply supported microstructure in the rolling direction. We seek the probability that the applied engineering strain on the microstructure causes particle fracture. That is, the probability that the engineering strain belongs to some limit set S,

$$\Pr(\bar{\epsilon}_{RVE} \in S) \tag{6.2}$$

where $\bar{\epsilon}_{RVE}$ is the average applied engineering strain and S is defined as $S = \{\bar{\epsilon}_{RVE} \in \mathbb{R} : g(\bar{\epsilon}_{RVE}) \leq 0\}$ and g is the limit state funciton defined as $g(\bar{\epsilon}_{RVE}) = \bar{\sigma}_{p,cr} - \bar{\sigma}_p(\bar{\epsilon}_{RVE})$ and $\bar{\sigma}_p$

is some measure of stress in the particle. Here we use the average of the first principle stress over the entire particle volume with $\bar{\sigma}_{p,cr} = 540$ MPa. The mean stress measure is reasonable because the particle is elastic. In some cases the strain on the particle never reached the limit state within the simulated applied strain range. In this case, we use the final points in the history to decide what failure strain to assign. If the slope of the final points is positive, we extrapolate. If the slope is negative, we assign an arbitrarily large value $\bar{\sigma}_{p,cr} = 0.1$, or 10% strain. Note, a negative slope does not imply loss of ellipticity – these are not material point stress-strain relations.

6.3.2 Results

Results from these simulations are shown Figure 6.11. The left-hand side of the figure plots the mean stress versus the nominal applied engineering strain on the microstructure. For the micro-textured samples, there were some number of simulations that experienced numerical difficulties and the calculations failed earlier in simulation time. This is due to the same softer/stiffer bands of material that might drive higher or lower peaks in mean/max particle stress that are making the global matrices harder to solve (ill conditioning). However, from the calculations that were completed, the histograms in the right-hand side of Figure 6.11 support our hypothesis that microtexture leads to higher variability in second-phase particle stress distribution.

Assuming the particle is both perfectly brittle and coherently bonded to the matrix is conservative, as it neglects dissipative mechanisms that exist. On perhaps the opposite spectrum, we assume the particle is elasto-plastic and we use a power-law hardening plasticity model. The form of the hardening equation is

$$\bar{\sigma}(\bar{e}_p) = \sigma_y + A\bar{e}_p^n \tag{6.3}$$

where $\bar{\sigma}$ is the effective stress, $\bar{e}_p$ is the effective plastic strain, σ_y is the yield stress, A and n are hardening modulus and hardening exponent. For the particle properties we use 300 MPa for yield stress, 333 MPa for hardening modulus and 0.15 for hardening exponent. These choices are informed from the literature, but remain a bit arbitrary because the objective is to explore perhaps an upper bound on particle breaking load based on allowing some energy dissipation through a non-fracture mechanisms. Figure 6.12a plots the available simulation results, where again there is some attrition due to convergence issues for certain texture arrangements. We run these calculations on SkyBridge with 128 processors and they take *at least* 28 hours. The stress-strain data is not unlike the elastic-particle results in character, with obviously lower stresses. Interestingly, the distribution of failed particles, shown in Figure 6.12b and 6.12c is even wider, ranging above 100% strain. This is an artifact of our choice of plasticity parameters for the particle and our extrapolation routine for particles that don't fail within the simulated time. It is also unlikely to be true [16].

In an effort to ground the observations closer to reality, we consider the maximum first principle stress that occurs in any element in the particle volume. Figure 6.13 provides comparably information to Figure 6.12. Here, the stress-strain tends not to drop because

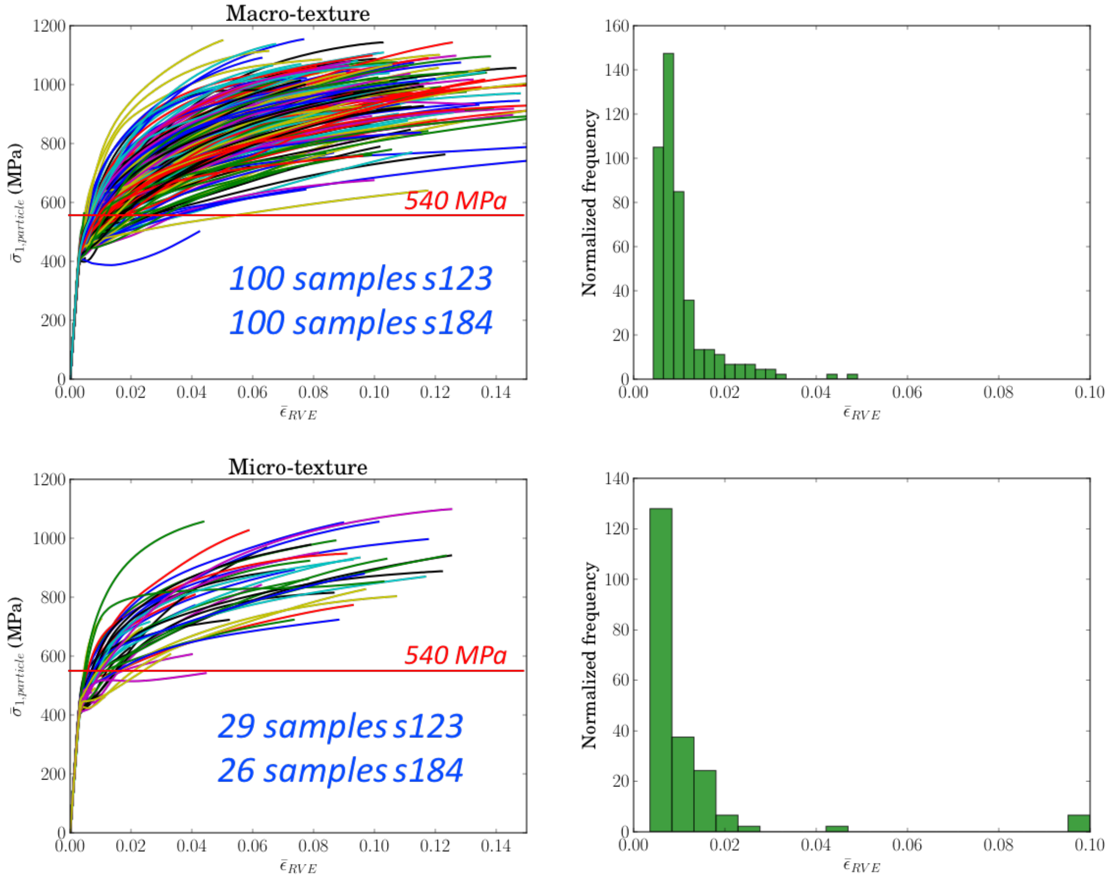

Figure 6.11: Particle stress-strain relations for a variety of surrounding textures.

there is always a hot element in the particle. The distribution shown with Figures 6.18b and 6.18c is more like the elastic-particle results and suggests less discrepancy between macro- and micro-texutre. Nevertheless, there tails of the mirco-textured samples still appear broader.

6.4 Example 4 – multiscale now!

6.4.1 Formulation

Our target has been predicting performance, crack nucleation and failure of the 6-notched specimen presented in Chapter 2, Figures 2.12, 2.13 and Appendix B. Our approach in this example is to build a FE model at the engineering length scale of the 6-notched specimen, calibrate it to the available data plotted in Figure 2.11 and use prediction calculations to define a subdomain to embed our microstructure model. We do not fully implement the hierarchical algorithm because, frankly, we ran out of time.

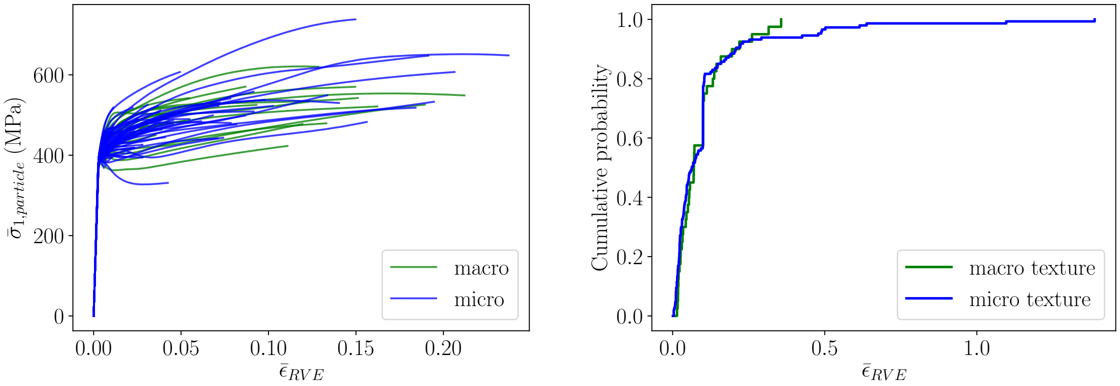

(a) stress-strain – EP particle

(b) CDF – EP particle

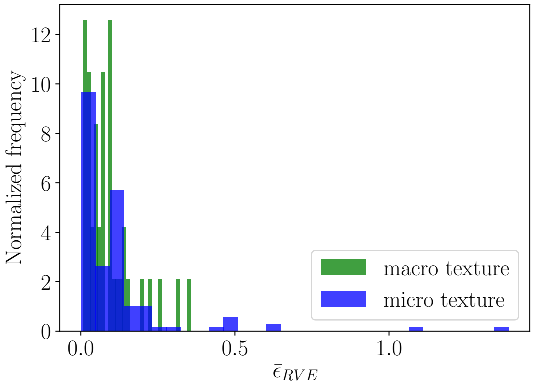

(c) Histogram – EP particle

Figure 6.12: Statistics of broken particles with mean stress metric when the particle is assumed to be an elasto-plastic material with power-law hardening.

First we built FE models of the smooth, gradual-notched, and sharp-notched tension specimens and used MatCal [8] to calibrate the constitutive parameters of the Hill plasticity model. MatCal uses optimization algorithms to solve the inverse problem between the FE predictions and available data, normalized load versus normalized displacement in our case. The procedure requires many FE solves and is deeply involved and computationally expensive. We performed teh calibration first to the smooth and gradual-notched tension data to get a reasonable fit for the plasticity parameters. Subsequently, we performed the fit to the gradual- and sharp-notched tension data for the damage parameters. This was not the focus of our research effort so we sought a calibration that was reasonably accurate. Application of the hierarchical methodology would include fitting all available data, building a translation model for the parameters, constructing an SROM and perform MCS with this model to construct the engineering scale estimate for reliability [6]. Figure 6.14 shows the results of the calibration to all available data and the parameters resulting parameters are tabulated in Table 6.6.

With the calibration complete, we turned the focus on predicting performance of the

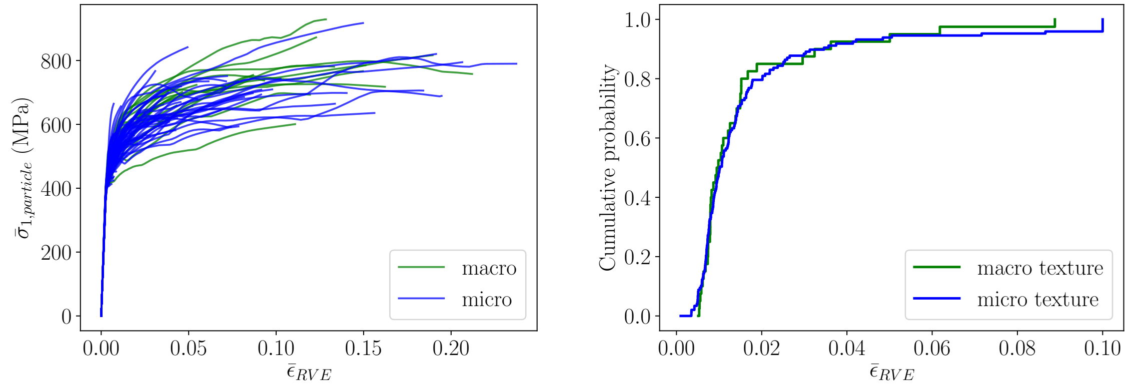

(a) stress-strain – EP particle

(b) CDF – EP particle

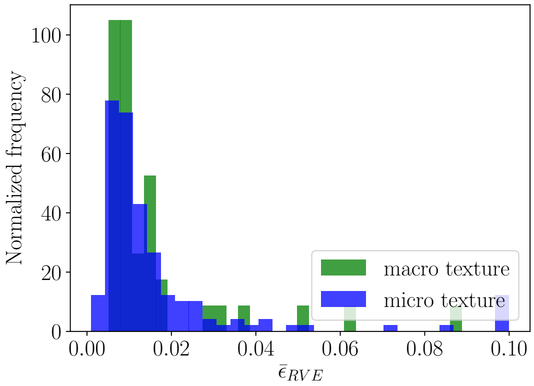

(c) Histogram – EP particle

Figure 6.13: Statistics of broken particles with maximum stress metric when the particle is assumed to be an elasto-plastic material with power-law hardening.

6-notched plate. Our goal here is to determine where to embed the polycrystal model. Figure 6.15 plots the force-displacement response that was predicted for the 6-notch specimen along with the available 6 test results. In general, the engineering scale model peforms reasonably well, but leaves no prediction about the uncertainty in strain-to-failure that is observed in the tests. Again, with the method described above, one could make a coarse UQ estimate, but our focus is on coupling the length scales.

Figures 6.16 and 6.17 show fields predicted by the engineering scale FE model. Figure 6.16 shows the von Mises effective stress (top) and triaxiality (bottom) contour plots. Clearly the middle set of notches are the most active for this deterministic scenario. Figure 6.17 shows the triaxiality contour plot focused on a cross-section at the mid-plane and at the middle notch. This is the location of highest triaxiality and identifies the hot spot where we will embed the microstructure with our multiscale approach. We use the micro-textured microstructure with elastic and brittle particle presented in Example 6.3 and our MPC approach for coupling.

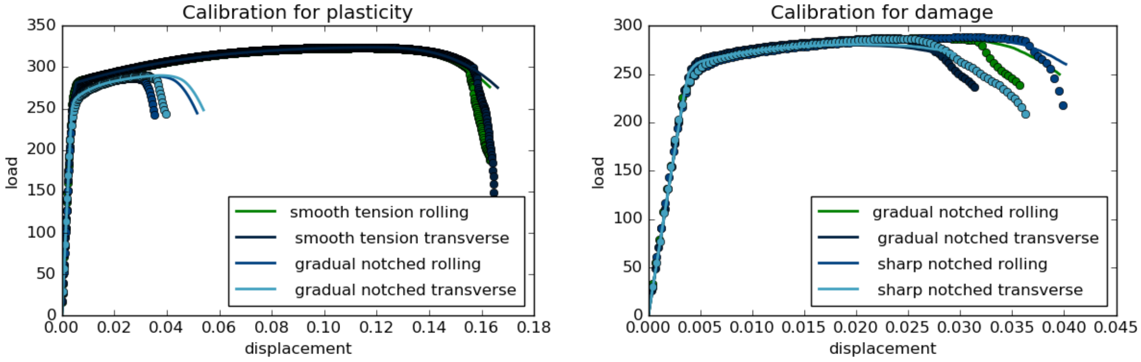

(a) plasticity (b) damage

Figure 6.14: Calibration results for calibrating the Hill plasticity model with damage to the smooth, gradual-notch, and sharp-notch tenstion data. Calibrations were performed with MatCal.

parameter	value
R11	1.00e-00
R22	8.07e-01
R33	8.00e-01
R12 = R23 = R31	9.50e-01
yield (MPa)	2.80e+02
hardening (MPa)	1.16e+02
recovery	1.11950e+01
damage exponent	9.875

Table 6.6: Hill plasticity parameters calibrated to the available smooth, gradual-notched and sharp-notched tension data.

6.4.2 Results

Figure 6.18 quantifies the results of the load in the particle for 46 realizations of microtexture. The strain measure here is different then for the microstructural plots. Here we use the nominal applied strain on the 6-notch specimen, so that the strains coincide with Figure 6.15. The critical strains are in the range 0.001 to 0.004, noticeably lower than the apparent strain-to-failure in of the plate, which ranges from 0.035 - 0.039. These results indicate that a particle in the high-triaxiality region in front of the notch is likely to fracture very early in loading. This is somewhat inconsistent with other findings that suggest particles don't fracture until after peak load on the specimen [16]. However, there are other findings in the fatigue literature that suggest surface particles fracture upon first fatigue cycle [44]. The two scenarios are for particles embedded in vastly different constraint environs. Nonetheless, it is reasonable to suspect our results are still missing some key physics as we assume the particle is elastic with no dissipation. The next steps for this research are to perform these multiscale calculations with the elasto-plastic constitutive model for the

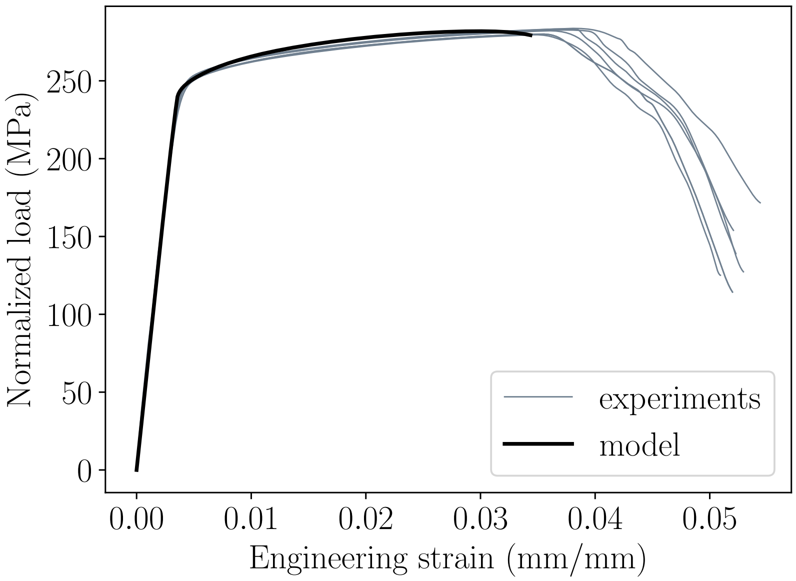

Figure 6.15: Engineering scale simulation plotted on the experimental observations.

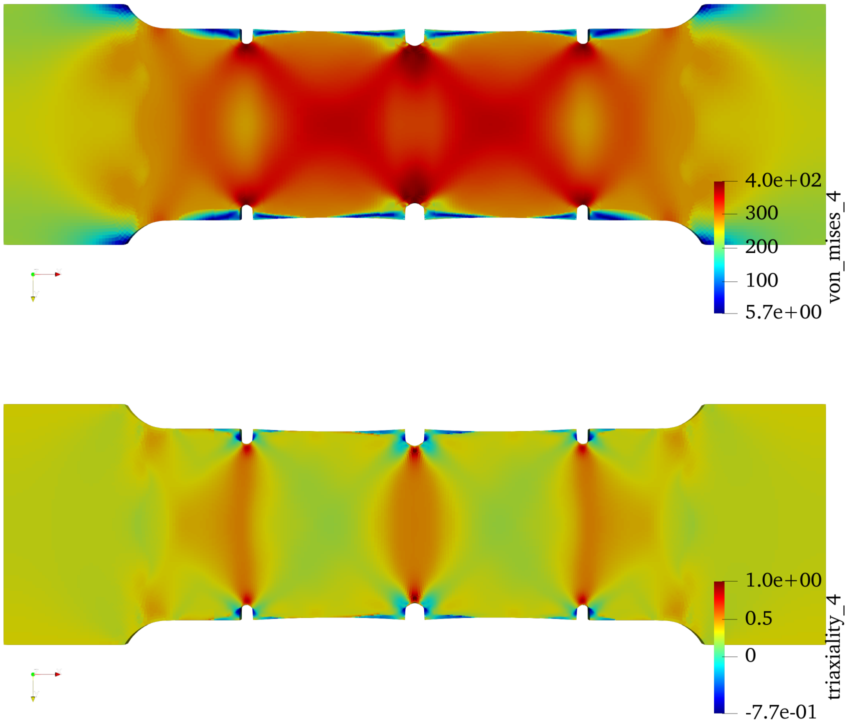

Figure 6.16: Effective stress contour contour plot (top) and triaxiality contour plot (bottom).

particle and to compare our SROM approach with the brute force MCS present here.

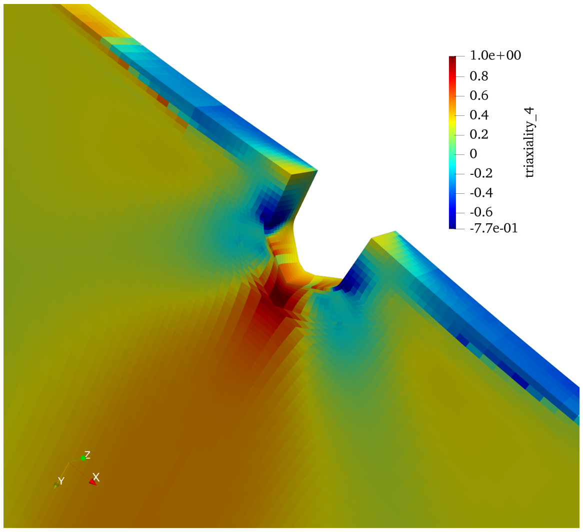

Figure 6.17: Magnified view of the triaxiality on a bisecting cross-section of the specimen at the middle notch identifying the hot spot from the engineering level simulation.

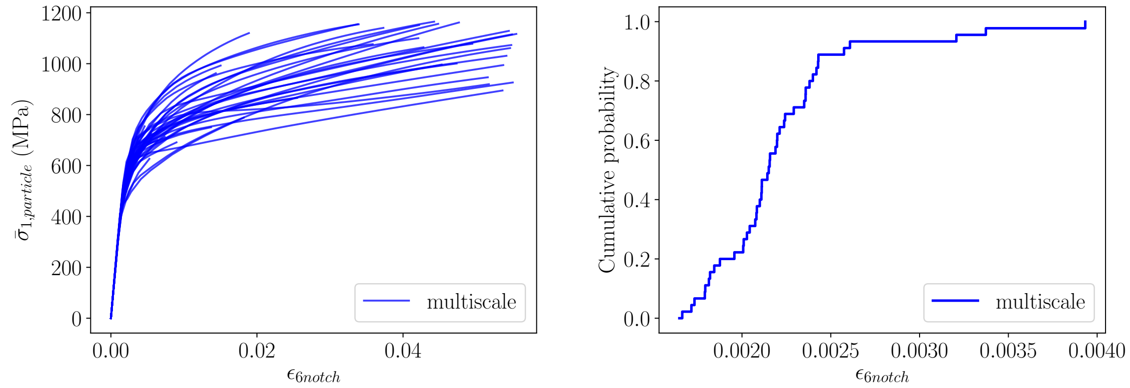

(a) Stress-strain – multiscale (b) CDF – multiscale

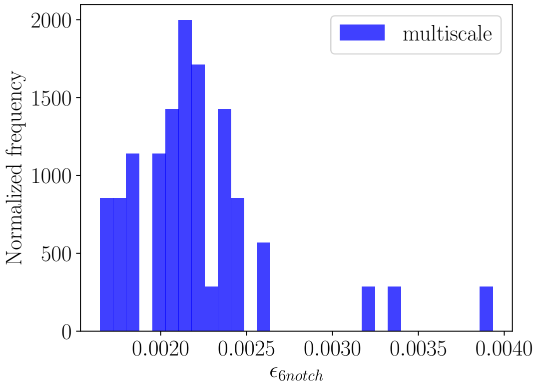

(c) Histogram – multiscale

Figure 6.18: Statistics of broken particles when the particle is coupled to a Hill plasticity engineering scale model.

Chapter 7

Quantifying dislocation accumulation via a combined EBSD - in situ SEM deformation approach

The objective of this research is to understand how different aspects of the microstructure in AA 6061-T6, including grain boundary and triple junction state, grain size, and presence of second phase particles, interact synergistically to promote localized dislocation accumulation as a function of strain and depth from the sample surface. The work was motivated by our multi-scale DIC efforts and a desire to collect evidence for the next length scale down the hierarchy. Outcomes of this discovery work and the techniques developed herein can be used to inform model development for damage at the microscale, calibrate those models, and provide validating evidence for our simulations that include the material's second phase particles.

7.1 Experimental

Six-notch AA 6061-T6 tensile bars were ground and polished using successively finer levels of SiC paper, followed by diamond paste and a colloidal silica finish. A damage-free surface was then achieved by electropolishing the samples using a methanol-perchloric electrolyte. Once polished, the samples were loaded into a Kammrath-Weiss model in situ SEM straining stage that has been modified to facilitate EBSD-based analysis during deformation. Samples were strained incrementally, with EBSD scans collected at arrested stages of deformation using an EDAX/TSL system. All EBSD scans reported here were collected near the center notch of the specimens. Strain levels are taken from cross-head displacements read directly from the stage and should be taken as nominal values only. Samples were characterized using both traditional electron backscatter diffraction (EBSD) analysis as well as high angular resolution EBSD (HREBSD) using OpenXY, an open-access software package for HREBSD analysis. In contrast to traditional EBSD measurements, HREBSD relies on capturing and storing high-quality EBSD patterns during a scan. Cross-correlation based measurements are then used to measure minute shifts in Kikuchi bands in each pattern relative to a grain reference pattern. These shifts can be related to elastic strains and rigid body rotations of the underlying crystal lattice, providing two orders of magnitude higher angular resolution measurements in comparison to traditional EBSD and the resolution of all nine components of the elastic strain gradient tensor to within 0.0005 [45, 46]. The accumulation of geometrically necessary dislocations (GND), or those dislocations with non-opposing Burgers vectors in a given region, leads to internal-grain orientation gradients. These rotations can be quantified via traditional EBSD or, for higher precision measurements, HREBSD and related to Nyes dislocation density tensor via Kroners formulation [47, 48]:

$$\alpha_{ij} = \kappa_{ki} - \delta_{ki}\kappa_{pp} + e_{klj}\varepsilon^{e}_{ij,l} \tag{7.1}$$

Where κ is the lattice curvature and is defined by:

$$\kappa_{ij} = \frac{\partial \theta_k}{\partial x_i} \tag{7.2}$$

$\varepsilon^{e}_{ij,l}$ is the spatial derivative of the elastic strain, θ_k is the rotation vector as measured by HREBSD, e_{klj} is the Levi-Civita symbol, δ_{ki} is the Dirac delta function, and α_{ij} is the dislocation density tensor. The dislocation tensor is a statistical representation of the local dislocation state where columns represent the line direction and rows represent the Burgers vectors of the dislocations. The total GND density can then be estimated by taking the L1 norm of α_{ij}, as described by Ruggles et al. [49]. More details on the calculations and expected sensitivity can be found in [50, 51].

7.2 Results and analysis

7.2.1 Dislocation distribution as a function of depth from the surface

Figure 7.1 shows EBSD scans and the associated GND density maps collected from a 2%-strained sample at the surface (Fig. 7.1a-b), at a depth of 200 μm (Fig 7.1c), and at a depth of 400 μm (Fig 7.1d), with material removed between scans by mechanical and electro-polishing. As can be seen, at the surface of the deformed sample, the dislocations accumulate in lobe structures extending at 45° angles from the notch tip. With increasing depth from the surface, the dislocations increasingly concentrate near the center of the notch.

This dislocation distribution can be seen more clearly in the column-averaged GND density measurements, plotted in Figure 7.1e. These plots were filtered using a mean filter with a fifty-pixel (75 μm) window to reduce noise levels. Finite element analysis (FEA) simulations of the elastic strain field, assuming a homogeneous material, were conducted using the same geometry and applied stress levels (220 MPa). Cross-sections of the stress field corresponding to the depth scans are shown as insets in Figure 1b-d. Similar to the measured dislocation density fields, the stress distribution appears as a two-lobed structure on the sample surface and becomes increasingly concentrated near the notch tip with increasing depth from the sample surface.

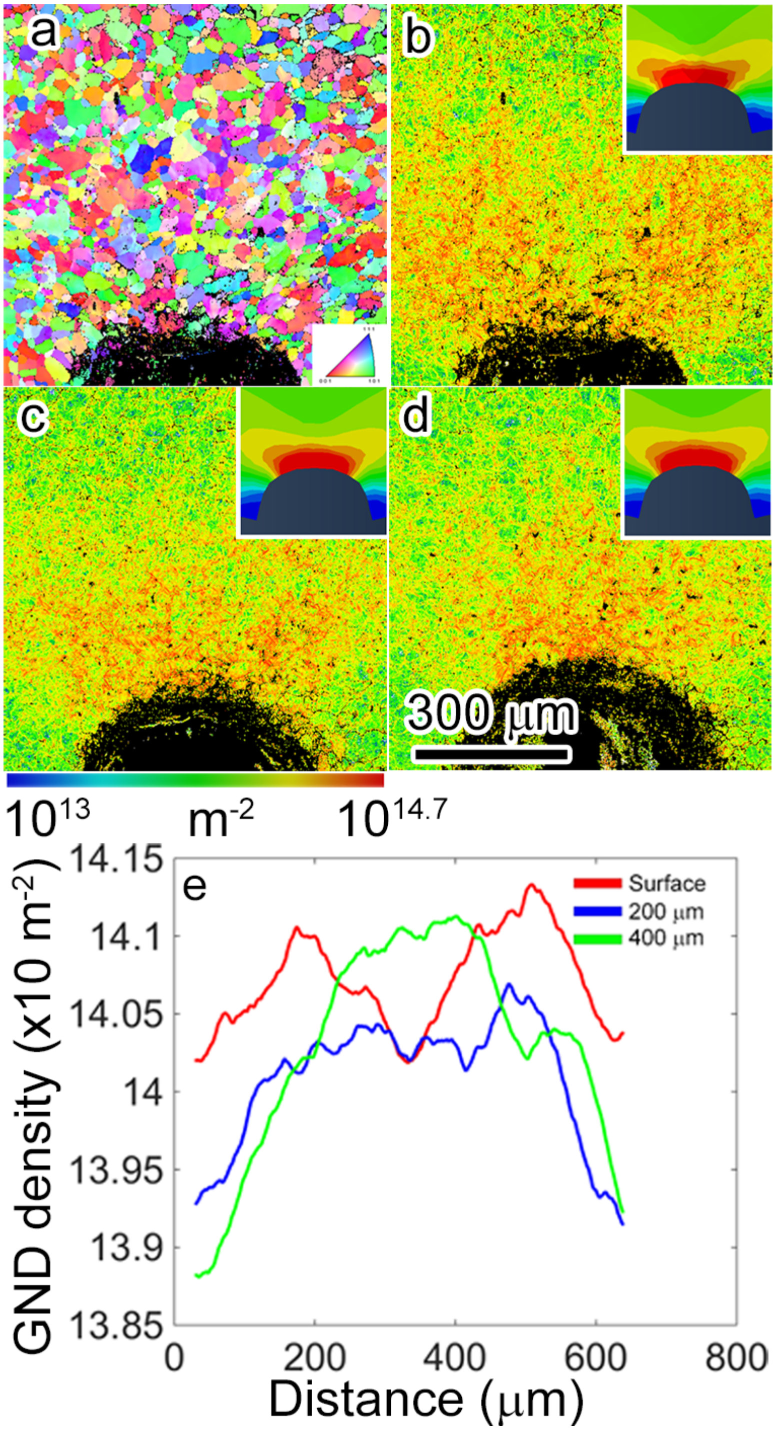

Figure 7.1: (a) Inverse pole figure (IPF) map of notched AA 6061-T6 sample strained to 2%. (b) GND density map generated from orientation data. (c-d) GND density map at 200 and 400 μm from surface, respectively. Insets in b-c show FEA predictions of elastic strain field. (e) column-wise average of GND density taken from b-d. Data are shown on a lograrithmic scale.

7.2.2 Dislocation distribution as a function of strain

In order to investigate the deformation behavior of the AA 6061-T6 as a function of strain level, samples were strained in situ in the SEM, with straining interrupted and EBSD scans collected every 0.2% strain between 1% and 2%. A subset of the GND maps generated from these scans are shown in Figure 7.2. As can be seen, the deformation lobe structure, similar to what is seen in Figure 1, develops early in the deformation. It is also apparent in the image that localized "hotspots" of deformation, or regions of high dislocation density, develop far ahead of the notch tip, during deformation. One such region is magnified in insets in Figure 7.2, showing GND accumulation localization to a region surrounding two intermetallic constituent particles, identifiable as black spots in the GND map.

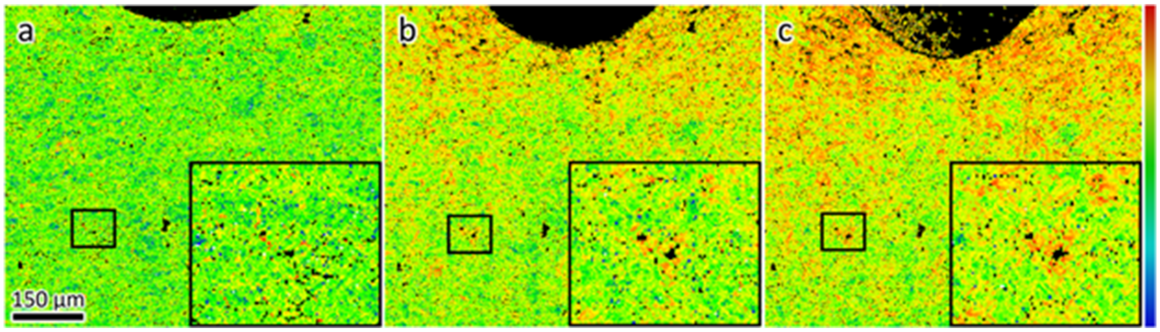

Figure 7.2: GND distribution in front of notch at (a) 0% strain, (b) 1.4% strain, and (2) 1.8% strain. GND density plotted on logarithmic scale from 10^3 to $10^{14.8}$ m^{-2}. Insets show dislocation accumulation around intermetallic constituent particles.

HREBSD scans were also collected during in situ deformation at higher magnification around features of interest. These scans were collected at 0%, 1%, and 2% strain around a triple junction (Fig. 7.3a-f) and near intermetallic constituent particles (Fig. 7.3g-l). Near the triple junction, it can be seen that dislocation accumulation occurs preferentially early on in the deformation, forming a banded structure (Fig. 7.3e, lower right grain). By 2% strain, dislocation accumulation led to the formation of a 20° rotation boundary. In the region surrounding the intermetallic constituent particles, there is little indication of dislocation accumulation at 1% strain (Fig. 7.3h). However, by 2% strain, dislocation bands similar to those shown in Figure 7.3f are clearly resolved and the region near the particle has undergone significant grain refinement(Fig. 7.3i and l). In both cases, the microstructure appears to concentrate dislocation accumulation, leading to grain refinement and sub-grain structure formation.

7.2.3 Quantification of microstructure/dislocation accumulation relationship

The above-described results are largely observation based, providing insight into strain localization mechanisms but lacking statistical significance. In order to quantify the influ-

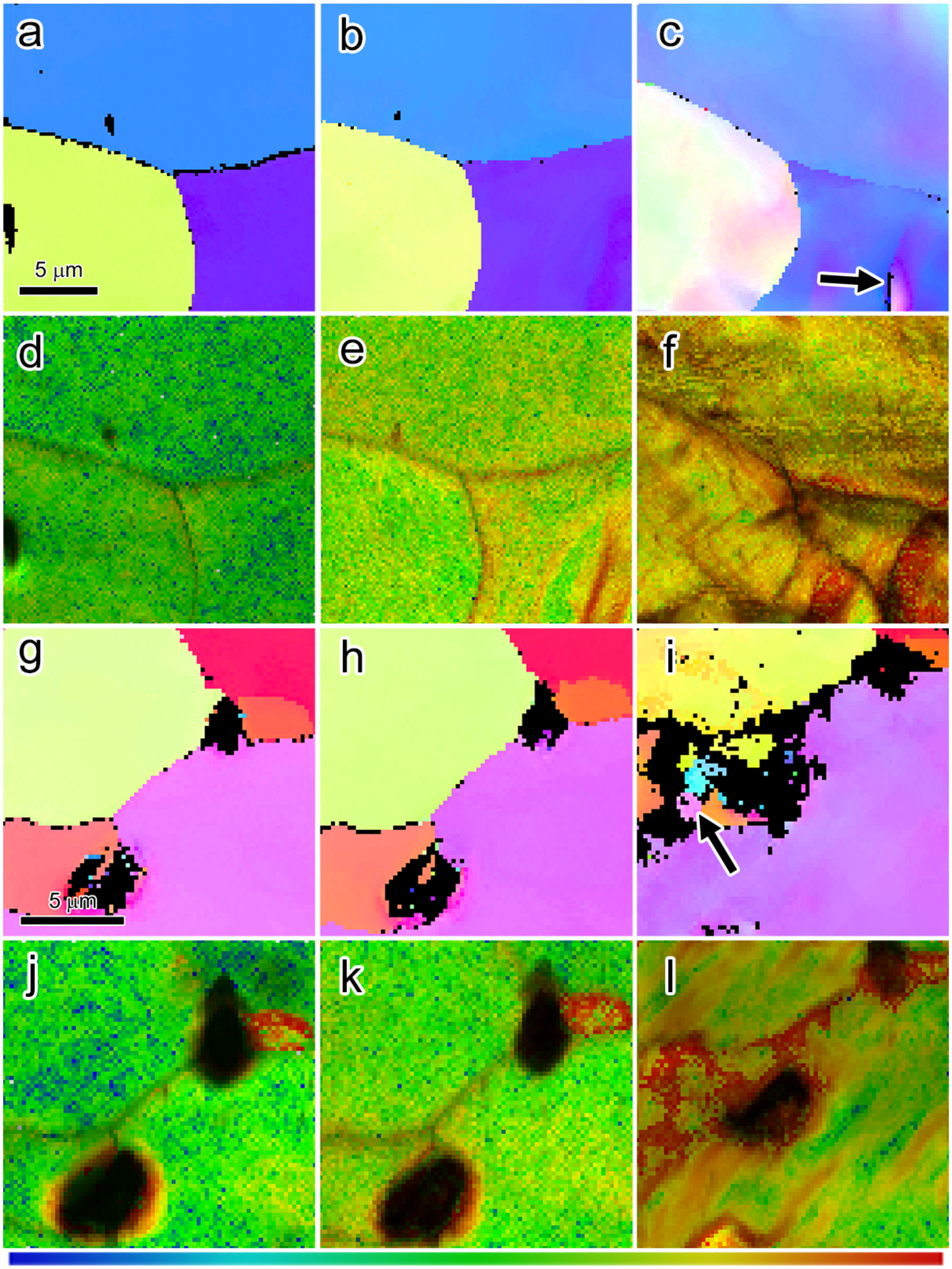

Figure 7.3: Inverse pole figure maps (a-c, g-i) and GND density maps (d-f, j-l) at 0%, 1%, and 2% strain at two regions of interest. GND density plotted on log scale from 10^{13} to $10^{15.6}$ m^{-2}.

ence of different microstructural features on dislocation accumulation, it is important to recognize the various ways in which a microstructure can be represented. Figure 7.4 demonstrates six unique ways in which the same microstructure can be presented, with each pixel in the scan representing either a local property of the material (orientation, grain size, or GND density shown in Fig. 7.4a-c, respectively) or the proximity to a feature of interest (intermetallic constituent particle, grain boundary, or triple junction shown in Fig. 7.4d-f, respectively). Once the microstructure is represented in different forms of interest, it becomes straightforward to relate different aspect of the microstructure to each other. This process is demonstrated for the EBSD scan collected 200 μm from the surface of the material (shown in Fig. 7.1c) with a focus on relating the local GND density to four aspects of the microstructure: proximity to intermetallic constituent particles, proximity to grain boundaries, proximity to triple junctions, and grain size. The grain sizes and distances from each point to the microstructural feature of interest were calculated using the orientation data for grain boundary and triple junction locations and by thresholding the EBSD image quality map to locate the intermetallic constituent particles. Once these maps are generated, the average GND density was calculated as a function of distance from features of interest; plots of these calculations are shown in Figure 7.5a. In Figure 7.5b, the data are further segmented as a function of grain size, with data points located in grains with diameter below approximately 45 μm plotted separately from data points located in larger grains. An additional line is also plotted representing data points with none of the targeted microstructural features of interest within the given range.

The data clearly show that the GND density is inversely proportional to the distance from all three features of interest, with triple junctions and constituent particles having a larger influence than grain boundaries. Interestingly, grain size appears to have little influence on the dislocation accumulation behavior near triple junctions or grain boundaries, but has a significant effect on dislocation behavior near intermetallic particles, with smaller grains promoting the accumulation of dislocations. Overall, the data suggest that the locations of highest dislocation accumulation are intermetallic particles located in smaller grains.

This quantitative information was used as a guide in the investigation of strain localization in front of a crack tip in AA 6061-T6. A sample was strained until crack nucleation and a cracked intermetallic particle was located ahead of the crack tip (shown in Fig. 7.6a). A HREBSD scan was collected around the crack tip and used to generate a dislocation density map. In addition, a kernel average misorientation (KAM) map was generated, which supplies qualitative dislocation density information and is less sensitive to noise in the scan. Particle cracking has been widely associated with crack initiation in ductile failure of AA 6061-T6, but multiple theories exist on what causes the particle cracking to occur and how particle cracking leads to crack initiation. Tanaka and Mura reviewed three types of fatigue crack initiation mechanisms at inclusions, including debonding and dislocation emission, dislocation impingement on inclusions leading to stress concentration and particle cracking, and dislocation generation from the inclusion/matrix interfaces due to elastic strain mismatches [52]. Although the present work investigates deformation under monotonic loading, many of the same mechanisms can be expected to be active.

In the GND density map (Fig. 7.6), it can be seen that dislocations accumulated preferentially on one side of the particle; in this case the side closer to the crack. This suggests that the dislocation accumulation led to the particle cracking, as either dislocation genera-

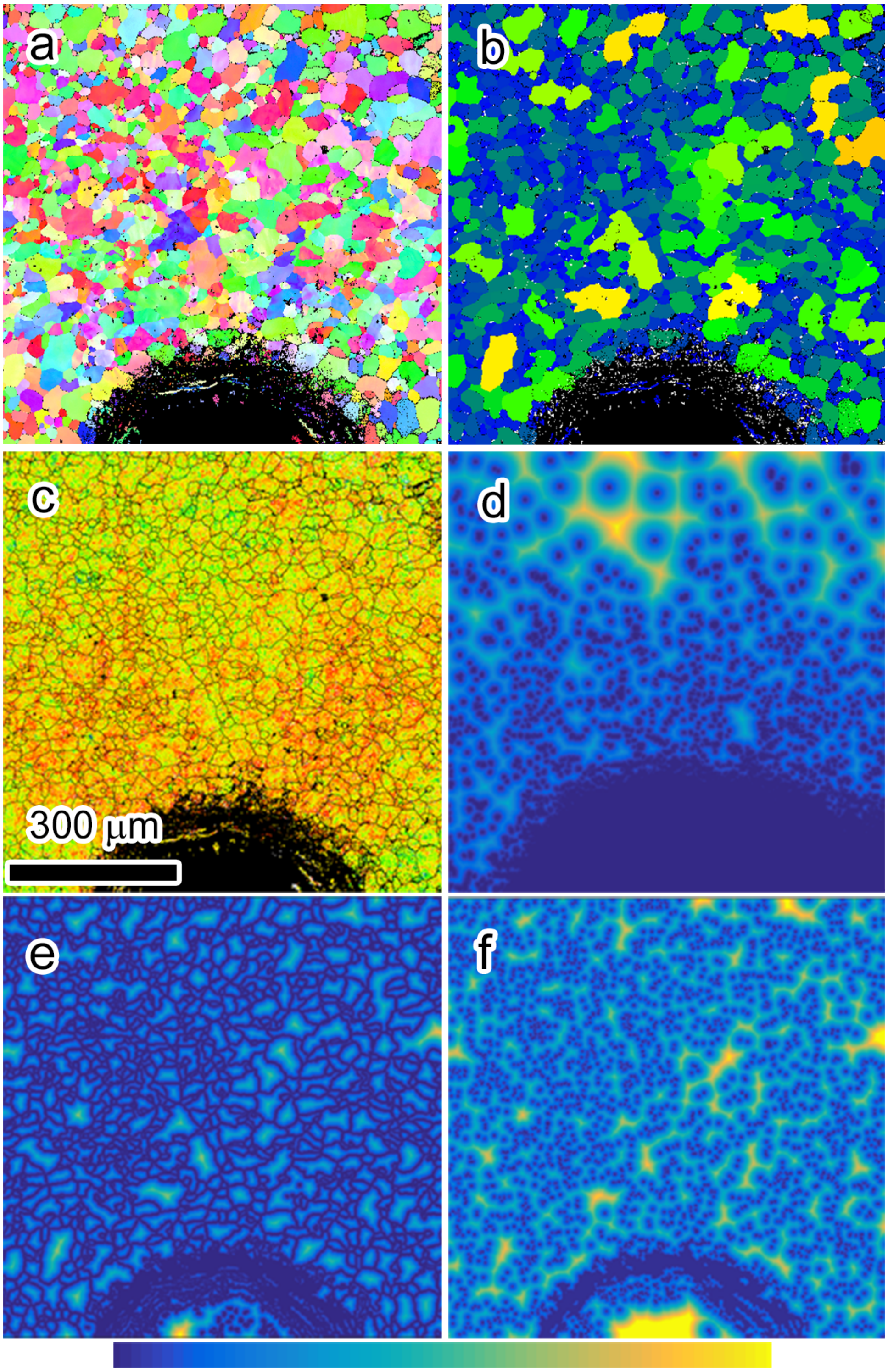

Figure 7.4: Different microstructural representations of scan shown in Fig 7.1c. (a) IPF map, (b) grain size map, (c) GND density map, (d) proximity to second phase particles, 0 - 40 μm, (e) proximity to grain boundary, 0 - 20 μm, (f) proximity to triple junction, 0 - 20 μm.

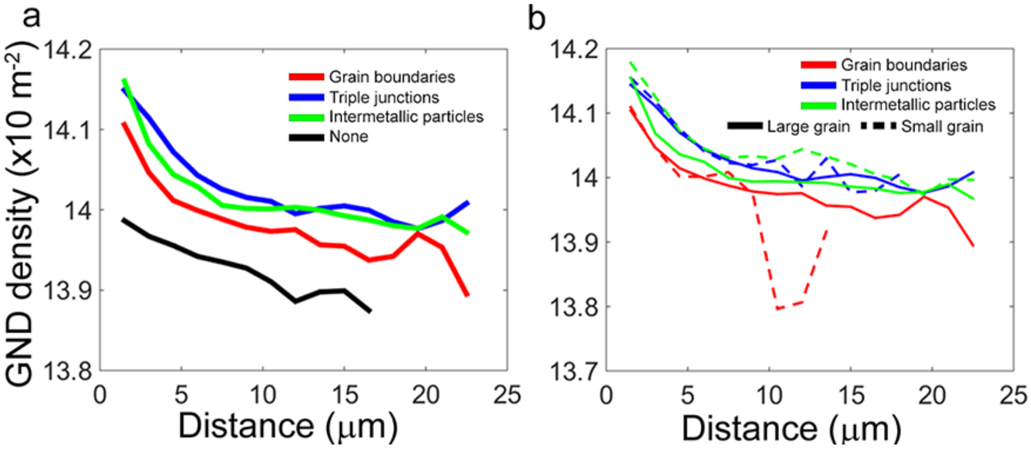

Figure 7.5: Average GND density as a function of distance from microstructural feature of interest. 'None' indicates that no three of the listed features are with the given distance. (b) Data separated between large grains (D > $40\mu m$) and small grains (D < $20\mu m$). GND density plotted on logarithmic scale.

tion from the matrix/inclusion interface or from a debonded region would most likely lead to higher levels of dislocation accumulation leading away from the crack tip. The associated KAM map was overlaid with the EBSD pattern quality map to give a sense of the local surface features. As can be seen, multiple small particles are distributed in the region surrounding the intermetallic particle. Based off their size, it is assumed that these are dispersoids in the matrix. Interestingly, it can be seen that dislocations accumulate preferentially around these dispersoids, suggesting that there is a synergistic effect between the intermetallic particle and the dispersoids, leading to high levels of dislocations accumulation.

7.3 Summary

Microstructural heterogeneities inherent to AA 6061-T6, including the distribution of second-phase particles and grain structure-related inhomogeneities associated with all polycrystalline materials, lead to localization of dislocation accumulation. The relationship between microstructural inhomogeneities and dislocation accumulation can be quantified and explored in detail, including how the dislocation distribution evolves with strain and depth from the free surface, using a combined EBSD/in situ SEM deformation approach. In this study, it was shown that dislocation accumulation occurs preferentially near intermetallic particles, in particular those that are located in small grains. This observation can motivate future work along the lines discussed in Chapters 3 and 4. The dislocation distribution surrounding a cracked particle suggests that the particle cracking is induced from stresses associated with dislocations piling up at the particle/matrix interface.

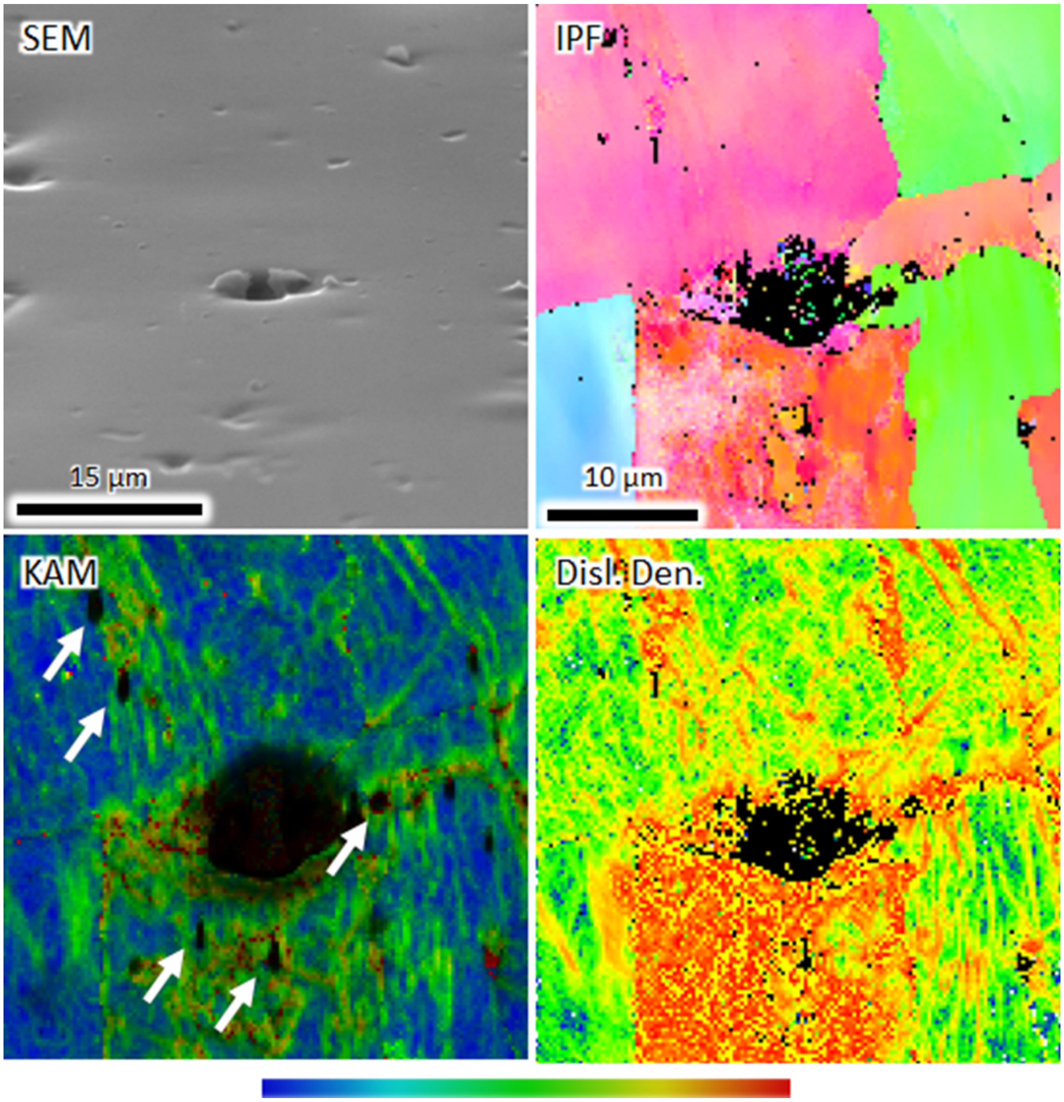

Figure 7.6: Secondary electron image (SEM) and HREBSD scan data around a cracked intermetallic particle found ahead of a crack tip. KAM map is overlaid on an EBSD pattern image quality map to give quasi-topographical information. White arrows in KAM map indicate the presence of dispersoids. KAM map scale is linear from 0 - 5°and for GND density map is logarithmic from $10^{13.85}$ to $10^{15.5}$ m^{-2}.

Chapter 8

Conclusions

In summary, we developed tools for modeling uncertaint microstructure of AA 6061-T6 and propagating those uncertainties through forward calculations to provided estimates of particle cracking, leading to crack nucleation. Our approach outlines a hierarchical, multifidelity method that systematically focuses computational resources at hotspots identified by engineering-scale simulations and combines the results from multiscale analyses to maximize efficiency. Our engineering-scale simulations use Hill anisotropic plasticity and damage. The multiscale simulations focused on the variability associated with random grain orientation, including spatial correlation to capture grain misorientation, and its influence on fracture load in second-phase particles. During research to prepare our microstructural finite element models for multiscale analysis, we explored the effect of a convenient simplification for the geometric representation of grain boundaries. We employed the newly developed Sandia tool Sculpt[2] to develop FE meshes of microstructures whose mesh boundaries conform in some sense to the materials grain boundaries. A simpler approach is to overlay grain orientation onto an existing background mesh resulting in grain boundaries that are not smooth and that have sharp corners introduced by the background mesh. For the problems that we have considered for this aluminum alloy and that explicitly include a second-phase in the microstructure, it appears less important to carefully treat the grain boundary. Further, an important contribution of this work was the development of random-field reduced order models (RFROMs) to expedite MCS of polycrystalline materials.

Our experimental efforts developed a multiscale digital image correlation (DIC) observations for use in model validation, and through high-resolution electron backscatter diffraction (EBSD) measurements and serial section, identify key relationships between microstructural features and dislocation density leading to damage and crack nucleation. The multiscale DIC attempted to capture two distinctly different length scales of strain data in situ, so that engineering-scale and microstructural strain fields could be simultaneously observed. While ultimately unsuccessful in the lifespan of this project, many speckle patterns were ruled out and a thin-film remodeling method was identified as a strong candidate. Work on the topic will continue and the data will be useful for validating multiscale calculations. The high-resolution EBSD work was achieved through the Academic Alliance LDRD program and collaboration with Professor Josh Kacher at Georgia Institute of Technology (GT). The Kacher contract was extremely productive with the only regret being it was a one-year contract in the final year this project. The GT data captures dislocation accumulations occurring in the presence of a strong gradient caused by a sharp notch at grain boundaries, grain boundary triple junctions, and second-phase particles. This information is measured at the surface of a specimen and at a multiple serial-sectioned depths below the surface approaching the midplane of the specimen. This data is very informative about ranking the importance of microstructural features for damage processes and can be used in the future for calibrating damage models at the microstructural length scale.

The following list itemizes our findings and newly developed capabilities:

- a tool to model random fields, calibrated to data, that generates statistically equivalent samples for Monte Carlo simulation;
- a reduced-order model for random fields and it was shown to be accurate and efficient for propagating uncertainty;
- understanding of the impacts of modeling assumptions about grain boundaries in the presence of a material's second phase and concluded that overlay microstructures are sufficient in some cases, despite leading to artificially roughened grain boundaries;
- understanding of the effects of microtexture on particle breaking load in second-phase particles and found that microtexture broadens the probability density function for crack nucleating load in the particle;
- multiscale simulations coupling the engineering scale to the material microstructural scale concurrently and with one-way submodel coupling and noting various differences in the particle breaking load;
- concurrently coupling the engineering scale with a microstructure that contains a crack nucleating agent (second-phase), in 3D and with Monte Carlo simulation for estimates of probability;
- using a combined EBSD/in situ SEM deformation approach, it was shown that dislocation accumulation occurs preferentially near intermetallic particles, in particular those that are located in small grains.

References

[1] Adam D Kammers and Samantha Daly. Digital image correlation under scanning electron microscopy: methodology and validation. *Experimental Mechanics*, 53(9):1743–1761, 2013.

[2] Hojun Lim, Fadi Abdeljawad, Steven J Owen, Byron W Hanks, James W Foulk, and Corbett C Battaile. Incorporating physically-based microstructures in materials modeling: Bridging phase field and crystal plasticity frameworks. *Modelling and Simulation in Materials Science and Engineering*, 24(4):045016, 2016.

[3] J.M. Emery, J.D. Hochhalter, P.A. Wawrzynek, G. Heber, and A.R. Ingraffea. Ddsim: A hierarchical, probabilistic, multiscale damage and durability simulation system – part i: Methodology and level i. *Engineering Fracture Mechanics*, 76(10):1500 – 1530, 2009. MatModels 2007.

[4] John M. Emery and Anthony R. Ingraffea. *DDSim: Framework for Multiscale Structural Prognosis*, pages 469–496. Springer US, Boston, MA, 2011.

[5] Mircea Grigoriu. A method for solving stochastic equations by reduced order models and local approximations. *Journal of Computational Physics*, 231(19):6495–6513, 2012.

[6] John M Emery, Richard V Field, James W Foulk, Kyle N Karlson, and Mircea D Grigoriu. Predicting laser weld reliability with stochastic reduced-order models. *International Journal for Numerical Methods in Engineering*, 103(12):914–936, 2015.

[7] Brian T. Lester and William M. Scherzinger. An evolving effective stress approach to anisotropic distortional hardening. *in preparation*, 2017.

[8] Kyle N. Karlson, James W. Foulk, Arthur A. Brown, and Michael G. Veilleux. Sandia fracture challenge 2: Sandia california's modeling approach. *International Journal of Fracture*, 198(1):179–195, Mar 2016.

[9] M Grigoriu. Reduced order models for random functions. application to stochastic problems. *Applied Mathematical Modelling*, 33(1):161–175, 2009.

[10] Karel Matouš and Antoinette M. Maniatty. Finite element formulation for modelling large deformations in elasto-viscoplastic polycrystals. *International Journal for Numerical Methods in Engineering*, 60(14):2313–2333, 2004.

[11] John M. Emery. *DDSIM: A hierarchical, probailistic, multiscale damage and durability simulation methodolgy*. PhD thesis, Cornell University, 2007.

[12] James W. Foulk III. Strong concurrent multiscale coupling. Technical Report SAND2017-xxx, Sandia National Laboratories, 2017.

[13] Benjamin Peherstorfer, Karen Willcox, and Max Gunzburger. Survey of multifidelity methods in uncertainty propagation, inference, and optimization. *Preprint*, pages 1–57, 2016.

[14] Benjamin Peherstorfer, Boris Kramer, and Karen Willcox. Combining multiple surrogate models to accelerate failure probability estimation with expensive high-fidelity models. *Journal of Computational Physics*, 341:61–75, 2017.

[15] Benjamin Peherstorfer, Tiangang Cui, Youssef Marzouk, and Karen Willcox. Multifidelity importance sampling. *Computer Methods in Applied Mechanics and Engineering*, 300:490 – 509, 2016.

[16] A Ghahremaninezhad and K Ravi-Chandar. Ductile failure behavior of polycrystalline al 6061-t6. *International journal of fracture*, 174(2):177–202, 2012.

[17] A Ghahremaninezhad and K Ravi-Chandar. Crack nucleation from a notch in a ductile material under shear dominant loading. *International Journal of Fracture*, 184(1-2):253–266, 2013.

[18] A Ghahremaninezhad and K Ravi-Chandar. Ductile failure behavior of polycrystalline al 6061-t6 under shear dominant loading. *International Journal of Fracture*, 180(1), 2013.

[19] YP Korkolis, S Kyriakides, T Giagmouris, and L-H Lee. Constitutive modeling and rupture predictions of al-6061-t6 tubes under biaxial loading paths. *Journal of Applied Mechanics*, 77(6):064501, 2010.

[20] Akhtar S Khan, Amit Pandey, and Thomas Stoughton. Evolution of subsequent yield surfaces and elastic constants with finite plastic deformation. part iii: Yield surface in tension–tension stress space (al 6061–t 6511 and annealed 1100 al). *International Journal of Plasticity*, 26(10):1432–1441, 2010.

[21] SS Haltom, S Kyriakides, and K Ravi-Chandar. Ductile failure under combined shear and tension. *International Journal of Solids and Structures*, 50(10):1507–1522, 2013.

[22] U Fred Kocks, Carlos Norberto Tomé, and H-R Wenk. *Texture and anisotropy: preferred orientations in polycrystals and their effect on materials properties*. Cambridge university press, 2000.

[23] Viggo Tvergaard and Alan Needleman. Three dimensional microstructural effects on plane strain ductile crack growth. *International journal of solids and structures*, 43(20):6165–6179, 2006.

[24] Matthew Clark, Vernon Yancy, Quentin Sneed, and Shannon Burke. Sources of material failure variability. Technical report, Howared University, 2016.

[25] Hojun Lim, Rémi Dingreville, Lisa A Deibler, Thomas E Buchheit, and Corbett C Battaile. Investigation of grain-scale microstructural variability in tantalum using crystal plasticity-finite element simulations. *Computational Materials Science*, 117:437–444, 2016.

[26] Devin M Pyle, Jing Lu, David J Littlewood, and Antoinette M Maniatty. Effect of 3d grain structure representation in polycrystal simulations. *Computational Mechanics*, 52(1):135–150, 2013.

[27] Joseph E Bishop, John M Emery, Corbett C Battaile, David J Littlewood, and Andrew J Baines. Direct numerical simulations in solid mechanics for quantifying the macroscale effects of microstructure and material model-form error. *Jom*, 68(5):1427–1445, 2016.

[28] Sanjay R Arwade and Mircea Grigoriu. Probabilistic model for polycrystalline microstructures with application to intergranular fracture. *Journal of Engineering mechanics*, 130(9):997–1005, 2004.

[29] Mircea D. Grigoriu. *Stochastic Calculus*. Birkhäuser Basel, 2002.

[30] Richard Zallen. *The Physics of Amorphous Solids*, chapter 2, pages 33–85. Wiley-VCH Verlag GmbH, 2004.

[31] JK Mason and CA Schuh. The generalized mackenzie distribution: Disorientation angle distributions for arbitrary textures. *Acta Materialia*, 57(14):4186–4197, 2009.

[32] M. Grigoriu. Reduced order models for random functions. application to stochastic problems. *Applied Mathematical Modelling*, 33:161–175, 2007.

[33] SIERRA Solid Mechanics Team. Adagio 4.18 User's Guide. Technical Report SAND2010-6313, Sandia National Laboratories, Albuquerque, NM, 2010.

[34] Alejandro Mota, Irina Tezaur, and Coleman Alleman. The schwarz alternating method in solid mechanics. *Computer Methods in Applied Mechanics and Engineering*, 319:19–51, 2017.

[35] WaiChing Sun and Alejandro Mota. A multiscale overlapped coupling formulation for large-deformation strain localization. *Computational Mechanics*, 54(3):803–820, 2014.

[36] A. A. Brown and D. J. Bammann. Validation of a model for static and dynamic recrystallization in metals. *International Journal of Plasticity*, 32–33(0):17 – 35, 2012.

[37] Phillip L Reu. A method for overlapping two dic views by using a two-tone speckle pattern. In *Advancement of Optical Methods in Experimental Mechanics, Volume 3*, pages 119–124. Springer, 2014.

[38] Jay D Carroll, Wael Abuzaid, John Lambros, and Huseyin Sehitoglu. High resolution digital image correlation measurements of strain accumulation in fatigue crack growth. *International Journal of Fatigue*, 57:140–150, 2013.

[39] Adam D Kammers and Samantha Daly. Self-assembled nanoparticle surface patterning for improved digital image correlation in a scanning electron microscope. *Experimental Mechanics*, 53(8):1333–1341, 2013.

[40] J Carroll, W Abuzaid, J Lambros, and H Sehitoglu. An experimental methodology to relate local strain to microstructural texture. *Review of Scientific Instruments*, 81(8):083703, 2010.

[41] J. F. Thomas. Third-order elastic constants of aluminum. *Phys. Rev.*, 175:955–962, Nov 1968.

[42] E.S. Keeping. *Introduction to Statistical Inference.* Dover, 1995.

[43] Joseph E Bishop, John M Emery, Richard V Field, Christopher R Weinberger, and David J Littlewood. Direct numerical simulations in solid mechanics for understanding the macroscale effects of microscale material variability. *Computer Methods in Applied Mechanics and Engineering*, 287:262–289, 2015.

[44] JE Bozek, JD Hochhalter, MG Veilleux, M Liu, G Heber, SD Sintay, AD Rollett, DJ Littlewood, AM Maniatty, H Weiland, et al. A geometric approach to modeling microstructurally small fatigue crack formation: I. probabilistic simulation of constituent particle cracking in aa 7075-t651. *Modelling and Simulation in Materials Science and Engineering*, 16(6):065007, 2008.

[45] Angus J Wilkinson, Graham Meaden, and David J Dingley. High-resolution elastic strain measurement from electron backscatter diffraction patterns: new levels of sensitivity. *Ultramicroscopy*, 106(4):307–313, 2006.

[46] Josh Kacher, Colin Landon, Brent L Adams, and David Fullwood. Bragg's law diffraction simulations for electron backscatter diffraction analysis. *Ultramicroscopy*, 109(9):1148–1156, 2009.

[47] JF Nye. Some geometrical relations in dislocated crystals. *Acta metallurgica*, 1(2):153–162, 1953.

[48] E. Kroner. *Continuum theory of dislocations and self-stresses.* Verlag, 1958.

[49] TJ Ruggles and DT Fullwood. Estimations of bulk geometrically necessary dislocation density using high resolution ebsd. *Ultramicroscopy*, 133:8–15, 2013.

[50] Brent L Adams and Joshua Kacher. Ebsd-based microscopy: Resolution of dislocation density. *Computers, Materials, & Continua*, 14(3):185–196, 2010.

[51] Wolfgang Pantleon. Resolving the geometrically necessary dislocation content by conventional electron backscattering diffraction. *Scripta Materialia*, 58(11):994–997, 2008.

[52] K Tanaka and T Mura. A theory of fatigue crack initiation at inclusions. *Metallurgical Transactions A*, 13(1):117–123, 1982.

Appendix A

Multiscale uncertainty modeling code and Git repository

All of the code developed for this project is stored with the Git version control software. Table A.1

Multiscale UQ Tools	https://code-source.sandia.gov/git/multiscaleUQTools/
srom	stochastic reduced-order models
eulerRF	translation random field model and ROM
make_ustructure	overlay and sculpting code
trv	translation random vectors
utilities	misc.
LDRD project repo	https://gitlab.sandia.gov/62758/multiscale-UP
Computational Science Tools	https://code-source.sandia.gov/git/CompSciTools/
pyTools	various python scripts, including exodus read/write and FEM manipulations

Table A.1: Code and data stored in Git repositories.

Appendix B

Engineering drawings

DESIGN AGENCY PART NUMBER	ISSUE	SHEET ZONE	PREPARED BY	DESCRIPTION	DATE	CHKR	APVD
CARROLL NOTCHED SPECIMEN 6 NOTCH	A	1	B C SALZBRENNER, 01851	NOTCHED TENSILE SPECIMEN 6 NOTCH	03/24/2015	BCS	BCS

6 NOTCH SPECIMEN

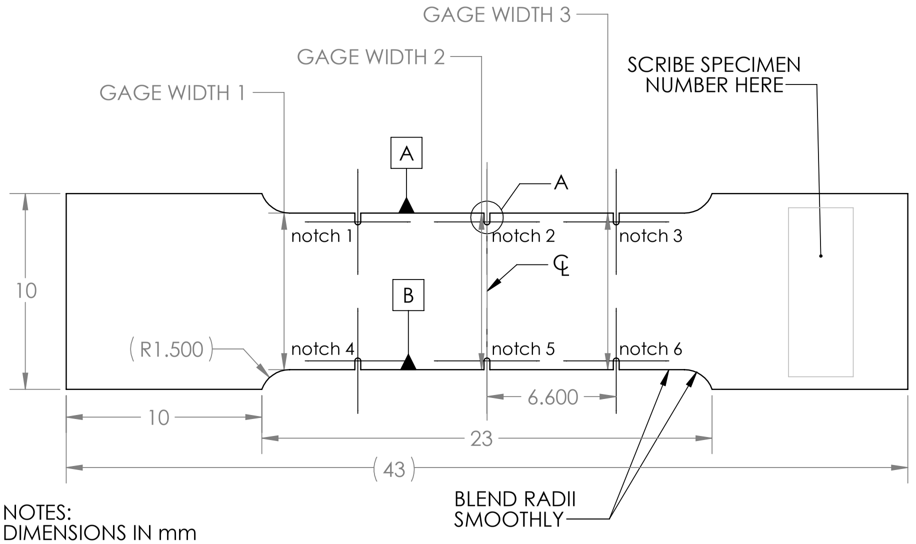

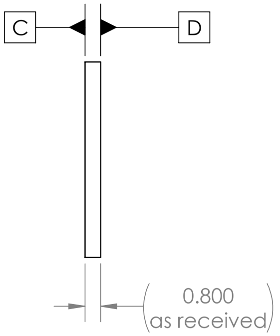

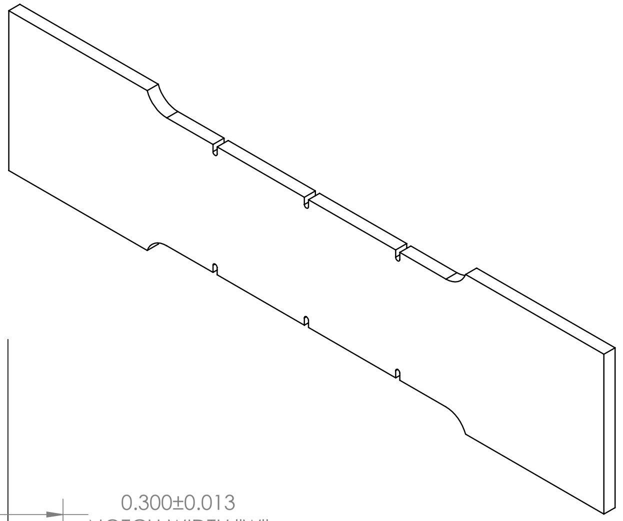

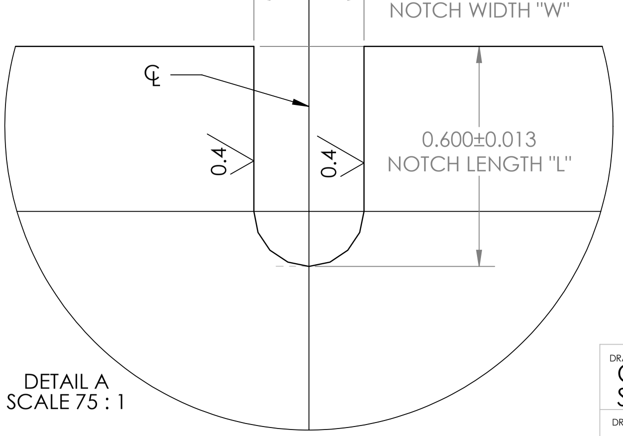

DETAIL A
SCALE 75 : 1

NOTES:
DIMENSIONS IN mm
TOLERANCE ±0.05mm unless otherwise specified
SURFACE FINISH IN um
SURFACE FINISH TO BE INSPECTED AT SANDIA NATIONAL LABS
NOTCH CENTER TO CENTER: 6.6mm
3 NOTCHES ON EACH SIDE
A PARALLEL TO B WITHIN 0.13mm
C PARALLEL TO D WITHIN 0.13mm
BLEND RADII SMOOTHLY
MATERIAL PER CONSULTANT
SCRIBE SPECIMEN NUMBER IN LOCATION INDICATED
NUMBER SPECIMENS FROM 1 TO 60
ADD AN 'R' FOR ROLLING DIRECTION, 'T' FOR TRANSVERSE TO ROLLING DIRECTION
ADD A '-6' FOR 6 NOTCHES SPECIMENS.
EXAMPLE NAME: 8R-6 (8th specimen, cut in rolling direction, 6 notches)
CORRESPONDING SPECIMEN LABELS SHALL BE MARKED ON PLATE WITH A SHARPIE.

MEASURE AND REPORT (TO NEAREST 0.01mm) NOTCH WIDTH, NOTCH LENGTH, AND GAGE WIDTH, PER TABLE BELOW

notch	notch width "W" (mm)	notch length "L" (mm)
1	x.xx	x.xx
2	x.xx	x.xx
3	x.xx	x.xx
4	x.xx	x.xx
5	x.xx	x.xx
6	x.xx	x.xx
GAGE WIDTH 1 (mm)		x.xx
GAGE WIDTH 2 (mm)		x.xx
GAGE WIDTH 3 (mm)		x.xx

DRAWING NUMBER
CARROLL NOTCHED SPECIMEN, 6 NOTCH
DRAWING CLASSIFICATION
UNCLASSIFIED

SIZE B	CAGEC 14213	SCALE 4:1	
	ISSUE A	SHEET 1	OF 5

STATUS SA-CHK-7/28/2000

2 NOTCH SHARP SPECIMEN

DESIGN AGENCY PART NUMBER	ISSUE	SHEET ZONE	PREPARED BY	DESCRIPTION	DATE	CHKR	APVD
CARROLL NOTCHED SPECIMEN, 2 NOTCH SHARP	A	1	B C SALZBRENNER, 01851	NOTCHED TENSILE SPECIMEN 2 NOTCH SHARP	03/24/2015	BCS	BCS

REVISIONS

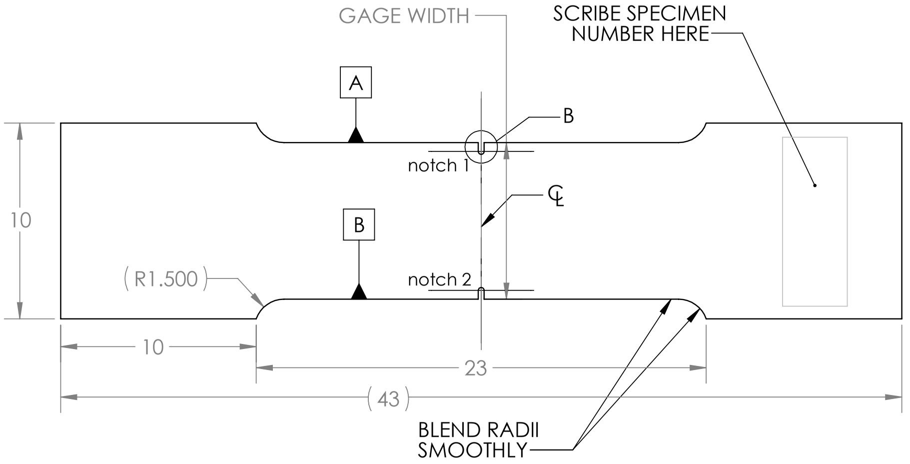

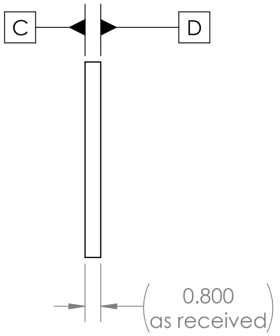

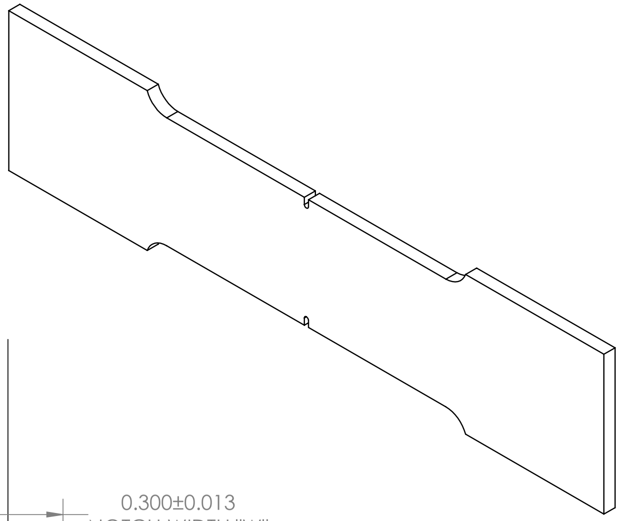

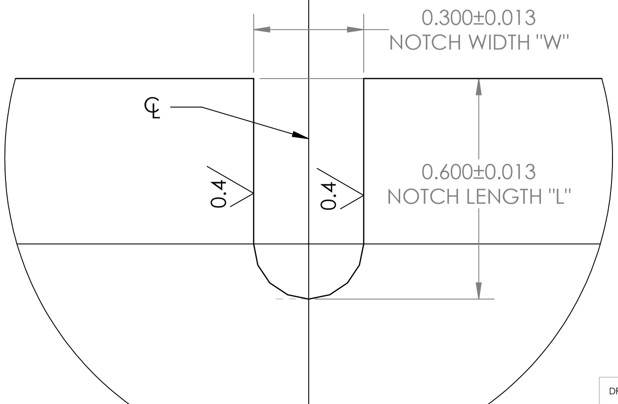

DETAIL B
SCALE 75 : 1

NOTES:
DIMENSIONS IN mm
TOLERANCE ±0.05mm unless otherwise specified
SURFACE FINISH IN um
SURFACE FINISH TO BE INSPECTED AT SANDIA NATIONAL LABS
A PARALLEL TO B WITHIN 0.13mm
C PARALLEL TO D WITHIN 0.13mm
BLEND RADII SMOOTHLY
MATERIAL PER CONSULTANT
SCRIBE SPECIMEN NUMBER IN LOCATION INDICATED
  NUMBER SPECIMENS FROM 1 TO 20
  ADD AN 'R' FOR ROLLING DIRECTION, 'T' FOR TRANSVERSE TO ROLLING DIRECTION
  ADD A '-2S' FOR 2 NOTCH SHARP SPECIMENS.
  EXAMPLE NAME: 5R-2S (5th specimen, cut in rolling direction, 2 notches sharp)
  CORRESPONDING SPECIMEN LABELS SHALL BE MARKED ON PLATE WITH A SHARPIE.

MEASURE AND REPORT (TO NEAREST 0.01mm) NOTCH WIDTH, NOTCH LENGTH, AND GAGE WIDTH, PER TABLE BELOW

notch	notch width "W" (mm)	notch length "L" (mm)
1	x.xx	x.xx
2	x.xx	x.xx
GAGE WIDTH (mm)		x.xx

DRAWING NUMBER
CARROLL NOTCHED
SPECIMEN, 2 NOTCH SHARP
DRAWING CLASSIFICATION
UNCLASSIFIED

SIZE	CAGEC		SCALE	
B	14213		4:1	
	ISSUE A		SHEET 2	OF 5

STATUS SA-CHK-7/28/2000

DESIGN AGENCY	REVISIONS						
PART NUMBER	ISSUE	SHEET ZONE	PREPARED BY	DESCRIPTION	DATE	CHKR	APVD
CARROLL NOTCHED SPECIMEN, 2 NOTCH GRADUAL	A	1	B C SALZBRENNER, 01851	NOTCHED TENSILE SPECIMEN 2 NOTCH GRADUAL	03/24/2015	BCS	BCS

2 NOTCH GRADUAL SPECIMEN

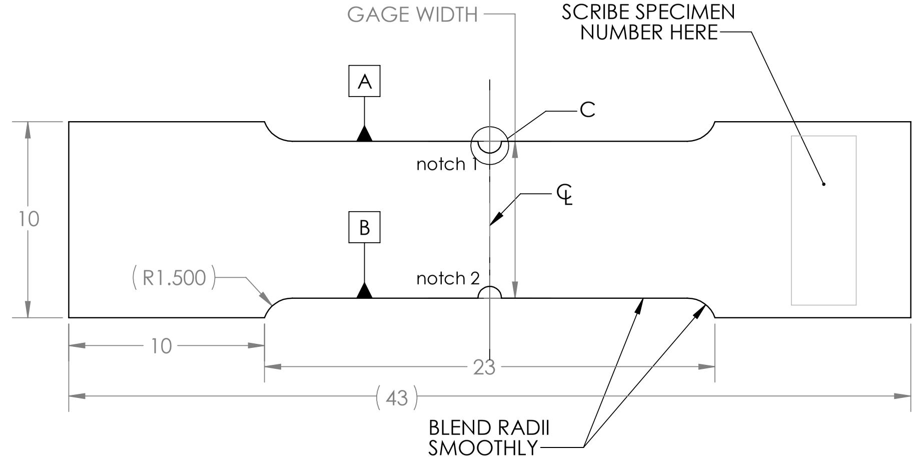

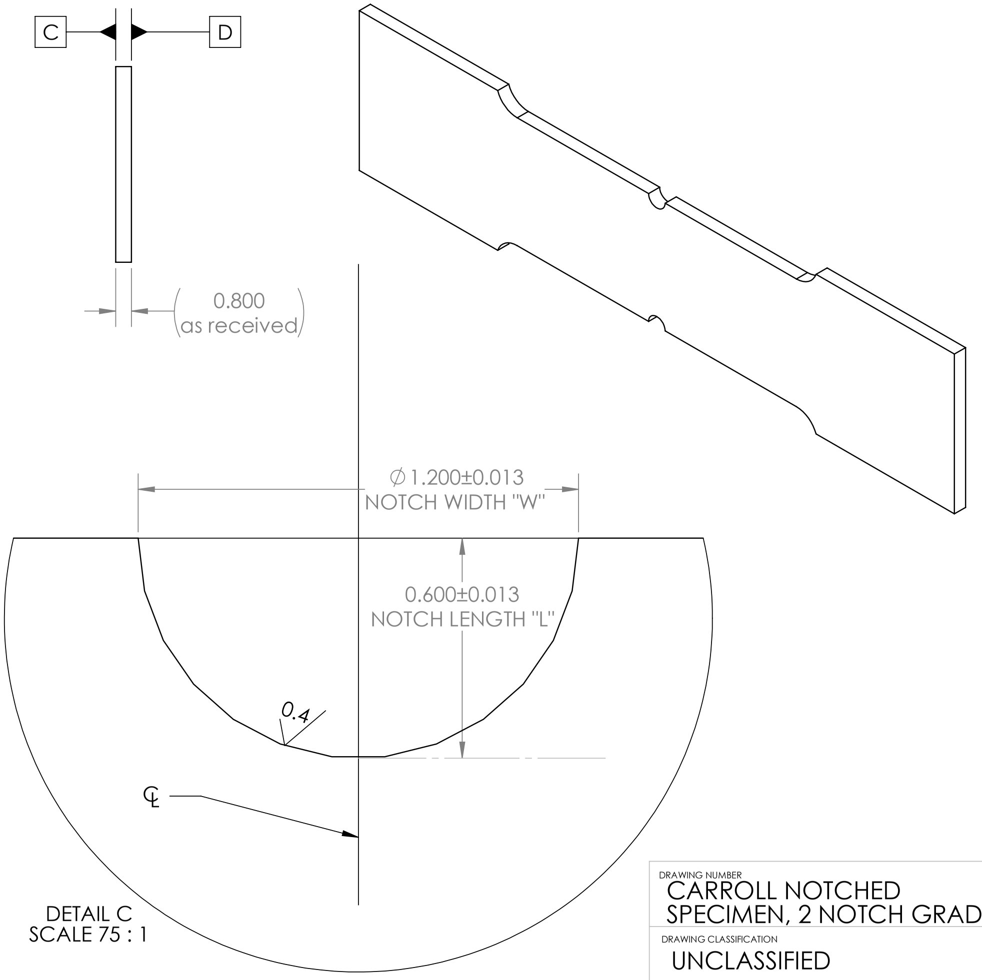

DETAIL C
SCALE 75 : 1

NOTES:
DIMENSIONS IN mm
TOLERANCE ±0.05mm unless otherwise specified
SURFACE FINISH IN um
SURFACE FINISH TO BE INSPECTED AT SANDIA NATIONAL LABS
A PARALLEL TO B WITHIN 0.13mm
C PARALLEL TO D WITHIN 0.13mm
BLEND RADII SMOOTHLY
MATERIAL PER CONSULTANT
SCRIBE SPECIMEN NUMBER IN LOCATION INDICATED
  NUMBER SPECIMENS FROM 1 TO 20
  ADD AN 'R' FOR ROLLING DIRECTION, 'T' FOR TRANSVERSE TO ROLLING DIRECTION
  ADD A '-2G' FOR 2 NOTCH GRADUAL SPECIMENS.
  EXAMPLE NAME: 3T-2G (3rd specimen, cut in transverse direction, 2 notches gradual)
  CORRESPONDING SPECIMEN LABELS SHALL BE MARKED ON PLATE WITH A SHARPIE.

MEASURE AND REPORT (TO NEAREST 0.01mm) NOTCH WIDTH, NOTCH LENGTH, AND GAGE WIDTH, PER TABLE BELOW

notch	notch width "W" (mm)	notch length "L" (mm)
1	x.xx	x.xx
2	x.xx	x.xx
GAGE WIDTH (mm)		x.xx

DRAWING NUMBER
CARROLL NOTCHED SPECIMEN, 2 NOTCH GRADUAL
DRAWING CLASSIFICATION
UNCLASSIFIED

SIZE	CAGEC	14213	SCALE	4:1		
B	ISSUE	A	SHEET	3	OF	5

STATUS SA-CHK-7/28/2000

TENSION SPECIMEN

DESIGN AGENCY PART NUMBER	ISSUE	SHEET ZONE	PREPARED BY	DESCRIPTION	DATE	CHKR	APVD
CARROLL NOTCHED SPECIMEN TENSION	A	1	B C SALZBRENNER, 01851	NOTCHED TENSILE SPECIMEN TENSION	03/24/2015	BCS	BCS

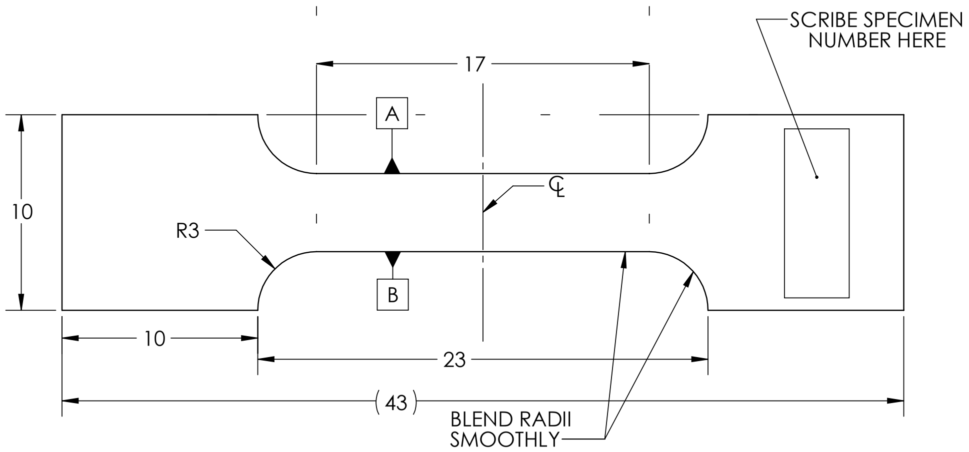

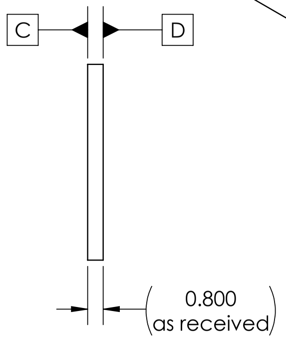

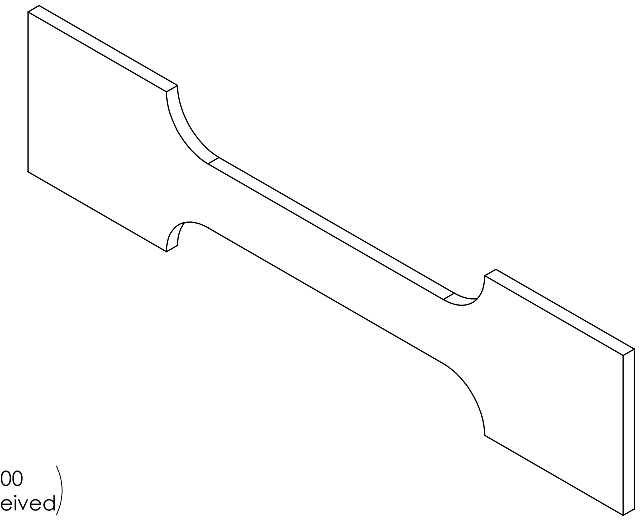

NOTES:
DIMENSIONS IN mm
TOLERANCE ±0.05mm unless otherwise specified
SURFACE FINISH IN um
SURFACE FINISH TO BE INSPECTED AT SANDIA NATIONAL LABS
A PARALLEL TO B WITHIN 0.13mm
C PARALLEL TO D WITHIN 0.13mm
BLEND RADII SMOOTHLY
MATERIAL PER CONSULTANT
SCRIBE SPECIMEN NUMBER IN LOCATION INDICATED
NUMBER SPECIMENS FROM 1 TO 50
ADD AN 'R' FOR ROLLING DIRECTION, 'T' FOR TRANSVERSE TO ROLLING DIRECTION
EXAMPLE NAME: 30R (30th specimen, cut in rolling direction, Tension specimen)

DRAWING NUMBER
CARROLL NOTCHED SPECIMEN, TENSION
DRAWING CLASSIFICATION
UNCLASSIFIED
SIZE B
CAGEC 14213
SCALE 4:1
ISSUE A
SHEET 4 OF 5
STATUS SA-CHK-7/28/2000

DESIGN AGENCY	REVISIONS						
PART NUMBER	ISSUE	SHEET ZONE	PREPARED BY	DESCRIPTION	DATE	CHKR	APVD
CARROLL NOTCHED SPECIMEN, PLATE	A	1	B C SALZBRENNER, 01851	NOTCHED TENSILE SPECIMEN PLATE	03/24/2015	BCS	BCS

PLATE

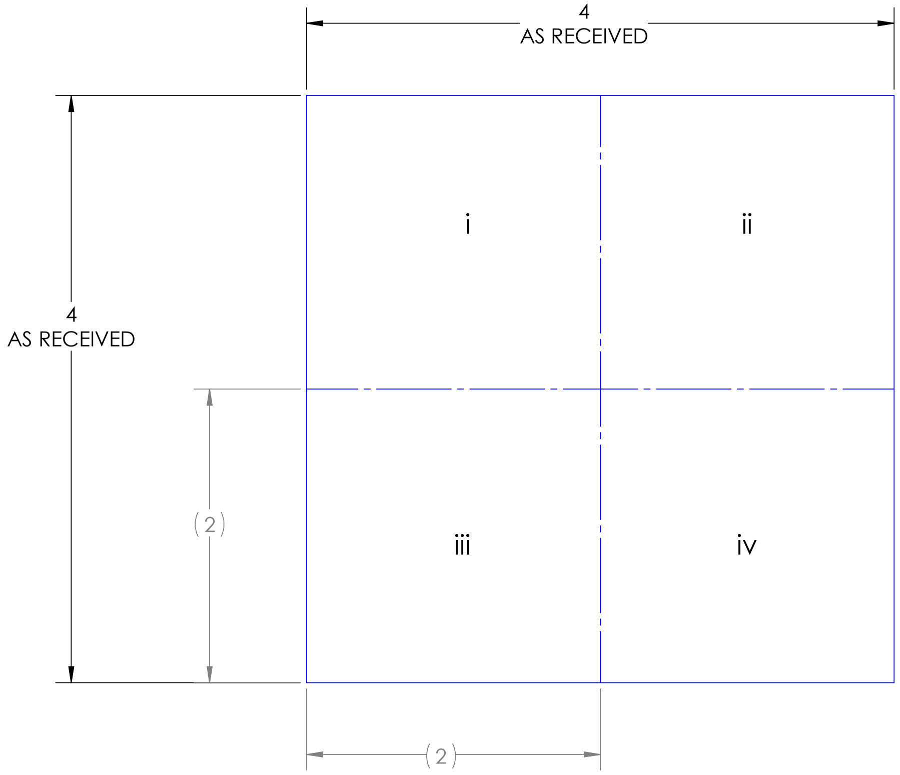

NOTES:
DIMENSIONS IN FEET
MATERIAL PER CONSULTANT
CUT AS RECEIVED PLATE INTO 4 EQUAL QUADRANTS
REMOVE ALL SAMPLES FROM QUADRANT i ONLY
CORRESPONDING SPECIMEN NUMBERS SHALL BE MARKED ON PLATE WITH A SHARPIE.
SEE DRAWING FOR LABELING CONVENTION.

DRAWING NUMBER
CARROLL NOTCHED SPECIMEN, PLATE
DRAWING CLASSIFICATION
UNCLASSIFIED
SIZE B
CAGEC 14213
SCALE 30:1
ISSUE A
SHEET 5 OF 5
STATUS SA-CHK-7/28/2000

DISTRIBUTION:

1	MS 0825	Srinivasan Arunajatesan, 01515
1	MS 0840	Joseph Bishop, 01554
1	MS 0889	Jay Carroll, 01851
1	MS 0359	Donna Chavez, 01171
1	MS 0346	Peter Coffin, 01553
1	MS 0840	Eliot Fang, 01554
1	MS 1027	Richard Field, Jr., 05853
1	MS 0840	Lili Heitman, 01553
1	MS 0840	Jim Redmond, 01550
1	MS 0825	Brian Robbins, 01515
1	MS 0889	Hartono Sumali, 01851
1	MS 0899	Technical Library, 9536 (electronic copy)

Sandia National Laboratories